UNIVERSITÀ DEGLI STUDI DI NAPOLI FEDERICO II

International PhD program on:
Novel Technologies for Materials, Sensors and Imaging

Organic LEDs: from limits analysis to device performances improvement

Giuseppe Nenna

Chairman: Prof. Antonello Andreone

Tutors: Prof. Antonio Cassinese
                Eng. Carla Minarini

November 2009

Gracias a la vida, que me ha dado tanto
Me ha dado la risa y me ha dado el llanto
Así yo distingo dicha de quebranto
Los dos materiales que forman mi canto
Y el canto de ustedes, que es el mismo canto
Y el canto de todos, que es mi propio canto
Y el canto de ustedes, que es mi propio canto

Violeta Parra

Table of Contents

CHAPTER III

CHAPTER IV

CHAPTER V

Acknowledgements

The world of semiconductor technology is continuously dazed by the surprising results achieved in the field of organic semiconductor. In particular, the display technology and solid state light sources developed a complete new class of devices as the OTFT (Organic Thin Film Transistor) and the OLED (Organic Light Emitting Diodes). In particular, the OLED are a new class of light sources can be used to obtain completely new solutions, not achievable with the traditional light sources that are currently on the market. They can cover a large range of colours and can be used in many applications, on rigid and flexible substrates.

To make suitable the OLED for the light sources market the study of the operation principles of organic LED is essential to determine all the mechanisms that affect the efficiency and life-time expectancy. The latter point can be improved thanks to a favourable change in work-point so reducing the electrical stress, thereby making the device more attractive

Despite considerable improvement in device properties, a better understanding of the nature of charge transport in these devices and the physics of organic/inorganic and organic/organic interfaces are crucial for further developments of optoelectronic organic devices. Besides quantitative correlations between the glass transition occurrence and the device operating limits are to deeply investigate the mechanisms that lead to device failures.

Moreover, brightness and efficiency are extremely important factors for the employment of organic light emitting diodes (OLEDs) in lighting and displays application in the competition against more standard technologies. It is also to take into account the possibility to enhance the efficiency through an improvement in the optical out-coupling in the photons path through the entire device and the substrate.

Extracting the wave-guided light within OLED and more in general within electroluminescent flat multilayer device structure will be one of the main driving forces to improve the device lifetime.

The experimental work described in this thesis was conducted to analyze different

approach about the OLED optimization and to investigate different solutions, trying to identify the best strategies to use for our purposes.

The **first Chapter** will analyze the results obtained on small area devices with attention on the different performances that were obtained, varying the nature of the contacts and of the organic layers and charging the charge balance approach. The dependence of device performance, and particularly of device efficiency, is discussed in the framework of the carrier recombination by means charge transfer mechanisms. The device limits remarking the aging phenomena and introducing the glass transition issues will be studied.

The **second Chapter** will show the characteristics of opto-electronic devices to give a right understanding on the injection and transport mechanisms of charge carriers. Temperature dependence and high field limits will be analyzed to better deduce the experimental data coming from the next chapter. Furthermore, some simple studies on thermal degradation of Organic LEDs using InfraRed imaging will be shown

The **third Chapter** will be focus on the investigation of the optical and electrical failure mechanisms during the glass transition phenomena in the archetypal OLED structure by using variable temperature AC impedance measurements. The related experimental data are discussed in the framework of the Universal Dielectric Response (UDR) model. The relation between the temperature kinetics towards the glass transition of organic layers frequency response and of the OLED electro-optical response is discussed.

The **fourth Chapter** will analyze the different possible approaches in the improvement of the photons extraction. A modelling of the output coupling and some methods to increase the external efficiency are discussed by means several ray-tracing simulations. In particular, the coupling efficiency enhancement in using microlens array and substrate texture is shown trough experimental results.

The **fifth Chapter** will present the experimental measurements on nanocomposite volumetric scattering films and on organic light emitting device (OLED) with and without the scattering layers. The data analysis are compared with Henyey-Greenstein

radiative-transfer model to narrow down the parameters that can be important in the identification of more suitable scattering layers to increase the external efficiency in terms of out-coupled light respect to the total generated amount.

Finally the **Conclusions** will be exhibited showing the results and the comments related to the reported data, paying attention to the limits of the devices and their quantum efficiency that are dependent on a number of different factors that have been widely discussed in this thesis.

CHAPTER I
"Organic LED"

In this chapter it will be shown how semiconducting organic materials have found an important application in organic light emitting devices (OLEDs). We will discuss in details the main factors that need to be addressed in order to optimise the overall device performance. In this chapter, we will examine the fundamental limits to the performance of OLEDs, and concentrate on methods to improve their efficiencies. We will first explain the various factors that comprise the power efficiency of an OLED. The charge transfer, a mechanism for significantly improving the efficiency of organic devices, will be described and characterized. Then, the device limits, remarking the aging phenomena and introducing the glass transition issues, will be studied.

1.1 Organic LED and radiative efficiency

The OLED can play a key role in the new frontier of lighting that lead to appear obsolete the Edison's invention that just over a century ago had changed the life of mankind.
Indeed, one of the important positive notes about the OLED technology is the energy savings that may result with their employment.
Recent projections show how the performances of OLED devices are beginning to be very close to those of inorganic LED and many important companies start to contemplate a massive OLED production for lighting application [1].
It is not widely known that lighting is one of the biggest causes of greenhouse gas emissions. The energy consumed to supply lighting the world requires greenhouse gas emissions of 1900 Megatonnes (Mt) of CO_2 per year This is equivalent to 70% of the emissions from the world's cars and over three times the emissions from aircraft [2].
This kind of problem is evident observing the pictures of the earth taken by satellite where is possible to notice the large amount of energy used for lighting, especially in areas of the planet most economically developed [3].

As already stated OLEDs developments can be a useful solution for the wasted energy because of the realized laboratory prototypes that demonstrated a wide range of efficiency improvements.

In particular, the process of light emission in OLEDs is based on the injection of positive and negative carriers from electrodes into an organic layer. These recombine forming excitons that can radiatively decay to produce electroluminescence from the active organic semiconductor (OS) layer itself. The emission color can be tuned over a wide range by appropriate choice of polymer and/or small molecule based on organic materials. The basic architecture for an organic semiconductor device is shown in figure 1.1.
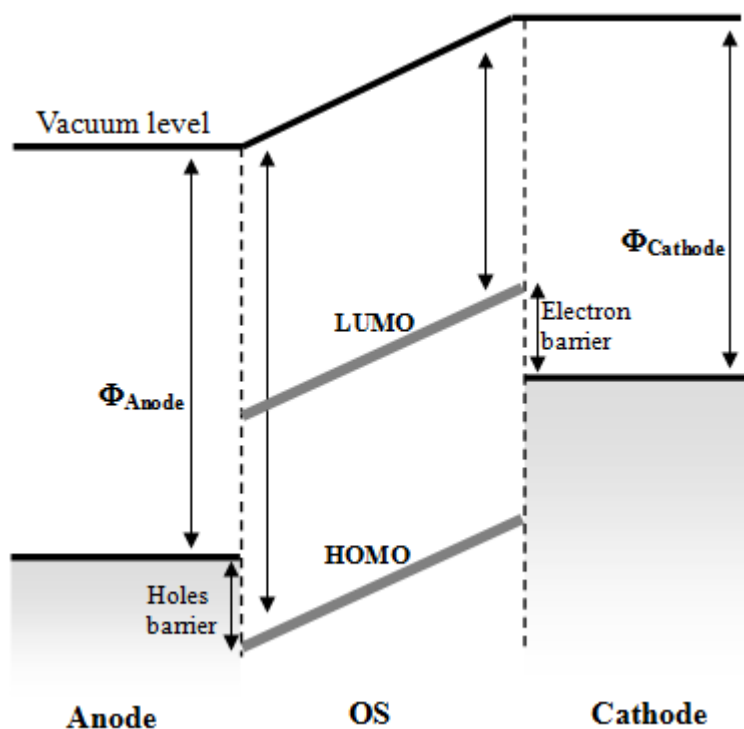
Fig. 1.1: Band diagram for a single layer Organic Semiconductor device.

Electron injection from the cathode is generally facilitated by a low work function material to reduce the electron barrier between the cathode Fermi level and the organic semiconductor LUMO level. From the other hand the hole injection is facilitated by the poly-ethylenedioxythiophene:poly-styrene sulphonic acid (PEDOT:PSS) layer, while the effective anode contact is provided by a transparent ITO coating.

In order to understand, and therefore to maximize the efficiency of an OLED, it is

necessary to consider the various loss mechanisms in this device configuration, which are the subject of this section. Thus, the charge carriers recombine in the organic layer to produce excitons and consequently photons, but it is not as simple as it appears.

The first loss process occurs due to carriers that do not combine, the probability of that is strictly related also to the balance between the number of positive and negative charges injected into the organic layer under investigation. This factor is commonly referred as the charge balance, which is defined as η_r is discussed in detail in this section of the thesis.

The excitons that are formed can be of two types, singlets that have a radiative decay and triplets that decay through nonradiative processes and thus lead to a loss of efficiency. The ratio of singlets to triplets (χ_s) is another important issue and will be reviewed in the second part of this section.

The singlet excitons do not all radiatively decay, due to the presence of non-radiative pathways for the excitonic states to fundamental relaxed states. The loss in efficiency, in this case, is related to the intrinsic photoluminescence efficiency of the organic material, as well as additional losses due to exciton quenching mechanism. These factors are collected together to define a quantity (Φ_{fl}) that is discussed in the last part of this chapter.

Finally, a large portion of the light generated in the device is unable to escape, thereby introducing a loss that is referred to as the output coupling (η_e), which will be discussed extensively in the Chapter IV.

These four major losses described above can be combined and summarized to determine the external quantum efficiency of OLED device (eq. 1.1)

$$\Phi_{el} = \chi_s \Phi_{fl} \eta_r \eta_e \tag{1.1}$$

This chapter will conclude by stating the current efficiencies that have been realized in devices and the potential for further improvements by minimizing the losses analyzed in (eq. 1.1).

1.2 Charge injection in organic films

The interface between the organic semiconductor and the contacting electrode plays an important role in the overall operation of the organic electronic devices. Indeed in order to maximize the quantum external efficiency it is necessary that the electrodes supply enough amount of carriers to the charge recombination and to the consequently exciton formation.

If the charge transport is restricted in the injection at the contacts, a device is said to be injection limited. In this case, the metal/organic interface may show non-Ohmic and consequential nonlinear I−V characteristics. For this reason, the band offset between the metal work function and the HOMO or LUMO level in the organic semiconductor (depending on whether the transport is p- or n-type) is a fundamental factor in determining the type of contact at the interface [4-7].

As reported in table 1, in nature there are several types of metals with big differences in their work function that can be selected depending on the test under examination.

Table 1. Work functions for various metals, according to [6] and [8]

Element	Work function (eV)
Yb	2.63
Sm	2.73
Li	2.95
Ca	3.00
Mg	3.70
Al	4.30
Ag	4.32
Zn	4.47
Cu	4.70
Au	5.10

Following this, we give an account about the performances of OLED devices with structure, ITO/TPD/Alq3/cathode made on a rigid glass substrate, using different types of cathodes, as shown in figure 1.2.

This analysis is reported to assess the change in the efficiency of opto-electronic devices changing the used cathode [4-7].
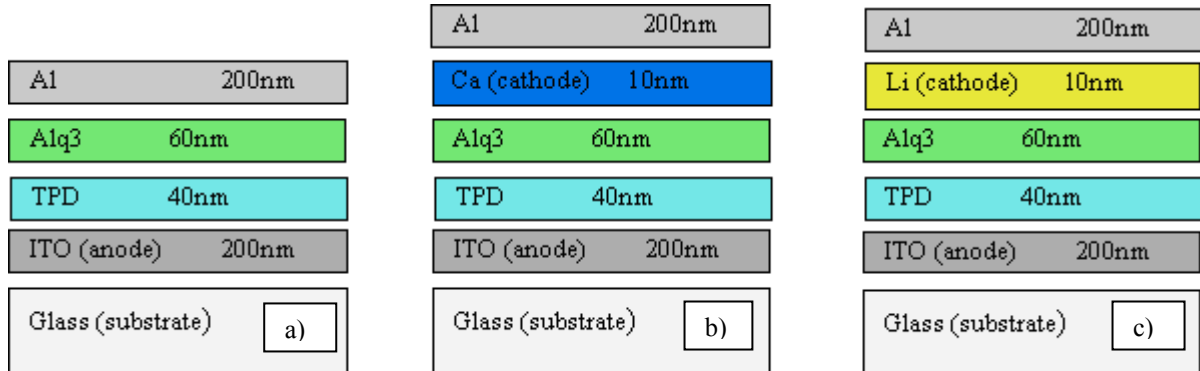
Fig. 1.2: The devices considered in this test: a): ITO/TPD/Alq$_3$/Al;
b): ITO/TPD/Alq$_3$/Ca/Al; c): ITO/TPD/Alq$_3$/Li/Al device.

To give a better understanding in the facilitated electron injection from a low work function cathode material (in this case Li and Ca) reducing the electron barrier between the cathode Fermi level and the organic semiconductor LUMO level as shown in figure 1.3.
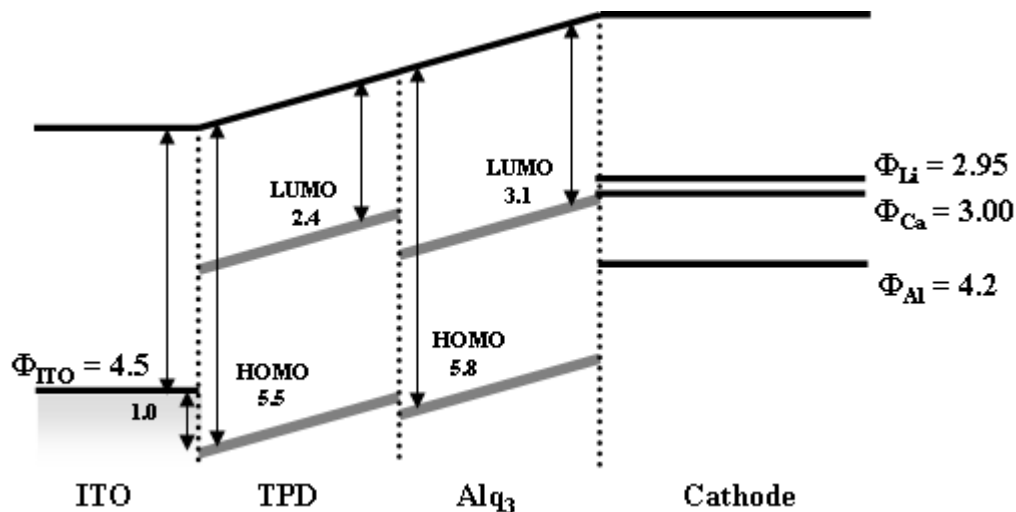
Fig. 1.3: Band diagram for the devices under test as described in detail in the previous figure

The performances of the devices have been quantified by evaluating at the same time, the dependence on the applied voltage, the electroluminescent and the current characteristics.

In particular, the efficiency of the devices was rated in terms of light intensity and current of the device (Cd/A), varying the applied voltage as reported for illustration purpose in figure 1.4.
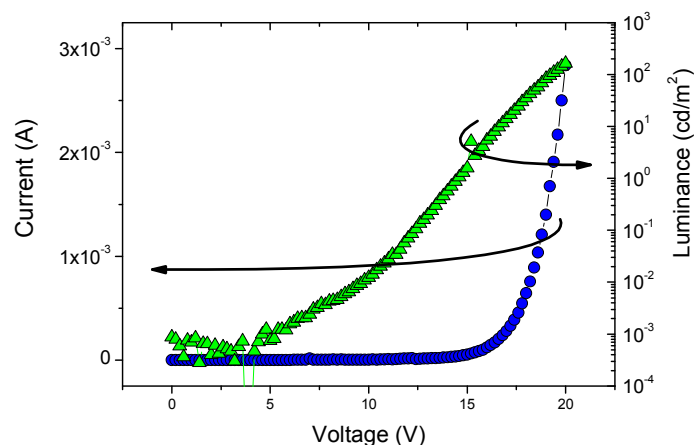
Fig. 1.4: The current device and the relative electroluminescence versus voltage for a ITO/TPD/Alq3/Al device.

In figure 1.5 we demonstrate the impact of the cathode metal work function on the device performance of organic electroluminescent devices. Our measurements clearly show that low-workfunction cathode metals can improve device performance and may optimize the efficiency.
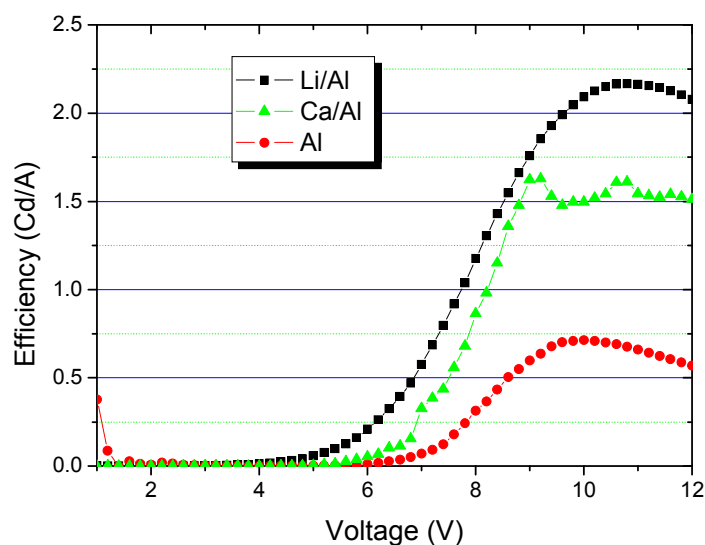
Fig. 1.5: The impact of the cathode metal work function on the device efficiency of

organic electroluminescent devices.

It is widely accepted that, basically, the LUMO of an organic solid corresponds to the semiconductor conduction band with respect to charge carrier injection [9–11, 14]. Nevertheless, on a microscopic scale, conduction mechanisms in "classic" inorganic semiconductors are distinct from charge transport in molecular solids, and low work function cathode metals do not automatically improve device performance.

The use of metal alloys [6,9] or additional thin insulating layers between cathode and electron transport layer as already demonstrated [10] are promising approaches. The latter can be well described by hopping in a particular density of states [11].

1.2.1 Thermionic emission and Tunnelling from contacts

One possible mechanism for current conduction in OLEDs is by thermionic emission of charge over an energy barrier at the organic heterojunction or a Schottky barrier at the organic–electrode interface. Assuming that the OLED behaves as a forward-biased diode with series resistance Rs we apply the diode equation (eq. 1.2) [8]

$$I = I_0 \left[\exp\left(\frac{q(V - IR_s)}{nKT} \right) - 1 \right]$$

(1.2)

where n is the ideality factor which may be temperature dependent and I_0 is the saturation current (figure 1.6).

Such large series resistances, coupled with the anomalously large n values suggest that the current is not controlled by thermionic emission over an energy barrier at the organic hetero-junction or at the contacts. Even with this extreme choice of parameters, theory and data differ significantly [12].
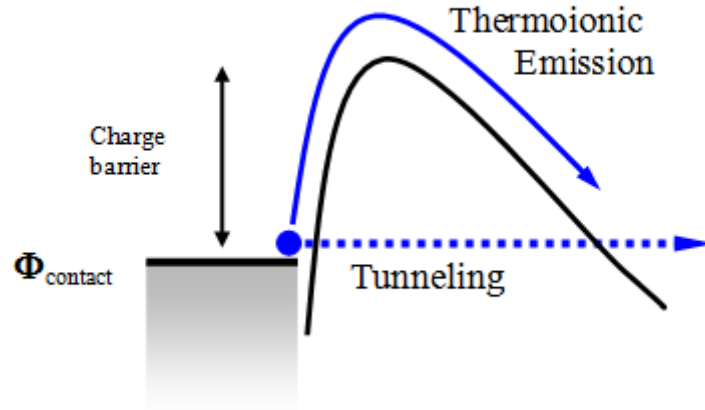
Fig. 1.6: Schematic representation of two possible mechanisms for charge injection in organic semiconductors: tunnelling through the barrier and thermionic emission over the barrier.

More recent work on the I–V and EL characteristics of single-layer polymer-based OLEDs has suggested that tunnelling from contacts into the conduction and valence bands of the organic layer limits current flow [12-15].

Nevertheless, to fit the data from molecular OLEDs to a tunneling model, we assume a triangular barrier at the electrode–organic interface, so that the current follows the Fowler–Nordheim equations (eq. 1.3) and (eq. 1.4) [12-15]:

$$J \propto F^2 \exp\left(-\frac{B}{F}\right)$$

(1.3)

$$B = \frac{8\pi\sqrt{2m^*}\,\varphi^{3/2}}{3qh}$$

(1.4)

where F is the applied field, B is the barrier height, and h is Planck's constant.

But also in this case the experimental data show significant difference from the expected theoretical curves, and only at the highest applied fields there is a good approximation, where tunnelling is expected to dominate [12] [13].

Given the poor fit to the data, and inappropriate temperature dependences of both the tunnelling and thermionic emission models generally are taken into account in cooperation the mentioned mechanisms to explain the observed data.

If a metal-semiconductor contact has a negligible junction resistance relative to the total resistance of the semiconductor device it can result an ohmic contact. A satisfactory ohmic contact should not significantly perturb the device performance and can supply the required current with a voltage drop that is sufficiently small compared with the drop across the active region of the device [8].

1.3 Charge balance

Here we analyze the problem of recombination charges in organic materials and the correlated loss trouble in balanced and unbalanced devices.

The charges recombination and the consequent device efficiency require a model that includes charge injection, transport and recombination (exciton formation) as well as all the space charge effects in the organic layer.

In many papers and the related experiments, electron-hole recombination in organic materials is thought to follow the Langevin bimolecular recombination model. This model is valid if the average mean free path of the carriers is much less than the radius of capture of one carrier by the other [16].

Moreover, it is found that the bimolecular recombination is thermally activated with identical activation energy as measured for the charge carrier mobility. This demonstrates that the recombination process is of the Langevin type, and explains why the conversion efficiency (photon/carrier) of a polymer light-emitting diode is temperature independent, in contrast to conventional inorganic LEDs.

This condition is generally true in low mobility materials such as conjugated polymers and small molecules where the mean free path, or hopping distance (of order 1 nm), is much less than the Coulomb Capture radius (of order 14 nm at room temperature).

In the Langevin model, the recombination current from bipolar equilibrium carrier densities nc and pc with mobilities µn and µp is given by (eq. 1.5):

$$\eta_r = \gamma n_c p_c = q \frac{(\mu_n + \mu_p)}{\varepsilon n_c p_c}$$

(1.5)

where γ is called the Langevin recombination coefficient.

The dependence of device performance, and particularly the device efficiency, on carrier injection, transport and recombination has been the subject of many studies, both in polymers and small molecules [17-20] and there is a wide consensus that the optimized device should have ohmic injection, so the barriers for injection of each carrier should be minimized, and we will concentrate more on the effect of mobility and recombination rate on the device efficiency.

The perfect balancing and the correlated optimum in the efficiency requires that the

numbers of hole and electron should be identical, i.e., that the two carriers should have the same mobility. In this ideal condition, the recombination profile, the current density, the luminance, and the efficiency are determined by the recombination rate [17][19].

In the true world, where the mobility of the two carriers is different, the recombination takes place closer to the electrode injecting the carrier with the lowest mobility where there is more probability in loss process.

For this reason, it will be very important the study about the mobility charges in polymer or small molecules to have a prediction about the probability in the recombination charge and the effective device efficiency [19][20].

In particular, when the two mobilities are very different, the current is controlled by the carrier with the highest mobility, while the recombination and efficiency are controlled by the carrier with the lowest mobility.

In these circumstances multilayer structures have to be used in order to improve charge balance and to optimize the device efficiency, figure 1.7.
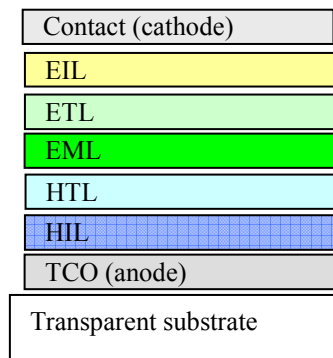
Fig. 1.7: A general OLED multilayer structure where are introduced: the electron injection layer (EIL), the electron transport layer (ETL), the emitter layer (EML), the hole transport layer (HTL), the hole injection layer (HIL) and a transparent conductive oxide (TCO).

Furthermore, also non-ohmic contact and charge blocking layer can be used, to match artificially the mobilities with the injection rates that could result essential to optimize the device efficiency.

1.4 Excited Electronic States in Organic Semiconductors

The emission process of OLEDs, as already mentioned, involves the recombination of electrons and holes, which form one of two types of excitated states; singlets and triplets. An important distinction of these two states is that the singlets can relax radiatively, whereas for the triplet states this process is forbidden, and therefore, relaxation occurs via nonradiative processes. Simple spin statistics suggest that the ratio of singlets to triplets is 1:3, although studies have shown that this is not applicable in polymeric materials.

This ratio of singlets to triplets, referred to as χ_s is, thus, a fundamental factor in determining the ultimate limit of OLED efficiency.

In this section, a brief description is provided on the formation of singlets and triplets followed by a discussion of the ratio for different materials. The final section will focus on the use of electro phosphorescent materials, which can enable triplet emission to be achieved.

The competition between radiative and nonradiative decay processes is of fundamental importance in OLEDs, since they determine the efficiency of emissive material that is directly related to the device efficiency. As well, the photoluminescent quantum efficiency (Φ_{fl}) is a measure of this ratio, which can vary significantly for different materials. In addition to this intrinsic photoluminescent efficiency of the emissive material, there are a number of additional factors that lead to further reduction in the luminescent efficiency, as the presence of impurities diffusing from the electrodes into the organic layer, or the activation of bleaching occurrence and the interaction between the excitons and the metal electrodes causing quenching phenomena.

1.4.1 Fundamental principles of energy and charge transfer

The triplet states in OLED devices are nonradiative because of the selection rules: this relaxation process would require one of the spin states to flip spin to avoid conflicting with the Pauli Exclusion Principle. Decay process involving triplets, thus have significantly longer time scales for radiative relaxation, and therefore, decay occurs predominantly via nonradiative processes.

Spin-flip processes can occur through interactions with impurities or defects and this

leads to phosphorescent emission and is several orders of magnitude smaller in magnitude in comparison to the fluorescence of the singlet states.

Many papers dealing on small molecules [21-23] and polymers, using different combinations of guest-host materials, demonstrated that phosphorescent signal can be enhanced by incorporating heavy mass element organo–metallic phosphors in the form of guest dopants to enhancing the spin-orbit couplings and causing a situation in which the selection rules are less rigid.

Thus the spin-orbit coupling enhancing the spin-flip process needed for radiative decay of the triplet state.

In figure 1.8 there is a simple schematic representation about the triplet dynamics in a guest-host sistem the rates of forward and back transfer, k_F and k_B, respectively, are determined by the free energy change (ΔG) and the molecular overlap; also significant are the rates of decay from the guest and host triplet states, labeled k_G and k_H, respectively.
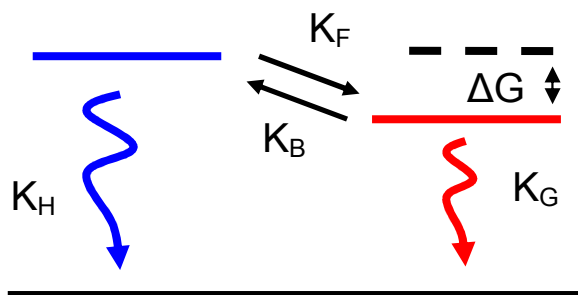
Fig. 1.8: Triplet dynamics in a guest-host system: Adapted from References [22].

As already stated, the emission processes from triplet's states are very difficult. In addition we know that if the excited state is formed from the combination of two uncorrelated electrons, then in a completely random formation process the relative degeneracy of the singlet and triplet states result in a way that the fraction of singlet excitons is $\chi_s = 0.25$. For this reason many companies and research institutes have tried in the last decades to enhance the OLED efficiency also improving the possibility to have a radiative decay also from the triplet state.

The triplet energy difference ΔG, for example, can be estimated by measuring the relaxed triplet state energies of both the donor and acceptor molecules from the highest-energy transition observed in their phosphorescent spectra, taken at low temperature to minimize

non-radiative transitions.

Triplet energy transfer is a hopping process commonly known as Dexter transfer and follows (eq. 1.6):

$$^3D*+{}^1A \rightarrow {}^1D+{}^3A* \tag{1.6}$$

where D is the donor and A, the acceptor. The superscript numbers 3 and 1 represente triplet and singlet states, respectively, and the asterisk signifies an excited state. Singlet energy transfer follows (eq. 1.7):

$$^1D*+{}^1A \rightarrow {}^1D+{}^1A* \tag{1.7}$$

Host singlet states may transfer to guest singlet states by means of Dexter transfer, except when guest-host singlet spectral overlap is strong, in which case long-range dipole-dipole or Förster energy transfer predominates [23,24]. The triplet state of the donor may also Förster transfer to the singlet state of the acceptor, following (eq. 1.8):

$$^3D*+{}^1A \rightarrow {}^1D+{}^1A* \tag{1.8}$$

This process is known as sensitized fluorescence when it results in the transfer of triplet excitons to the singlet state of a fluorescent dye. It may be very efficient if the donor is phosphorescent [23-25].

In this scenario, it is effortless to recognize that the efficiency formula (eq. 1.1) take into account too less physical phenomena and has to be drastically changed into (eq.1.9)

$$\Phi_{el} = [\chi_s\Phi_{fl}\eta_s + \chi_t\Phi_{ph}\eta_t]\eta_r\eta_e \tag{1.9}$$

where:

Φ_{ph} = phosphorescence efficiency

$\chi_t = (1- \chi_s)$ fraction of excitons in triplet states

η_s = transfers efficiency of singlet states from a material D (donor) to a material A (acceptor).

η_t = transfers efficiency of triplet states from a material D (donor) to a material A (acceptor).

In figure 1.9 are summarized all the possible energy transfer in the presence of a phosphorescent and a fluorescent guests. From theory, in principle, all excitons are transferred to the singlet state of the fluorescent dye, as triplets in the dye non-radiatively recombine. Electron–hole recombination creates singlet (S) and triplet (T) excitons in the host material. There is a probability of direct transfer into the singlet state of the fluorescent dye by a Förster process, or Dexter transfer into the triplet state that could be a source of loss. Singlet excitons in the phosphor are subject to intersystem crossing and transfer to the triplet state. From this state, the triplets may either dipole–dipole couple with the singlet state of the fluorescent dye or they may Dexter transfer to the triplet state, accomplish to an another loss mechanism.
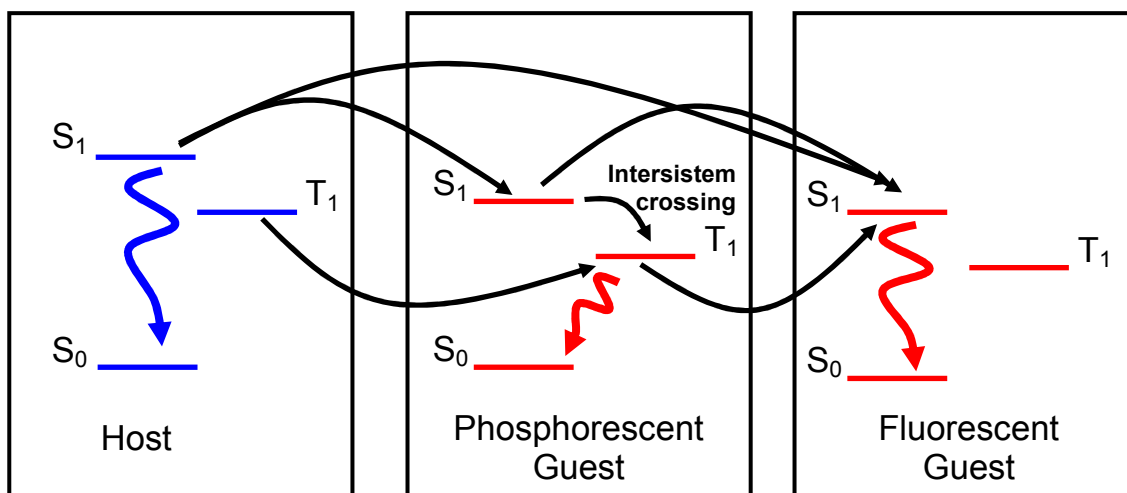
Fig. 1.9: A representation of the relevant processes that occur in the presence of phosphorescent and fluorescent guest materials Adapted from References [23].

To present a simple example of an OLED based on an energy transfer mechanism, and in particular based on a FRET (Forster Energy Transfer) mechanism, we realized a uncomplicated device in which the host polymer material was the PF6 (Polyfluorene) and the fluorescent dye was the DCM (4-dicyanomethylene-6-(ρ-dimethylaminostyryl)-2-methyl-4H-pyran).

As expected, in this case there was a spectral red-shift in presence of the DCM dye (see figure 1.10) that gives us a visible justification to the processes previously explained.
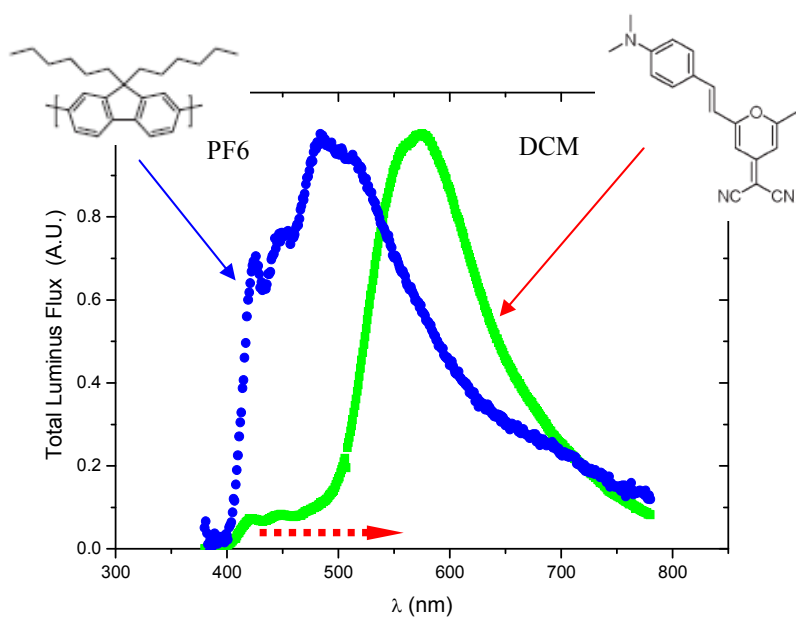
Fig. 1.10: OLED spectra in presence of DCM molecules dopants in polyfluorene polymer matrix. In inset is possible to observe a schematic representation of the molecules under investigation.

1.5 The organic/organic heterojunction

Multilayer structures efficiently confine charge carriers and the relative excitons, but another essential property is that neighbouring molecules, at the interface, have different chemical composition and the device characteristics could be largely affected by the chemical and physical interaction at organic/organic interfaces.

A possible interaction observed at organic/organic interfaces is the formation of a charge-transfer excited-state complex known as an exciplex rather than bulk excitons only. Figure 1.11 shows the energy levels that can interact in favour of the exciplex formation and brings evidence in the nature of exciplex itself.
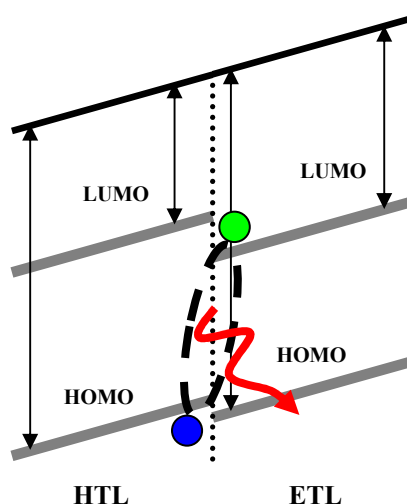
Fig. 1.11: Band diagram and the corresponding electronic energy representation of an excited bimolecular state extended between a molecule of the hole-transporting layer and a molecule of the electron-transporting layer.

The exciplex can be considered as an excited bimolecular state and this kind of quasi-particles can only appear at interfaces between different materials [26, 27].

The exciplex formation generally leads to the manifestation of some loss mechanism in electroluminescence efficiency and a consequent long wavelength emission. Since the emission wavelength of the exciplexes depends on the ionization potential of the electron donor molecules and the electron affinity of the electron acceptor molecules, a remarkable change in emission colour can be observed in a strong electron donor-acceptor combination. In addition, very delicate exciplex formations can occur between

two molecules having similar energy levels and these formations can lead to a modification in the electroluminescence characteristics.

The exciplexes create between two different molecules in which one of them is in an excited state and the other is in a ground state. In the OLEDs consisting of an emitting layer, a hole transport layer, and an electron transport layer, there is a high possibility that exciplex formation occurs at the ETL/EML or HTL/EML interfaces and so there are wide range of possible intra-molecules excited states that can give rise to a change in the emitted spectra.

For this reason there are a lot of papers dealing with the study and the application of exciplex formation to the tuning of emission colours and white emitting OLEDs for lighting purpose [28, 29].

Consequently, fine-tuning of energy levels between neighbouring layers can be a critical point to maximize electroluminescence efficiency and to modify the emission spectra depending to the situation.

1.6 OLED device limits

1.6.1 Aging process in OLED device

As is well known in the literature, the aging of the OLED devices is largely due to the interaction of environmental agents (oxygen, moisture) with organic materials [30]. However, devices manufactured in conditions completely inert and subsequently encapsulated, have a lifetime limited by intrinsic causes under electrical operation [31]. These kinds of considerations give as enough elements to simply understand that a critical point could be also the operation working-point of our devices. In detail, from figure 1.12 we can see that the slope (B) of electroluminescence versus time will be modified changing the current, and thus the lifetime will be reduced increasing the forced current. Moreover, it is possible to see also a change in the applied voltage as already reported in literature [32].
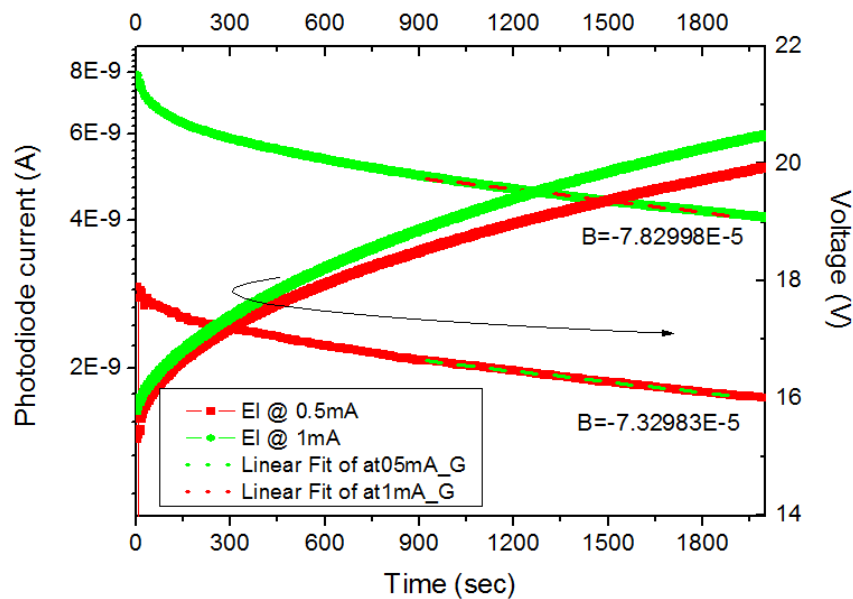
Fig. 1.12: Electroluminescence versus time for an applied current of 0.5 mA (red curve) and for 1 mA (green curve). Moreover, it is reported the change of applied voltage during the measure.

Several studies conducted in recent years on different OLED structure, have highlighted how, from the phenomenological point of view, the degradation of this class of devices is

always accompanied from formation and evolution of progressive space-free electroluminescence zones, those zones are called "dark spots" (figure 1.13).
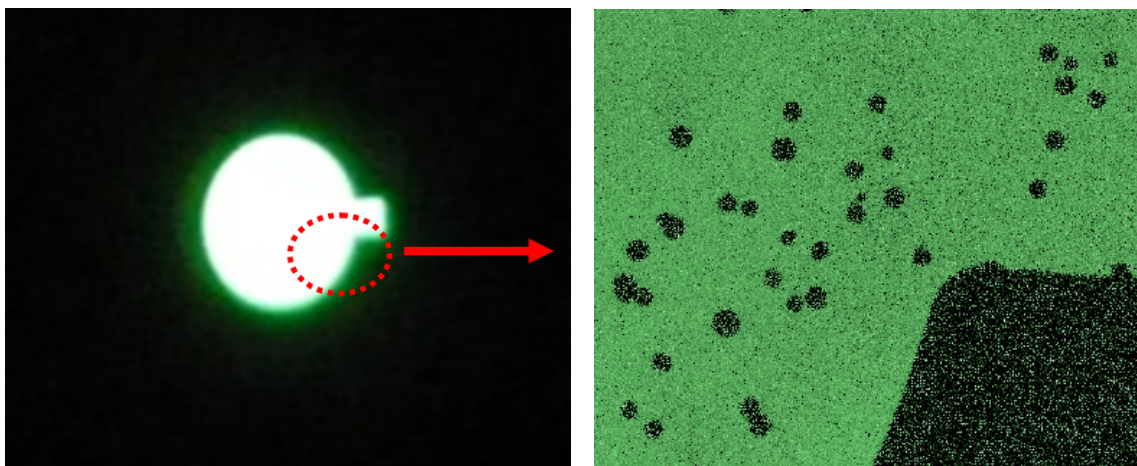
Fig. 1.13: A picture of a working OLED (on the left) and a magnified zone performed by an optical microscope in which are evident the presence of dark spots (on the right). Picture adapted from reference [33].

The growth of dark spots can ultimately cover almost the entire surface of the device and the electroluminescence can be reduced to negligible values. Many causes were reported to explain the phenomenon and today there is no unanimous consensus about their real origin. Amongst them, the dark spots were related to the presence of defects, in the manufacture process, with the presence of pin-holes more sensitive to the environmental oxygen and humidity [34] [35] [36].

A different part of studies correlates the presence of dark spots with the effect of ITO roughness extensively used as anode contact.

The roughness leads to highly invasive chemical interface reactions between the cathode and the organic compounds [37] [38] [39] and favours the further spread of the environmental agents degrading the organic materials.

However, beyond the real root causes of the phenomenon, it always occurs with the formation of "bubbles" on the cathode surface (figure 1.14), with the subsequent metal "delamination" that no longer adheres (figure 1.15).

The nature of these bubbles and their typical size, between units and tens of microns, was evaluated through SEM (Scanning Electron Microscopy) system LEO-1530 Gemini manufactured by Zeiss.
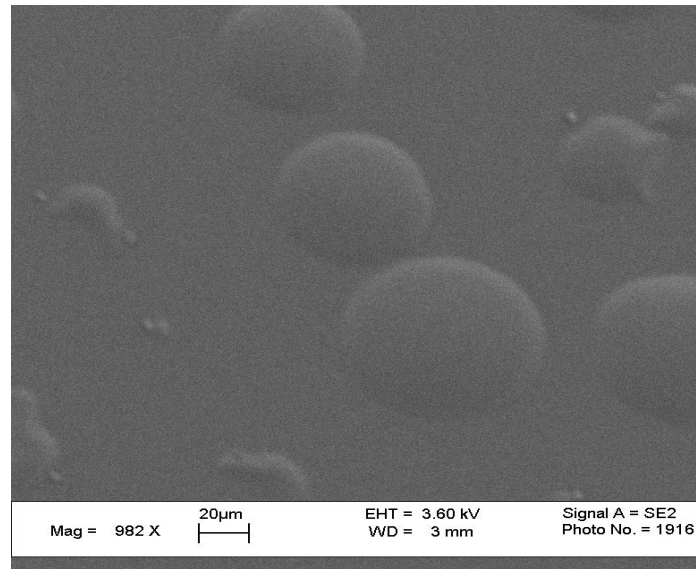
Fig. 1.14: A SEM picture in which it is evident the formation of bubbles on the cathode surface caused by the aging process. Picture adapted from reference [40].
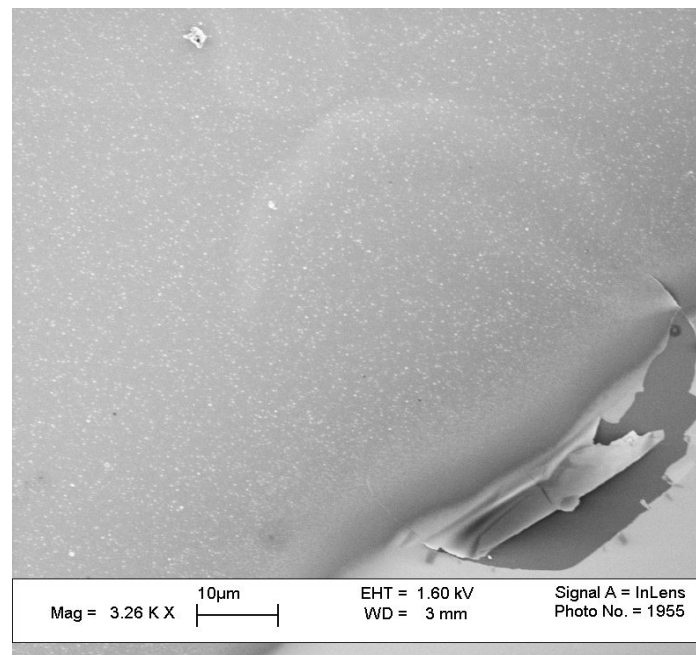
Fig. 1.15: A SEM picture of the metal delamination that can occur after the bubbles formation. Picture adapted from reference [40].

This phenomenon has even widely observed in our measures and as observed if the devices are not encapsulated, the presence of "bubbles" on the cathode is widely diffused. These results confirm, if it were necessary, that the possibility of make devices with long

half-life, passes through the devices isolation from the external environment.

These considerations are even more valid where you cannot exclude the effects of parallel local heating especially at high applied fields that cause increase of velocity in the aging process.

1.6.2 Glass transition (DSC)

Another aspect that can give important element to study the limits of organic semiconductor is the knowledge of the phase transitions such as melting, glass transitions, endothermic or exothermic decompositions, that can give elements to determine the device operational stability.

One of the most used methods is the differential scanning calorimetry (DSC) that is a thermo-analytical technique in which the difference in the amount of heat required to increase the temperature of a sample and reference are measured as a function of temperature [41]. The sample and the reference are maintained at nearly the same temperature throughout the experiment.

These transitions involve energy changes or heat capacity changes that can be detected by DSC with great sensitivity.

In this case we used this technique to have a comparison term in the understanding of our electrical measurements taking into account the temperature evolution of chemical parameters for our materials.

In figure 1.16, is shown a possible graph during a DSC measure for an organic compound in which is possible to distinguish three different phases that came one after one growing the temperature: the glass transition, the crystallization and the melting [42].
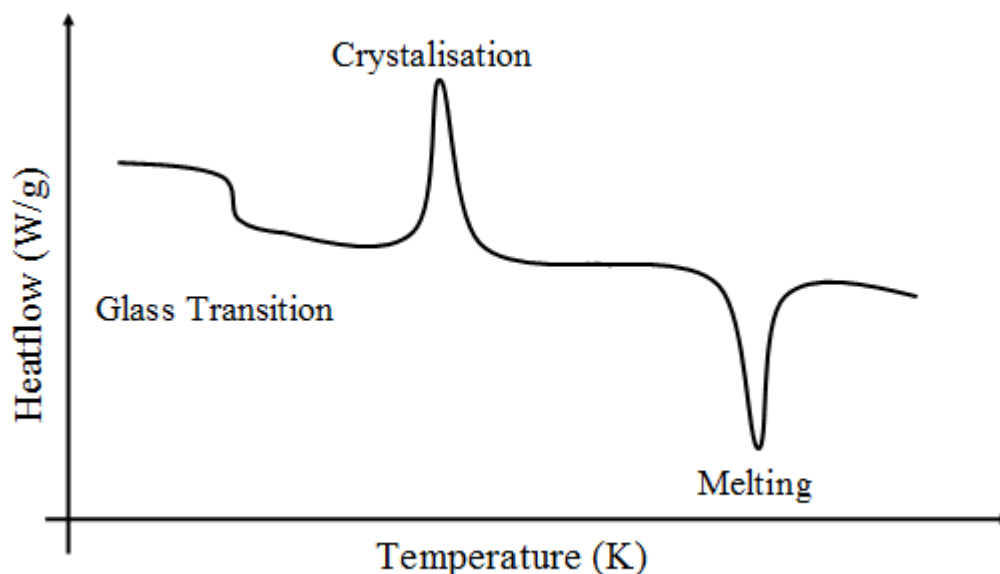
Fig. 1.16: An example measure made by the DSC technique on a polymer.

The instrument used for our purposes is a Jupiter STA449F3 produced by NETZSCH. The material that here we tested for an example purpose and also to introduce a part of our work was the small molecule TPD (N,N' - Bis(3-methylphenyl) - N,N' - diphenylbenzidine) which is often used as hole transporter layer (HTL) in OLED devices. In particular, we want to identify the region of glass transition to justify and analyze anomalies in the electrical transport in the same thermal region, anomalies that we will present in the next chapters.

Using a scanning speed of 10 K / min we obtained the graph that you can see in figure 1.17. It is possible to observe that the measure it is composed of a heating ramp of temperature, a cooling ramp, and a second heating ramp.
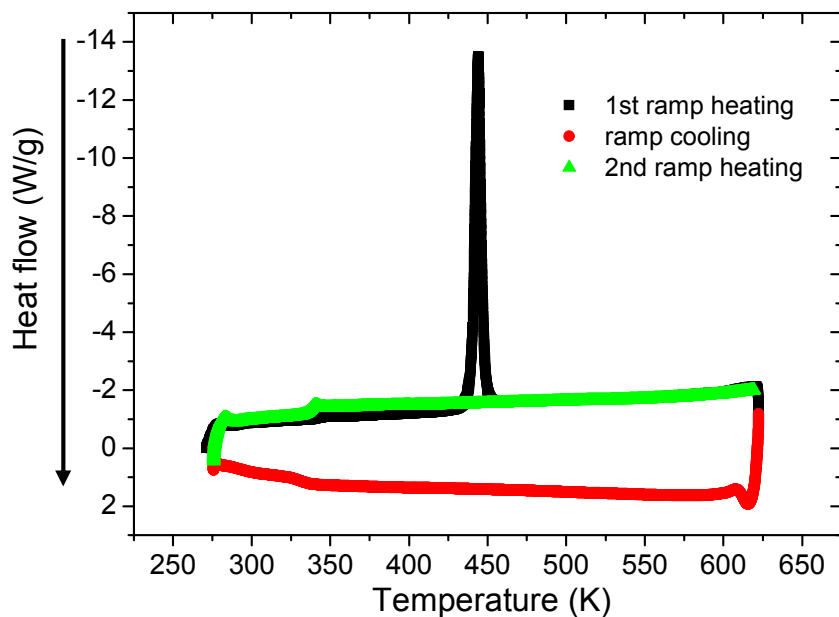
Fig. 1.17: DSC graph relative to the TPD small molecules, in green is reported the curve related to the second heating ramp.

It was realized a second heating ramp, because during the first ramp, in which it is possible to distinguish only the fusion peach around 445 K, it was not possible to easily localize the glass transition (Tg) region. In the second heating ramp, instead, it was particularly simple to localize the Tg region, as it is possible to observe from figure 1.18 in the temperature range between 300 K and 360 K.
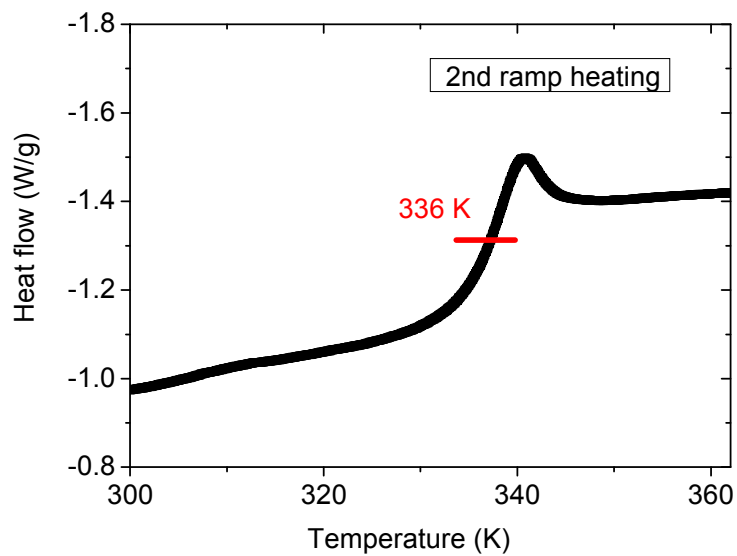
Fig. 1.18: TPD glass transition temperature and relative region

From the elaborated data it result a Tg of about 336 K and a temperature region that can be localized, more or less, from 330 K to 340 K

References

[1] DisplaySearch prediction www.displaysearch.com

[2] Colin J. Humphreys, "Solid-State Lighting", MRS Bulletin, Vol. 33 (2008)

[3] P. Cinzano,P F. Falchi, and C. D. Elvidge "The first World Atlas of the artificial night sky brightness" Mon. Not. R. Astron. Soc. 328, 689–707 (2001)

[4] M. Stössel, J. Staudigel, F. Steuber, J. Simmerer, A. Winnacker: Appl. Phys. A, 8, 387 (1999)

[5] G. E. Jabbour, B. Kippelen, N. R. Armstrong, and N. Peyghambarian: Appl. Phys. Lett, 73, 9 (1998)

[6] Soo Young Kim, Woong-Kwon Kim, Kwang Young Kim, Yoon-Heung Tak, Jong-Lam Lee: Electrochemical and Solid-State Letters, 9, 1 (2006)

[7] G. E. Jabbour, Y. Kawabe, S. E. Shaheen, J. F. Wang, M. M. Morrell, B. Kippelen, N. Peyghambarian: Appl. Phys.Lett., 71, 13 (1997)

[8] S.M. Sze, "Physics of Semiconductor Devices", Wiley, New York (1981)

[9] Jingze Li, Masayuki Yahiro, Kenji Ishida, Hirofumi Yamada, Kazumi Matsushige, Synthetic Metals, 151, 141–146 (2005)

[10] L.S. Hung, C.W. Tang, M.G. Mason, Appl. Phys. Lett. 70, 152 (1997)

[11] H. Bässler, Phys. Status Solidi B 175, 15 (1993)

[12] P. E. Burrows, Z. Shen, V. Bulovic, D. M. McCarty, and S. R. Forrest: J. Appl. Phys. 79 (10), 15 (1996)

[13] I. D. Parker, Carrier tunneling and device characteristics in polymer light-emitting diodes, J. Appl. Phys. 75 (3), 1656-1666 (1994)

[14] S. Ouro Djobo, J.C. Bernede, N. Kossi, Journal of Materials Science: Materials in Elactronics 15, 579-582 (2004)

[15] M. Koehler, I. A. Hummelgen, Appl. Phys. Lett. 70 (24), 3254-3256 (1997)

[16] N. K. Patel, S. Cinà, and J. H. Burroughes: IEEE Journal on selected Topics in quantum electronics, Vol. 8, No. 2 (2002)

[17] P. W. M. Blom, M. J. M. de Jong, and S. Breedijk Appl. Phys. Lett. 71, 930 (1997)

[18] P. W. M. Blom, M. C. J. M. Vissenberg, J. N. Huiberts, H. C. F. Martens: Appl. Phys. Lett. 77, 2057 (2000)

[19] B. K. Crone, I. H. Campbell, P. S. Davids, D. L. Smith, C. J. Neef, and J. P. Ferraris, "Device physics of single layer organic light-emitting diodes," J. Appl. Phys., Vol. 86, pp.

5767–5774 (1999)

[20] B. K. Crone, P. S. Davids, I. H. Campbell, and D. L. Smith: "Device model investigation of bilayer organic light emitting diodes", J. Appl. Phys. 87, 1974 (2000)

[21] M. A. Baldo, D. F. O'Brien, Y. You, A. Shoustikov, S. Sibley, M. E. Thompson, and S. R. Forrest, "Highly efficient phosphorescent emission from organic electroluminescent devices," Nature, vol. 395, p. 151 (1998)

[22] M. A. Baldo and S. R. Forrest, Phys. Rev. B, 62, 10958-10966 (2000).

[23] M. Baldo and M. Segal, "Phosphorescence as a probe of exciton formation and energy transfer in organic light emitting diodes". Phys. Stat. Sol. (a) 201, No. 6, 1205-1214 (2004)

[24] T. Förster, Faraday Soc. 27, 7-17 (1959).

[25] M. A. Baldo, M. E. Thompson, and S. R. Forrest, Nature 403, 750-753 (2000).

[26] By Jia-F. Wang, Yutaka Kawabe, Sean E. Shaheen, Michael M. Morrell, Ghassan E. Jabbour, Paul A. Lee, Jeffrey Anderson, Neal R. Armstrong, Bernard Kippelen, Eugene A. Mash, and Nasser Peyghambarian Adv. Mater., 10, No. 3 (1998)

[27] W. M. Su, W. L. Li, Q. Xin, Z. S. Su, B. Chu, D. F. Bi, H. He, and J. H. Niu, Appl. Phys. Lett., 91, 43508 (2007)

[28] J. Thompson, R. I. R. Blyth, M. Mazzeo, M. Anni, G. Gigli, and R. Cingolani, Appl. Phys. Lett., 79, 560 (2001)

[29] Naoki Matsumoto, Masakazu Nishiyama, and Chihaya Adachi, J. Phys. Chem. C, 112, 7735-7741 (2008)

[30] Michel Schaer, Frank Nüesch, Detlef Berner, William Leo, and Libero Zuppiroli, "Water Vapor and Oxygen Degradation Mechanisms in Organic Light Emitting Diodes", Advanced Functional Materials, 11, 116. (2001)

[31] S. Jung, N.G. Park, M.Y. Kwak, B.O. Kim, K.H. Choi, Y.J. Cho, Y.K. Kim, Y.S. Kim, Surface treatment effects of indium–tin oxide in organic light-emitting diodes Optical Materials, 21, 235-241 (2002)

[32] D. Y. Kondakov, R. H. Young, J. R. Sandifer, and C. W. Tang Journal of Applied Physics Vol. 93, No.2 15 (2003)

[33] Paolo Vacca, "Technology and electro-optical characterization of organic semiconductor devices", PhD. Thesis (2007)

[34] T.P. Nguyen, P. Jolinat, P. Destruel, R. Clergereaux, J. Farenc, Degradation in organic light-emitting diodes, Thin Solid Films, 325, 175-180 (1998)

[35] Haichuan Mu, Hui Shen, David Klotzkin, "Dependence of film morphology on deposition rate in ITO/TPD/Alq3/Al organic luminescent diodes", Solid State Electronics, 48, 2085 (2004)

[36] J. Steiger, S. Karg, R. Schmechel, H. von Seggern "Aging induced traps in organic semiconductors" Synthetic Metals, vol. 122, 49-52 (2001)

[37] Aziz et al, Applied Physics Letters, vol. 72 pp 2642-2644 (1998)

[38] P. E: Burrows et al, Applied Physics Letters, vol. 65, pp. 2922-2924, (1994)

[39] D. Kolosov et al, Journal of Applied Physics, vol. 90, pp. 3242-3247 (2001)

[40] Maria Grazia Maglione, "Dispositivi elettroluminescenti organici: tecnologie di fabbricazione e metodologie di caratterizzazione", PhD. Thesis (2005)

[41] M. J. O'Neill, Anal. Chem., 36, 7, pp. 1238-1245 (1964)

[42] L. E. Nielsen, "Mechanical properties of polymers and composites", Vol. 1 Marcel Dekker, inc. New York (1974).

CHAPTER II

"Electrical characteristics of organic semiconductors"

In this chapter the dependence of the mobility in organic compounds on the applied electric field will be shown, analyzing two different charge transport theories: the "Space Charge Limited Current" and the "Tunnelling". From the experimental data at high applied fields the tunnelling, in particular situations, dominate and it has been observed that the charge carrier injection at metal/polymer interfaces can be described by the Fowler Northeim (FN) expression. In this section the electrical properties of the adopted materials will be analyzed with an extensive study on device temperature limits, studying the temperature-dependent electrical properties of the organic light-emitting diodes and the thermal dissipation by means thermal-map of the working device.

2.1 Charge transport in disordered materials

Typically, organic materials employed in OLED purpose are not doped, and have a density of states in a manner that at room temperature there is no free charge and the materials shown properties comparable to the insulators. Because of we are in the presence of disorder matter, after the injection from the electrodes into the organic film, the transport mechanism is subject to the hopping events between molecules.

More in general, polymers offer the advantage over small molecules of having delocalized molecular orbitals, as long as the conjugation is preserved. This means that while electrons and holes in small molecule layers can only hop from one molecule to its neighbour, the transport properties of conjugated polymers are a combination of motion along the delocalized orbitals and hopping between different polymer chains. The carrier's mobility is normally field-dependent in systems where the transport is limited by hopping mechanisms. This is because the barrier for hopping is lowered by the presence of the field, therefore affecting the hopping probability.

2.2 Electrical transport (Poole-Frenkel approximation)

The exact dependence of the mobility on the electric field surely depends on the properties of the material and the fabrication process, but it has been found that in small molecules and conjugated polymers the Poole–Frenkel (PF) [1] model (eq. 2.1) often fits quite well the experimental data

$$\mu(E) = \mu_* \exp\left(\frac{-\Delta}{KT}\right)\exp\left(\gamma\sqrt{E}\right) \qquad (2.1)$$

where E is the electric field, where Δ is the activation energy, k the Boltzmann's constant, μ_* the mobility prefactor, and γ the electric-field coefficient to the mobility due to the interaction between charge carriers and randomly distributed permanent dipoles in semiconducting polymers. The field independent quantity present in the formula 2.1 is usually identified as the zero-field mobility μ_0.

Two of the most straightforward techniques used to measure mobility in organic materials are time of flight (TOF) [2-6] and measurement of the space charge limited current (SCL).

In the former case a layer of organic material is sandwiched between a semitransparent (normally a thin Al layer) and a reflective electrode (a thick Al layer).A thin sheet of electron-hole pairs is then formed close to the transparent electrode by using a light pulse (provided that the organic film is much thicker than the absorption depth of the optical excitation). In presence of an applied electric field, the electrons (or holes depending on the direction of the electric field) are then driven to the other electrode and collected. The carrier mobility can then be determined from the measured transit time (t) since it is related to the applied field (E) and the film thickness (d) by:

$$\mu(E) = \frac{d}{Et} \qquad (2.2)$$

assuming the transport is nondispersive.

The disadvantage of the TOF technique is that the mobility is measured on films much thicker (1 μm) than those normally used in OLEDs (100 nm or less). Since the film

preparation method for thick films is very different from that of thin films, the resulting morphology can give rise to different charge transport characteristics to those seen in thin films.

The other possibility, more suited to thin film measurements, is to derive the mobility directly from current–voltage measurements on OLED-like single carrier structures. When the barrier for charge injection is no longer the limiting factor (this means either a low barrier to injection or high enough electric field), the current is limited by the mobility of the carriers inside the organic layer. The charge present inside the organic layer produces an electric field and the total local electric field at any point within the device is a result of both the internal and externally applied fields. At high current densities the internal electric field can be sufficient to almost cancel the applied electric field at the injecting contact, and the contact becomes ohmic. In this regime is possible to study the material bulk properties in a more simple way, trying to correlate the theoretical models to the experimental data to give the right explanations to the observed phenomena.

2.2.1 Space Charge Limited Current versus Tunnelling

In particular, if the current is limited by the space charge present in the organic film, we are in the presence of the so called space-charge-limited current (SCLC) regime.

Here, the total charge inside the device is constant, and in order to inject extra charge, the same amount must be extracted from the other contact. This is the maximum current that can be transported by the device, and of course, depends on the mobility of the carriers. For single carrier devices, the Mott–Gurney law [7] with a field-dependent mobility describes the SCLC in most of the organic materials (2.3):

$$j_{SCLC} = \frac{9}{8}\varepsilon_0\varepsilon_r\mu\frac{V^2}{d^3}$$

(2.3)

This equation is derived neglecting diffusion and with the boundary condition that the electric field at the injecting contact vanishes.

However another important aspect in the organic semiconductor is the presence of free-

traps that can surely are able to change the electrical behaviour and the mobility versus the applied field.

In the presence of traps the current is in general lower and the quadratic field dependence is retained in the case of discrete trap levels only (or when all traps are filled). Then (2.3) has to be modified by a factor $\theta=n/(n+n_t)$ equal to the ratio of free carriers to the total number of carriers. If traps are distributed in energy they will be gradually filled with increasing electric field (i.e. θ depends on the electric field) and the current will increase faster than quadratic until all traps are filled.

In this case the so-called trap-charge limited current (TCLC) with the parameter $l=E_t/k_BT$ derived from the trap distribution is given by [8]

$$j_{TCLC} = N_c\mu q\left(\frac{\varepsilon\varepsilon_0 l}{N_r q(l+1)}\right)^l\left(\frac{2l+1}{l+1}\right)^{l+1}\frac{V^{l+1}}{d^{2l+1}}$$

(2.4)

If the assumption of a field-independent charge carrier mobility is dropped, an analytic solution for arbitrary $\mu(F)$ dependence is still possible in the absence of traps, however, $j(V)$ can then be given in parametric form only [9].

In true, in literature, there are many papers in which the TCL model is greatly criticized, because it was originally formalized to justify the electrical properties for material with delocalized bands (and this cannot be attributed to the organic materials under our attention) [10-12].

Recent work on the I–V characteristics of single-layer or double layer for polymers and small molecules in OLED devices has suggested that tunnelling from contacts into the conduction and valence bands of the organic layers limits current flow [13]. Even for polymer-based devices, however, the data show significant departures from this model, and alternative processes, including SCL conduction, have been proposed [14]. Often, these energy barriers are taken as intrinsic properties of the organic–organic or organic–metal junctions, although chemical reactions between the typically low-work-function electrodes and some EL materials [15] have been shown to substantially lower the barrier at the interfaces. This can introduce new electronically active states into the HOMO–LUMO band gap of the organic material, resulting in ohmic injection from the contacts.

Nevertheless, to fit the data from molecular OLEDs to a tunneling model, we assume a triangular barrier at the electrode–organic interface, so that the current follows the Fowler–Nordheim equation [16] (see also Chapter I).

From the experimental data at high applied fields the tunnelling effectively seems to dominate and it has been observed [17, 18] that the charge carrier injection at metal/polymer interfaces can be described by the FN tunneling expression. The current-voltage characteristics of devices which operate based on this mechanism are generally presented in the so-called Fowler–Nordheim plots (i.e., $\ln(J/E^2)$ vs $1/E$) where the expected behavior for FN tunneling is expressed as a straight line and where J and E are the current density and the applied electric field respectively.

In addition, we have also to say, that the pronounced temperature dependence of current at constant voltage in experimental data seems to be contrary to the Fowler–Nordheim equation which predicts almost no temperature dependence and it has to be adjusted with further investigations [19]. Finally, the deviation from a straight line in FN plots is shown as a consequence of the fact that the Fermi–Dirac distribution function is not a step function at temperatures different than absolute zero [19].

2.3 DC analysis and temperature investigation

Many studies have been reported about glass transition in organic materials [20-22] and in particular its correlation to the OLED's (Organic Light Emitting Diodes) degradation, but it is difficult to relate the glass transition and the device operating limits [23-25]. In particular, the glass transition region is very difficult to identify as it depend by a lot of parameters (thickness of the sample, temperature rate and environmental parameters). In this section a study on the glass transition phenomena is reported with the aim to highlight the limits of the device under investigation and to understand the mechanism related to the optical failure at this temperature region.

We investigate the behaviour of the emissive species, and the reasons to explain the differences between the optical and the electrical failure of the device during the currentvoltage (I-V) measurement. We examin the possibility that the optical failure is mainly ruled by the glass transition of hole transport layer (HTL).

There are many papers dealing with the thermal aging effects of OLEDs [26–28] which show how an OLED behaves differently during its lifetime for various working regimes at different substrate temperature [26]. In particular, the higher the current density inside the device, the faster the performance degradation because of the current induced heating (self-heating). To increase the operational stability of OLEDs, several strategies have been developed [27, 28], including the study of the thermal degradation mechanism too, in particular the trend of electroluminescence versus time at different temperatures [29].

We performed electro-optical measures versus temperature to explain the mechanisms governing the dynamics of glass transition, eventually correlating such mechanisms to device limitations.

2.3.1 OLED devices fabrication and initializing set-up

We have manufactured OLED devices on Corning 1737 glass substrate, with 150 nm thick commercial ITO layer, with a sheet resistance of $10\Omega/\square$. The substrates were cleaned with deionised water, detergent and ultrasounds and dried in oven at 115°C for 2 hours. The anodes were patterned through inverse photolithography and HCl-based solution etching. The deposition of organic layers and cathode was carried on in a high

vacuum evaporator chamber. The organic layers were thermally evaporated sequentially and there was no vacuum breaking between their depositions. The base vacuum was always around 10^{-7} mbar and the growth rate for the organic layers was between $1 \div 2$ Å/s. The vacuum was broken before the aluminium cathode deposition by thermal evaporation, through shadow mask; the growth rate was about $4 \div 5$ Å/s. The OLED structure under investigation was: ITO/TPD/Alq$_3$/Al.
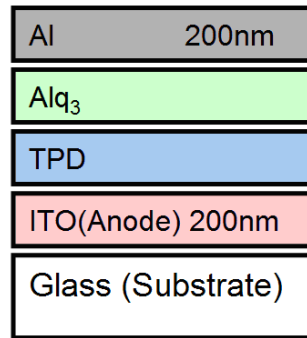
Fig 2.1: The OLED bi-layer structure under investigation where the Alq3 is used like ETL and EML while the TPD like HTL.

We considered a very standard device structure because we were focused on the device limitations. Furthermore, TPD was selected for its low glass transition temperature [30][31][32], in this way we can easily evaluate the HTL (hole-transport layer) morphology change without damaging the emitter layer and easily evaluate its influence on the device behaviour.

Current-voltage (I-V) characteristics have been measured using a Keithley 2400 Power Supply SourceMeter in voltage mode with constant increment steps and delay time of 1 s before each measurement point. Electroluminescence (EL) analysis was performed using a photodiode (Newport 810UV) connected to a Keithley 6517A Electrometer.

The temperature measurements were performed with a Janis cryostat equipped with an optical quartz window, on which was mounted the photodiode, and a heater connected to a Lake Shore 331s temperature controller. The temperature was measured both in proximity of the device and on the heater by two thermocouples. The cryostat base pressure during the measurements was around 10^{-4} mbar.

2.3.2 DC characterization and temperature dependence

To investigate the operational limits of our basic OLED structure, current-voltage (I-V) and electroluminescence-voltage (EL-V) measurements have been performed at increasing driving voltages, until the device electrical and optical "breakdown".

In figure 2.2 it is possible to analyze the electrical failure for several thickness combinations of holes and electron transporter layers. In particular the HTL/ETL thicknesses are respectively: 20nm/30nm, 40nm/60nm, 20nm/60nm, 70nm/50nm. From the electrical behaviours is possible to note a change in the failure point depending on the thickness and in particular on the applied field distribution on the organic layers.

Above all, we can note a progressively shift to high voltages increasing the device's thickness, giving us elements to justify it with a thermal activation caused by the total power dissipation.
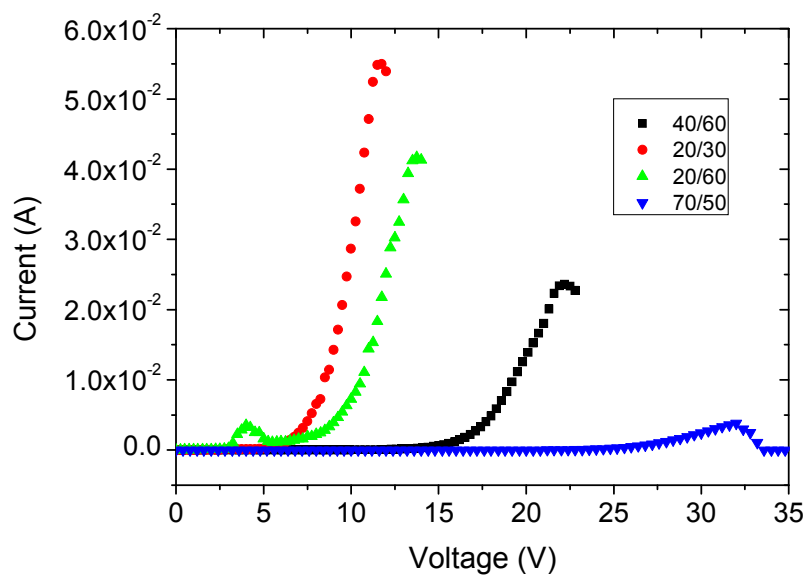
Fig. 2.2: I-V curves changing the device thickness and the relative "high field" electrical failures.

If now we focused on a particular device (i.e.: 40nm/60nm) is possible to clearly note that current and electroluminescence get a maximum value before rapidly decreasing as a function of the applied voltage. In any case, the experimental findings reveal that the

"optical failure" occurs at lower voltages (about 20 V) in comparison with the "electrical failure" (about 22 V) (see figure 2.3).
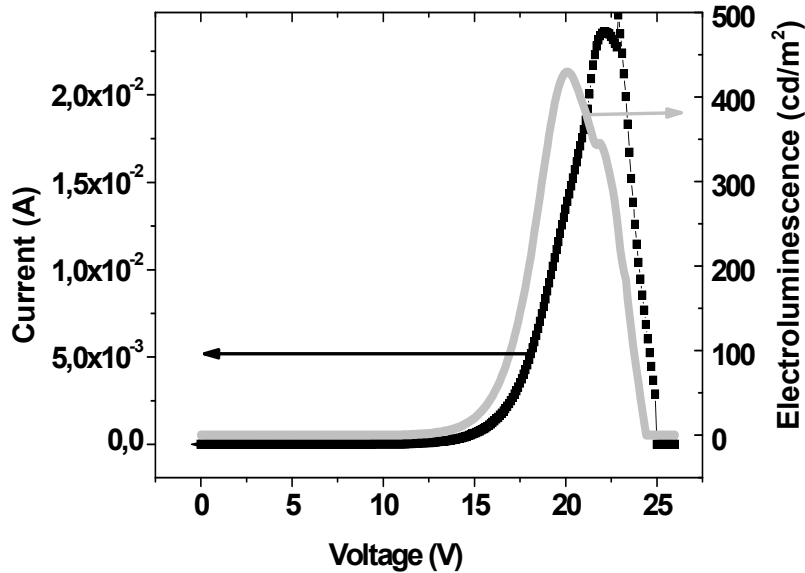
Fig. 2.3: Typical I-V and EL-V characteristics for an ITO/TPD/Alq$_3$/Al device and their failures (HTL/ETL = 40nm/60nm).

Besides, if we observe figure 2.4 we will see a slightly decrease in power consumption for both, electrical and optical, failures increasing the total thickness but it can be easily attributed to the difference in the thermal dissipation that surely will change with the device thickness. These considerations cannot be applied for too thick devices, because of the applied field has to be very high to lead an optical failure and so it can be too much high for the thin metal cathode that is damaged and cause the contemporary optical and electrical failures.
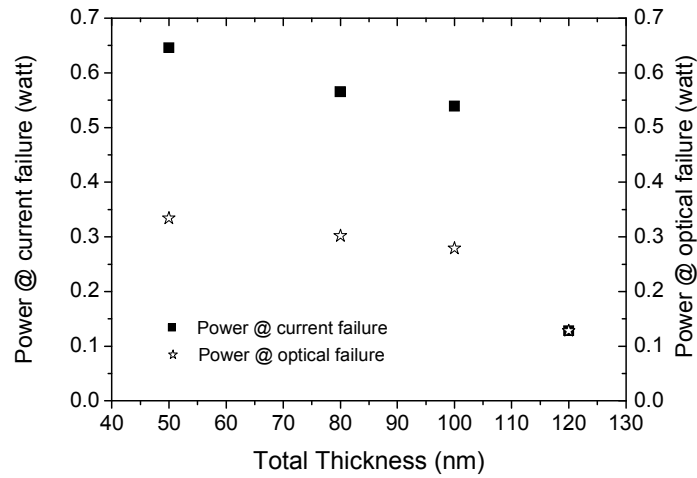
Fig. 2.4: The impact of the device thickness on electric and optical failures
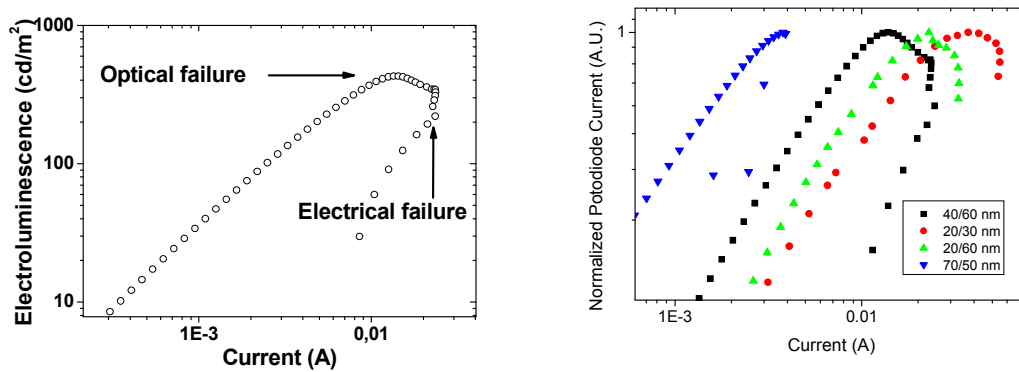
Fig. 2.5: Electroluminescence vs. device current, displaying both optical and electrical failures for 40nm/60nm device (right). The same graph related to different devices thicknesses (left).

A complementary picture of this situation is given in figure 2.5, where the electroluminescence is plotted versus the device current and the different failure events are more directly evidenced.

To gain more insights on this feature, an alternative procedure has been followed, driving the OLED (40nm/60nm) at a fixed voltage (15 V) and forcing externally the device temperature by a resistive heater.
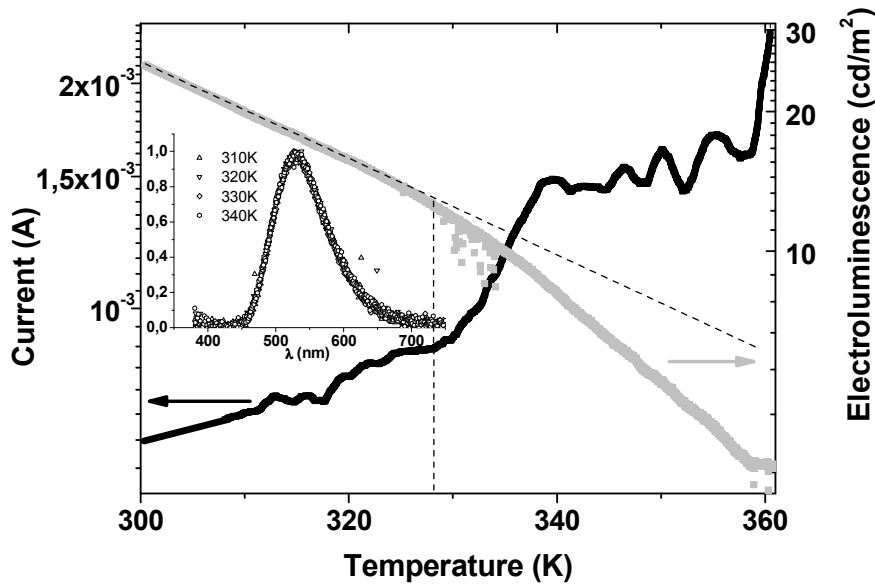
Fig. 2.6: Electroluminescence and device current as function of temperature for the TPD/Alq$_3$ OLED device at V = 15 V. (Inset) Device spectra (arbitrary unit) versus temperature.

This driving voltage has been chosen to be higher than the optical onset voltage but considerably lower than breakdown values, in order to limit the self-heating effects. In this way, the behaviours of device current and of electroluminescence both versus temperature have been accurately monitored up to 360 K (figure 2.6).

As expected, both the current and the luminescence display temperature dependences, with peculiar features concentrated above 330 K.

In these curves, three main regions can be identified. In the first one, from room temperature to about 328 K, device current increases according to a conventional thermal activation law. On the other hand, the corresponding EL slight reduction has to be attributed to the inevitable underlying device degradation in time, mainly affecting the emission properties [33][34].

The starting value (about 328÷329 K) of the second zone is marked by a clear change in the slope of both EL and I curves. In detail, electroluminescence starts to decrease more rapidly, and in a complementary way to a faster increase of the device current. This can be interpreted in terms of a significant increase of hole traps concentration near the HTL/ETL interface, which can easily act as recombination centres with a dominant non-radiative behaviour [35]. Furthermore, a contemporaneous spectral analysis, performed

by a spectrum-radiometer and reported in the inset in figure 2.6, allows confirming that electroluminescence variation is related only to the intensity of emitted light and not to spectrum modification. It is important to outline that TPD Tg value usually reported in literature is located between 333 K and 338 K, meaning that the device response in the second region should be the most significantly affected by glass transition occurrence [30][31][32].

Finally, the third region starts at about 341 K, where the current begins displaying an unstable behaviour with significant negative differential resistance (NDR) zones. Here, TPD has completely changed its phase and the overall device behaviour should be slightly masked by the presence of Alq_3 layer, until the definitive failure at about T ~ 360 K [36][37].

2.4 Temperature limits investigation (Fowler Nodheim)

In this section we have studied with a different approach the temperature-dependent electrical properties of the organic light-emitting diodes. We have continued to use the molecular compounds, TPD (40 nm) as a hole transport, and Alq3 (60 nm) as an electron transport layer.

To observe the effect of temperature on the OLED devices, I–V characteristics were measured with a temperature variation in the range of 298 K to 360 K.

In particular, we fixed each temperature value and then we wait for temperature device equilibrium and only after we performed the measure (for the initializing set-up see 2.3.1 section). In figure 2.7 it is possible to see the I-V evolution changing the temperature with a step of five degree.
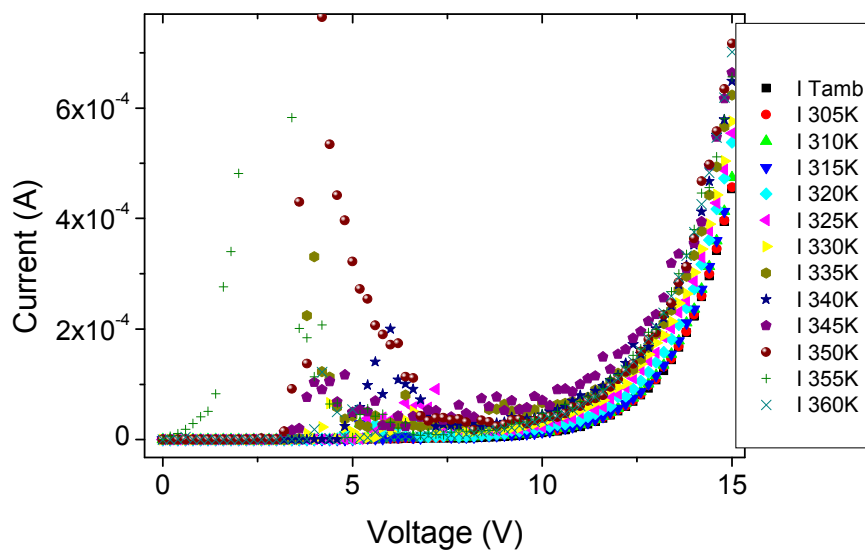
Fig. 2.7: I-V curves versus the applied temperature

Analyzing our data, especially at high voltages, the current density in the device seems to follow a sort of tunnelling model (see also inset of figure 2.8) [38][39]. This is probably due to an higher barrier for the electron injection and an higher holes mobility in the HTL compound respect to the electrons in the ETL leading to a surely unbalanced device and an electric behaviour very close to a single carrier device.
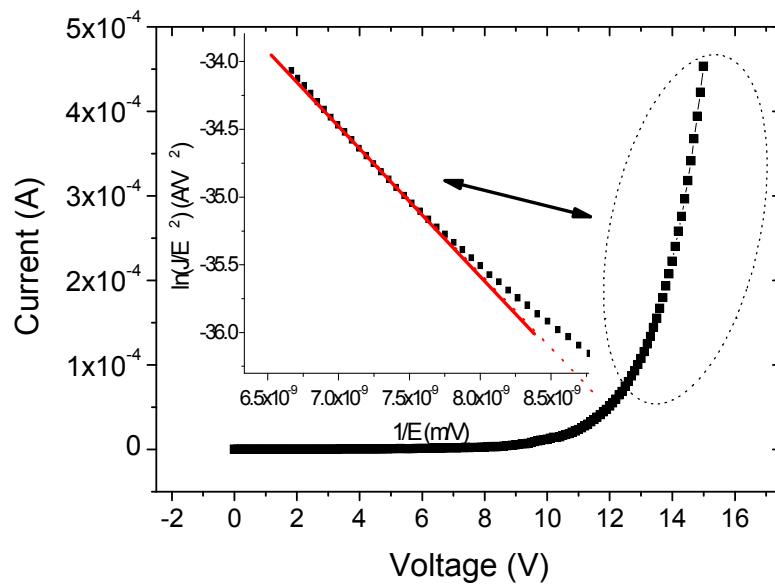
Fig. 2.8: I-V of the TPD (40nm)/Alq3(60nm) OLED device. Inset, Fowler–Nordheim tunneling plot relate to the same device

In particular, the Fowler–Nordheim tunnelling can be summarized by the simple expression already reported in Chapter I (eq. 3 and 4) and the related B parameter, in this case, is strictly connected with the barrier height (φ) between anode and HTL.

Changing the substrate temperature, it is possible to monitor the change in the electric slope (at high field) of our device including the glass transition temperature region (figure 2.9).
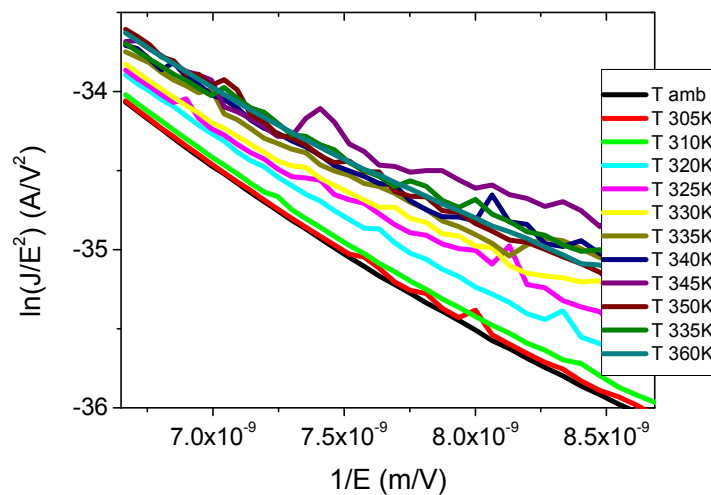
Fig. 2.9: Fowler–Nordheim tunneling plot, relate to the TPD(40nm)/Alq3(60nm) OLED device, versus temperature.

Moreover as consequence, with this kind of approach it is possible to investigate the change in the barrier height between anode and HTL due to the organic compound reorganization and it is possible to give possible explanation to the data reported in figures 2.3 and 2.5.

It is possible to observe, in figure 2.10, that the change in the slope at high field is possible to bring back to the different way in which the current is growing at lower voltages that lead also to a higher noise level in the data.
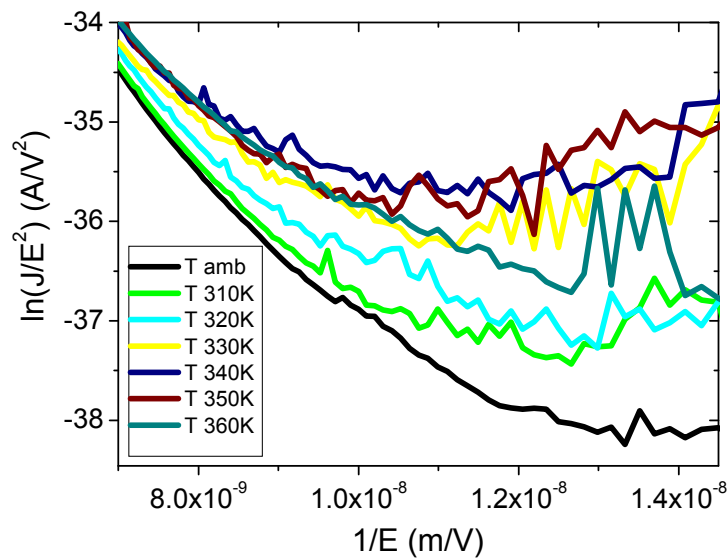
Fig 2.10: F–N plot versus temperature. It is evident the different way in which the current is growing at lower voltages.

In a first temperature region (until 320 K) the B parameter, related to the barrier height, decrease slightly with the temperature, as expected [19,38] (figure 2.11). From 325 K to 340 K, we can define the glass transition region; here, B value changes drastically until 340 K, where the data start to have a more uncertain behaviour probably the TPD molecules find another unstable state.

This rapid variation of B parameter in the glass transition region probably is due to a reorganization of the energy levels associated with the traps in the TPD layer (see also figure 2.10) [35] and a consequent modification of the TPD conduction properties. Furthermore, from figure 2.6 and figure 2.11, these devices are able to transport current

also at temperature higher than the glass transition one.
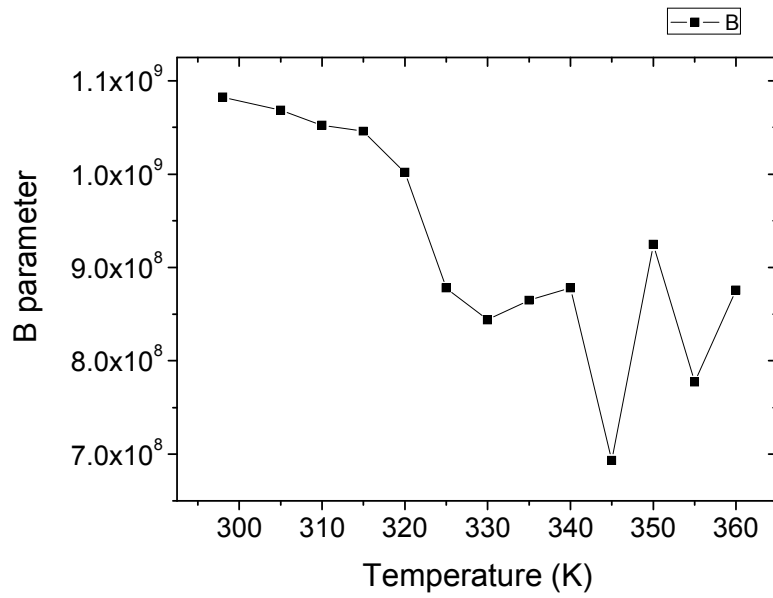
Fig. 2.11: The F–N B parameter versus the substrate temperature. It is possible to see a strong variation in the B value around 325 K.

2.5 Thermal stress (IR measure)

In this paragraph, we present a correlation study between the working temperature of OLEDs (Organic Light Emitting Diodes) and the electroluminescence and driving voltage changes. The aim is to investigate the relationship between the operating temperature and the aging mechanisms, keeping in mind what we already exposed.

For this experiment, the measurement set-up was (see also figure 2.12):

• an IR (Infrared) camera (AVIO neo-thermo TVS-700), to evaluate the temperature of device,

• a CCD-telescope to collect and send the light to a spectroradiometer (Optronics Laboratories OL770) by an optical fibre,

• a Source-meter (Keithley 2400) to drive the device and to perform the electrical measurements.

The calibration of the IR camera has been performed using a blackbody. We have compared the read temperature for it with the one from the substrate, and then we adjusted the response of the camera to obtain the same readings. In this way, we also obtained the emissivity of the substrate, ε, found to be about 0.89.

Thermal measurements are made imaging the surface of the glass substrate through which the light emission can be seen.

To correctly evaluate the temperature of a working OLED, it is necessary to take into account the difference in temperature between the OLED side of the glass and the mentioned surface. In order to do this, the temperature difference between the two faces has to be previously measured; with a heat flux-meter, we have heated one face of a bare substrate, measuring the temperature using two thermocouples placed on both sides of the sample. Therefore, the measured temperature on the glass can be directly correlated to the temperature of the device.
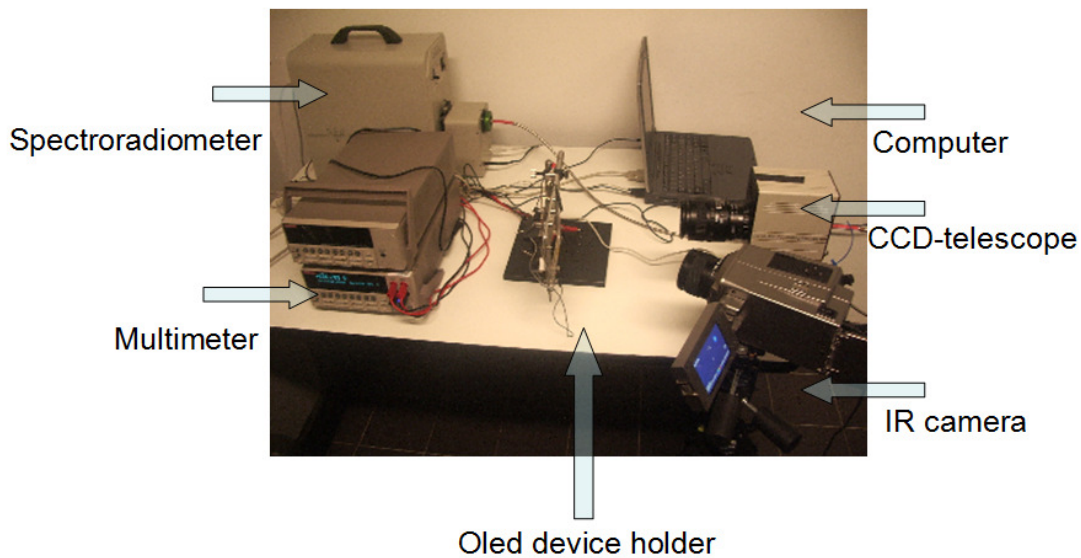
Fig. 2.12: A photo about the measurement set-up

As shown in figure 2.13, by plotting normalized electroluminescence and current intensity versus voltage in semilog scale, for a TPD/Alq3 (20nm/30nm) device, several operating regions can be observed. The "optical failure voltage" V^* can be defined as the voltage at which the maximum light intensity plateau intersects the polynomial part of the EL curve; in a similar way, the "electrical failure voltage" can be defined using the I-V curve. For the OLED of fig. 5, $V^* \approx 9.75$ V, 2 V before the electrical failure voltage.
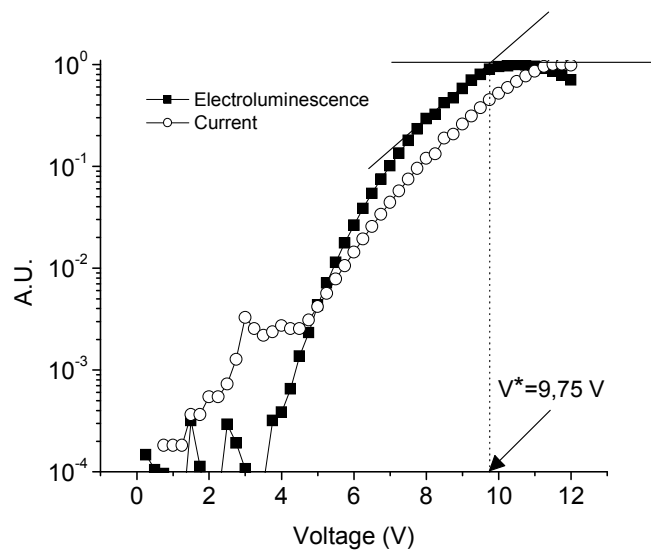
Figure 2.13: The optical decay region can be defined starting at the intersection of the EL plateau with the adjacent polynomial branch of the curve.

Monitoring the temperature during the I-V and the EL-V curves, we have found that performances degradation of devices is strictly related to the glass transition temperature (Tg) of organic layers, and that electrical failure is reached only for temperatures higher than Tg.
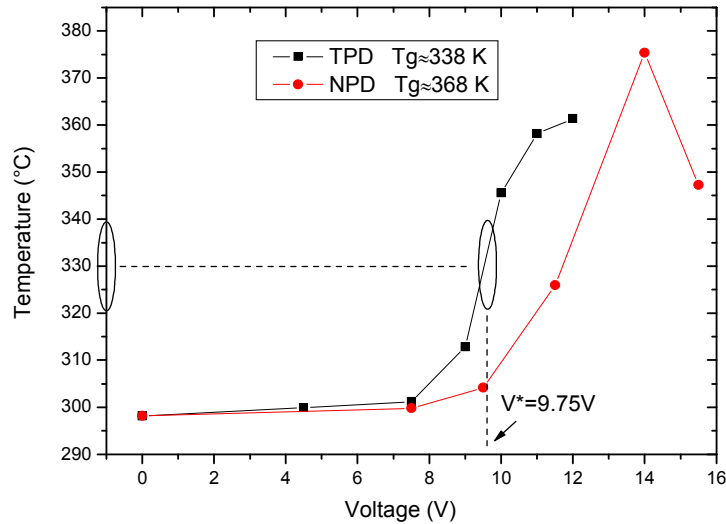
Figure 2.14: The optical failure, shown in figure 1, happens when the operating temperature T* is close to the glass transition temperature of TPD (Tg~338 K). To complete our analysis in this picture is shown the temperature behaviour for a device with an NPD (Tg~368) layer instead that the TPD one.

The measurement of the temperature has to be performed in "stationary" conditions, so we have experimentally determined how long the device power supply has to be held at a fixed voltage to obtain a stable temperature. We call this time "hold time" and it should be long enough to end the thermal transients of the system and short enough to minimise the electrical stress. After this hold time, we acquired the distribution of the temperature on the substrate surface (thermal map) and we tried to relate it to the device's physical properties (see figure 2.15).
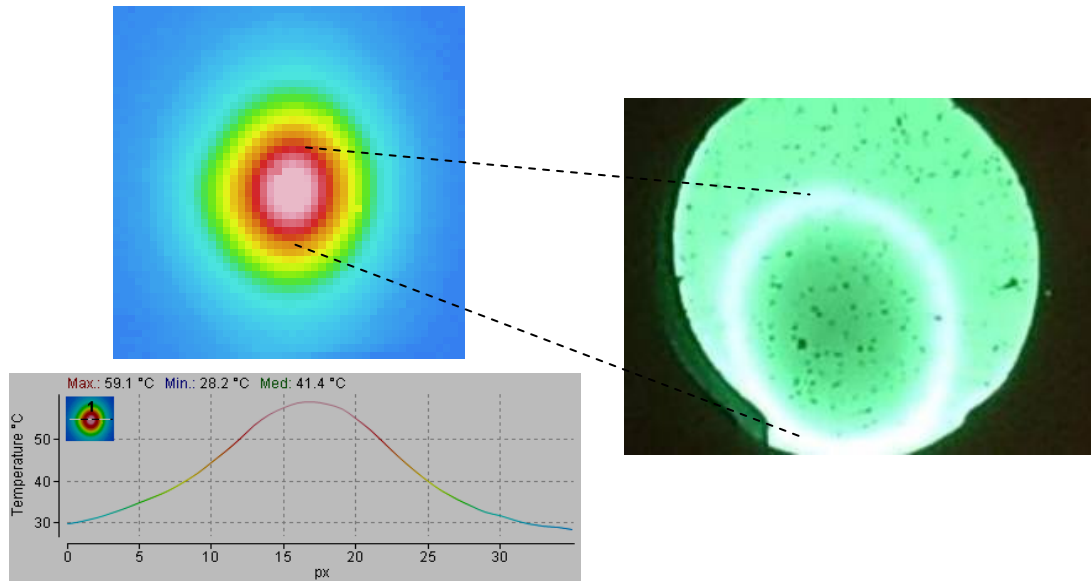
Fig. 2.15: (Right) Thermal maps taken from the glass side and temperature profile along a cut-line passing through the centre of the map (px: pixels of the map). (Left) OLED picture, during operation, that shows an evident degradation of electroluminescence. The optical failure starts from the inside of the device.

In figure 2.15, we can observe that the temperature is higher in the inner part of the device, because the boundaries of its active area exchange heat with the adjacent colder non-active areas. For our purposes, the highest temperature on the surface of the whole device was considered to get an estimation of the thermally-induced performance decay. From the experimental data (see figures 2.15 and 2.16), we have observed that highest temperature is not located in the geometrical centre of the device.
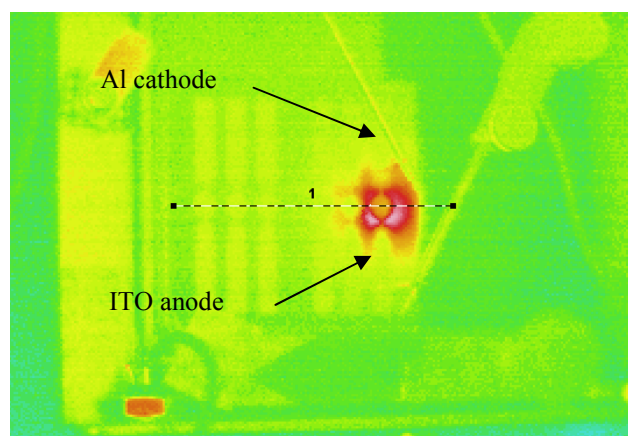
Fig. 2.16: A thermal map of the OLED device the cathode side. The higher temperature in proximity of the power supply contact on ITO anode generates the asymmetry bottom-to-up in the thermal map.

This fact can be explained considering that the electrical resistivity of ITO ($4*10^{-4}$ $\Omega*cm$) is higher than the resistivity of the Aluminium ($2*10^{-6}$ $\Omega*cm$). Because of this difference, as the distance from power supply contact on ITO anode increases, current density inside the device reduces, so a non-uniformity of the thermal power generation can be observed in the same direction (figure 2.16). In this point of higher temperature, driving the device at voltages approaching V*, the electrical stress leads to a local optical failure which can be attributed to a thermally-induced glass transition in the TPD.
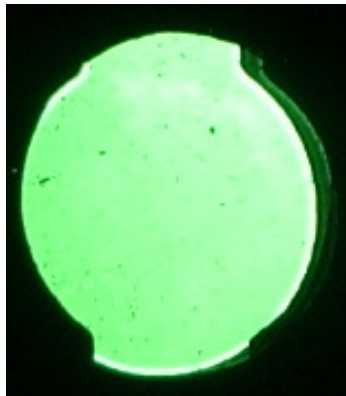
Figure 2.17: Picture of the same OLED, operated in the safe zone of characteristics.

Figures 2.15, 2.16 and 2.17 shown that the device is brighter at the contours, because the boundary effects lead to an accumulation of the current density flow lines. Therefore, if the cause of damage was the current density, and not the thermal stress, the failure should start from the boundaries of the active area and not from the middle, as instead it happens. As said previously, edges of active zone are cooled by non-active adjacent areas, so their failure is delayed. Therefore, thermal stress leads to the optical failure by the formation of non radiative, but still electrically-active, zones. The electrical damage can be observed in the I-V plot at voltages, greater than the optical failure voltage V*, producing a temperature of about 360 K. Consequently, it can be assumed that the optical failure is due to the glass transition of TPD and not all the physical properties change at the same time and at the same temperature. We can imagine that there are two different "T_g": one for optical and one for electrical parameters. In this way, the failure temperature higher than T_g measured by Xiang Zhou et al. [37] can be explained.

At the same time, the best configuration stated from Popovic et al., ITO/TPD/NPD/Alq3/Al instead of ITO/NPD/TPD/Alq3/Al [40], can be explained

considering that the TPD layer isn't located at the recombination interface and therefore it harms the device less than in the second configuration. In the ITO/TPD/NPD/Alq3/Al structure, TPD acts only as holes transporter, so its electrical failure dominates and the device can still work at temperatures higher than TPD T_g, as can be expected according to our results. In the other configuration, the TPD layer is situated on the recombination interface, so its optical failure dominates respect the electrical one.

Moreover, since the OLED temperature is an important issue in typical OLED display or lighting applications and highly thermally conductive substrates will be promising substrate candidates for such applications in terms of heat dissipation and corresponding lifetime improvement [41].

References

[1] D. M. Pai, J. Chem. Phys. **52**, 2285 (1970)

[2]. E. W. Montroll and H. Scher, J. Stat. Phys. 9, 101 (1973).

[3] H. Scher and E. W. Montroll, Phys. Rev. B 12, 2455 (1975)

[4] P. Borsenberger, L. Pautmeier and H. Bässler, J. Chem. Phys. 94, 8 (1991)

[5]. H. Bässler, Phys. Stat. Sol. (b) 175, 15 (1993)

[6] M. E. Sharfe, Phys. Rev. B 2, 5025 (1970)

[7] N.F. Mott and R.W. Gurney, "Electronic Processes in Ionic Crystals", Clarendon Press, Oxford (1940)

[8] K.C. Kao and W. Hwang. "Electrical Transport in Solids", Pergamon Press, Oxford (1981)

[9] Wolfgang Brütting, Stefan Berleb and Anton G. Mückl, Organic Electronic, Vol. 2, Issue 1, Pages 1-36 (2001)

[10] W. Brutting et al, Organic Electronics, 2, pp. 1–36, (2001)

[11] W. Brutting et al, Synthetic Metals, 122, pp.99-104, (2001)

[12] W. Brutting et al., Journal of Applied Physics, vol. 89, pp. 1704 – 1712, (2001)

[13] I. D. Parker, J. Appl. Phys. 75, 1656 (1994)

[14] R. N. Marks, D. D. C. Bradley, R. W. Jackson, P. L. Burn, and A. B. Holmes, Synth. Met. 55, 4128 (1993)

[15] Y. Gao, K. T. Park, and B. R. Hsieh, J. Appl. Phys. 73, 7894 (1993)

[16] R. H. Fowler and L. Nordheim, Proc. R. Soc. London Ser. A 119, 173 (1928)

[17] I. A. Hümmelgen, L. S. Roman, F. C. Nart, L. O. Péres, and E. L. de Sá, Appl. Phys. Lett. 68, 3194 (1996).

[18] L. S. Roman, I. A. Hümmelgen, F. C. Nart, L. O. Péres, and E. L. de Sá, J. Chem. Phys. 105, 10614 (1996).

[19] M. Koehler, I. A. Hummelgen, Appl. Phys. Lett. 70 (24), 3254-3256 (1997)

[20] L. E. Nielsen, "Mechanical properties of polymers and composites", Vol. 1 Marcel Dekker, inc. New York, 1974.

[21] P. D'Angelo, M. Barra, M. Nicodemi, and A. Cassinese, Journal Appl. Phys. 101, 044910 (2007)

[22] J. A. Quintana, P. G. Boj, J. M. Villalvilla, M. A. Díaz-García, J. Ortiz, L. Martín-Gomis, F. Fernández-Lázaro, Á. Sastre-Santos, Applied Physics Letters 92, 041101

(2008)

[23] K.A. Osipov et al, Thin Solid Films 515, 4834–4837 (2007)

[24] Shizuo Tokito, Hiromitsu Tanaka, Koji Noda, Akane Okada, and Yasunori Taga, IEEE Transaction on Electron Devices, vol. 44, No. 8, (1997)

[25] V.I. Adamovich, M.S. Weaver , R.C. Kwong, J.J. Brown, Current Applied Physics, 5, 15–18 (2005)

[26] D. H. Chung, S. W. Hur, S. K. Kim, J. U. Lee, C. H. Kim, J. W. Hong, T. W. Kim, Current Applied Physics, 4, 667–670 (2004).

[27] D. F. O'Brian, P. E. Burrows, S. R. Forrest, B. E. Koene, D. E. Loy, M. E. Thompson, Advanced Materials, 14, 1108–1112 (1998).

[28] G. Vamvounis, H. Aziz, N-X. Hub, Z. D. Popovic, Synthetic Metals, 143, 69–73 (2004).

[29] P. N. M. dos Anjos, H. Aziz, N. X. Hu, Z. D. Popovic, Organic Electronics, 3, 9–13, (2002).

[30] Shizuo Tokito, Hiromitsu Tanaka, Koji Noda, Akane Okada, and Yasunori Taga, "Temperature Dependences of Electroluminescent Characteristics in the Devices Fabricated with Novel Triphenylamine Derivatives", IEEE Transaction on Electron Devices, 44, No. 8 (1997).

[31] P. Fenter, F. Schreiber, V. Bulovid, S.R. Forrest, "Thermally induced failure mechanisms of organic light emitting device structures probed by X-ray specular reflectivity", Chemical Physics Letters 277, 521-526 (1997).

[32] Jie Xu, Biao Chen, "Prediction of glass transition temperatures of OLED materials using topological indices", J. Mol. Model 12, 24–33 (2005).

[33] Soo Young Kim Kwang Young Kim and Yoon-Heung Tak Jong-Lam Lee, "Dark spot formation mechanism in organic light emitting diodes", Applied Physics Letters 89, 132108 (2006)

[34] P. E. Burrows, V. Bulovic, S. R. Forrest, L. S. Sapochak, D. M. McCarty, and M. E. Thompson, "Reliability and degradation of organic light emitting devices", Applied Physics Letters 65, 2922-2924 (1994).

[35] D. Y. Kondakov, J. R. Sandifer, C. W. Tang, R. H. Young, "Nonradiative recombination centers and electrical aging of organic light-emitting diodes: Direct connection between accumulation of trapped charge and luminance loss", Journal Applied Physics., 93, 1108 (2003).

[36] G. Nenna, G. Flaminio, T. Fasolino, C. Minarini, R. Miscioscia, D. Palumbo, M. Pellegrino, "A Study on Thermal Degradation of. Organic LEDs Using IR Imaging", Macromol. Symp., 247, 326–332 (2007).

[37] X. Zhou, J. He, L. S. Liao, M. Lu, X. M. Ding, X. Y.Hou, X. M. Zhang, X. Q. He, S. T. Lee, "Real-Time Observation of Temperature Rise and Thermal Breakdown Processes in Organic LEDs Using an IR Imaging and Analysis System", Adv. Mater. 12, 265–269 (2000).

[38] Dong Hoe Chung, Sung Woo Hur, Sang Keol Kim, Joon Ung Lee, Chung Hyeok Kim, Jin Woong Hong, Tae Wan Kim, Current Applied Physics 4, 667–670 (2004)

[39] S. Ouro Djobo, J.C. Bernede, N. Kossi, Journal of Materials Science: Materials in Electronics 15, 579-582 (2004)

[40] Zoran D. Popovic, Hany Aziz, Nan-Xing Hu, Ah-Mee Hor, Gu Xu Synthetic Metals Vol.111–112, 229–232 (2000)

[41] Seungjun Chung, Jae-Hyun Lee, Jaewook Jeong, Jang-Joo Kim, and Yongtaek Hong Applied Physics Letters 94, 253302 (2009).

CHAPTER III

"Transient analysis: Material and device limits"

In this chapter a way to analyze the material limits performing thermo-analytical measure will be discussed and it will be evaluated how the material limits can play a rule in the OLED device electrical limits. For this understanding, AC impedance measurements versus temperature have been performed to investigate the optical and electrical failure mechanisms during the glass transition phenomena in the archetypal ITO/TPD/Alq$_3$/Al OLED structure. The related experimental data are discussed in the framework of the Universal Dielectric Response (UDR) model. By AC measurements, TPD glass transition temperature is located and temperature regions with different OLED behaviours are evidenced. The relation between the behaviours of TPD frequency response and of the OLED electro-optical response, while the temperature approaches the glass transition region, is discussed to better analyze and explain the data showed in Chapter II.

3.1 AC analysis (UDR theory)

The dielectric response of solids has been the subject of extensive investigations for the best part of a century [1-5].

A vacuum capacitor with an electric field E between its metallic plates has an interfacial charge Q_0 and if the field varies with time, the charge Q_0 follows exactly, with no inertia. If the capacitor is filled with a material medium (i.e. gasses, liquids or solids) the induced charge is increased by the polarisation P of the medium, and we will have (eq. 3.1):

$$Q = Q_0 + P = \varepsilon_0 (1 + \chi) E = \varepsilon E \qquad (3.1)$$

where ε is the dielectric permittivity and χ the susceptibility of the medium.

In dielectric measurements, the sample permittivity ε_r and ac conductivity σ are determined by measuring the capacitance C and the conductance G of a capacitor filled with the material under study by (eq. 3.2)

$$\varepsilon_r = \frac{Cd}{\varepsilon_0 S} \text{ and } \sigma = \frac{Gd}{S}$$ (3.2)

where S is the surface of the capacitor, d is the thickness of the "filling" material, and ε_0 is the vacuum permittivity.

The permittivity of a medium gives information about the relaxation response of a dielectric medium to an external electric field. For this reason, the relaxation is often described in terms of permittivity as a function of frequency, which can, for ideal systems, be described by the Debye equation [1].

In particular, the Debye relaxation is the dielectric relaxation response of ideal, non-interacting dipoles under an alternating external electric field. It is usually expressed in the complex permittivity ε of a medium as a function of the frequency field ω (eq. 3.3):

$$\varepsilon(\omega) = \varepsilon_\infty + \frac{\Delta\varepsilon}{1 + i\omega\tau}$$ (3.3)

where ε_∞ is the permittivity at the high frequency limit, $\Delta\varepsilon = \varepsilon_s - \varepsilon_\infty$ where ε_s is the static, low frequency permittivity, and τ is the characteristic relaxation time of the medium.

Or in other terms (eq. 3.4):

$$\chi(\omega) = \chi'(\omega) - i\chi''(\omega) = \frac{A}{1 + i\omega} = A\frac{1 - i\omega\tau}{1 + \omega^2\tau^2} \ .$$ (3.4)

Another model on dielectric relaxation is given by the Cole-Cole equation when the relaxation peaks are symmetric (eq. 3.5) [4]:

$$\varepsilon(\omega) = \varepsilon_\infty + \frac{\Delta\varepsilon}{1 + (i\omega\tau)^\alpha}$$ (3.5)

Most polymers show dielectric relaxation patterns that can be accurately modelled by this equation.

We can also consider the Cole-Cole approach like a special case of Havriliak-Negami relaxation that is an empirical modification of the Debye relaxation model, accounting for the asymmetry and broadness of the dielectric dispersion curve. The model was first used to describe the dielectric relaxation of some polymers, by adding two exponential parameters to the Debye equation (eq. 3.6) [6]:

$$\varepsilon(\omega) = \varepsilon_\infty + \frac{\Delta\varepsilon}{(1+(i\omega\tau)^\alpha)^\beta} \tag{3.6}$$

where the parameters α and β are related respectively with the asymmetry and broadness of corresponding spectra. So, the Cole-Cole formulation can be easily reached when the symmetry parameter (β) is equal to 1.

But generally, unlike the classical Debye model, usually amorphous systems show a dielectric response ε_r and dielectric loss characterized by a spread of dispersion on frequency and Debye's law is replaced by the UDR model [7-11].

There are two fundamentally different types of polarization response under a steady electric field, depending on the nature of the polarizing species: with dipolar species, a finite amount of charge displacement takes place and the response has loss peak of the form shown in figure 3.1.
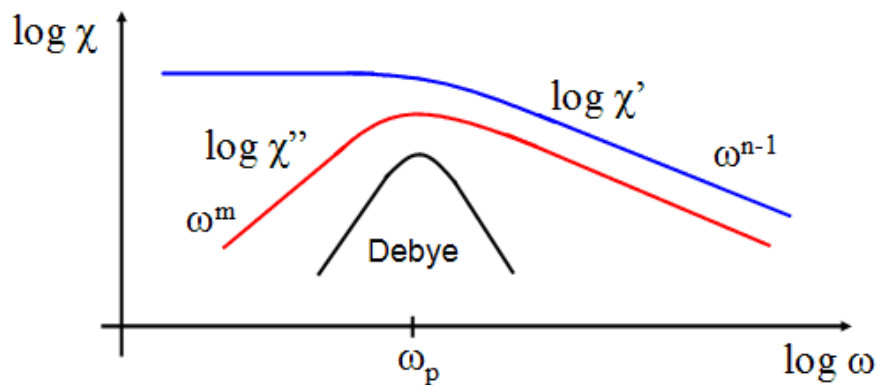
Fig. 3.1: The general shape of the dielectric response of dipolar materials showing the two slopes *m* and (*1-n*), andan example related to the ideal Debye response. Adapted from reference [10]

With hopping electronic or ionic charges an indefinite amount of charge may be displaced leading to the rising dispersion at low frequencies shown in figure 3.2.
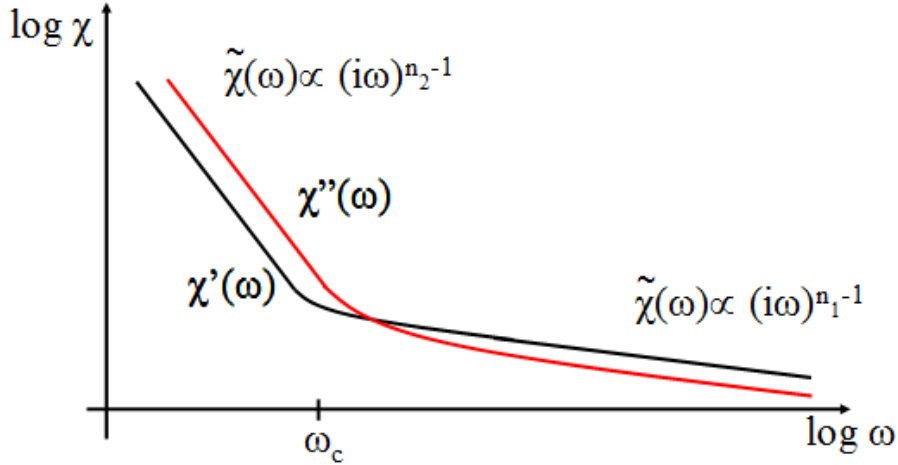
Fig. 3.2: The dielectric response of a material dominated by hopping electrons, or ions, with two power laws corresponding to low and high losses with, respectively. Adapted from reference [10]

The dipolar response is always broader than the Debye shape and generally is given by two partial power laws divided by the loss peak at ω_p. In particular, at low frequencies is possible to write (eq. 3.7):

$$\chi''(\omega) = \tan(m\pi/2)\left[\chi(0) - \chi'(\omega)\right] \propto \omega^m \tag{3.7}$$

with $0<m<1$ when $\omega<<\omega_p$

where $\chi(0)$ is the limiting constant value of $\tilde{\chi}(\omega)$ as $\omega \rightarrow 0$. Instead, at high frequencies we have the so called "universal dielectric response" (eq. 3.8):

$$\tilde{\chi}(\omega) = \left[\sin(n\pi/2) - i\cos(n\pi/2)\right](i\omega)^{n-1} \propto (i\omega)^{n-1} \tag{3.8}$$

with $0<n<1$ when $\omega>>\omega_p$

The exponents m and n cover the range 0 to 1, covering the entire range of logarithmic

slopes from zero to -1 and corresponding to dielectric losses ranging from very low to very high. The values of *m* and *n* for any particular dipolar system are independent of one another implying that they must represent two separate and independent physical mechanisms. In general, we find (eq. 3.9):

$$m \geq 1 - n \tag{3.9}$$

Hopping electronic systems such as amorphous semiconductors give the n-power law at low frequencies domain and in this specific situation it is possible to write (eq. 3.10) [7-11]:

$$\sigma(\omega) = \sigma_0 + A\omega^s \text{ and } \varepsilon_r(\omega) = \varepsilon_\infty + \left[\frac{A}{\varepsilon_0} tg\left(\frac{\pi s}{2} \right) \omega^{(s-1)} \right] \tag{3.10}$$

where A, weakly frequency dependent, is the constant phase element that shows dispersion of conductivity and dielectric properties of the filling material, σ_0 is the dc conductivity, generally separated from the ac contribution (even if this one is not related to relaxation phenomena, as happens for some materials), and ε_∞ represents, as usual, the dielectric permittivity of the compound at high frequency. The exponent s allows classifying empirically the nature of polymeric materials concerning their electrical properties as we will see in following paragraphs.

With the representation of the equations 3.10 was studied the dynamics of deep level trapping transitions [10][11] in space charge regions of p-n junctions and the hopping process [9] that are fundamental into the organic materials analysis.

3.2 Device limits and glass transition

Operational stability of Organic Light Emitting Diodes (OLEDs) is undoubtedly the most important issue to establish their potential commercial applications [12]. Among other reasons, thermal effects causing irreversible material degradation can play a crucial role in defining the device operation limits, when large current densities are produced and self-heating phenomena have to be considered [13]. In this regard, many studies have been reported showing how an OLED differently behaves during its lifetime at various working regimes and at different substrate temperatures [14][15][16][17]. Hence, several strategies have been adopted in the attempt to reduce thermal aging effects [15][16].

So far, high temperature stability studies have been mainly devoted to analyze thermally induced morphological changes in the organic materials [18][14] and to determine the critical temperatures above which the devices finally fail [15][16][17][19][20]. More in detail, it has been demonstrated that one the major thermal effects producing OLED degradation is basically related to the morphological instability of the Hole Transport Layer (HTL), as temperature approaches its glass transition [2][21][22]. Despite the considerable interest for this subject, still today, quantitative correlations between the glass transition occurrence and the device operating limits are not well established [23][24][18].

Recently, it has been shown that alternate current (AC) electrical measurements performed at different temperatures represent a reliable and not destructive tool to investigate the glass transition phenomenon in device operational situations [21][25]. These measurements are based on the application of small alternate signals (amplitude ≤ 1 V), thus preventing direct self-heating effects and related self-induced aging mechanisms. Furthermore, differently from other electrical techniques, they do not require doping procedures to increase the basic conductivity of the investigated material [21].

In this paragraph, the glass transition phenomenon and its effects on the electro-optical response of a basic OLED structure are investigated by high sensitivity AC measurements. For our purposes, a very simple and well referred OLED configuration (ITO/TPD/Alq$_3$/Al) has been considered [26][27][28]. TPD was selected for its low and well known glass transition temperature, involving morphological changes which affect the device overall behaviour without directly damaging the emitter material (Alq$_3$). The

frequency response of TPD thin films has been analyzed as a function of temperature and, consequently, modeled according to the main parameters of the so-called Universal Dielectric Response model (UDR). Characteristic temperature values are experimentally extracted and correlated to the different electro-optical operation regions of the OLED. The main target of this study is to clarify the underlying physical mechanisms related to the operation failure of OLED devices approaching the glassy region.

3.2.1 Devices transient analysis

Three basic device configurations (see figure 3.3) have been fabricated on Corning 1737 glass substrates deposited with commercial 200 nm thick Indium Tin Oxide (ITO) layer (sheet resistance Rs ≈ 10 $\Omega/\square$). Single organic layer devices (A and B) have been realized by depositing separately a 100 nm thick film of TPD and Alq_3, respectively. For the last device (C), a basic double layer OLED configuration has been adopted, with a 40 nm thick TPD film as HTL (Hole Transport Layer) and a 60 nm thick Alq_3 film as ETL (Electron Transport Layer) and as emissive layer. In any case, an Aluminium (Al) cathode has been evaporated to complete the device structure. The active area of each device is 12.56 mm^2. The devices realization follows the same procedure and parameters used in the last paragraph 2.3.1.

Al	200nm
Alq_3	60nm
TPD	40nm
ITO(Anode)	200nm
Glass (Substrate)	

Al	200nm
TPD	100nm
ITO(Anode)	200nm
Glass (Substrate)	

Al	200nm
Alq_3	100nm
ITO(Anode)	200nm
Glass (Substrate)	

Fig. 3.3. The devices considered in this work: on the left, ITO/TPD/Al device (A); in the middle, ITO/Alq$_3$/Al device (B); on the right, ITO/TPD/Alq$_3$/Al device (C).

All measurements have been performed in vacuum (P ≈ 10^{-4} mbar), mounting the sample in a cryostat with optical windows. Variable temperature experiments were carried out with a rate of about 0.5 K/min. AC measurements (amplitude AC voltage of 1 V) have

been performed by using an Agilent LCR meter (see figure 3.4). The investigated frequency and temperature ranges are [100 Hz ÷ 100 KHz] and (300 ÷ 360) K, respectively. AC experimental set-up has guaranteed a resolution for the equivalent capacitance and conductance measurements of about 0.1 pF and $1*10^{-10}$ S, respectively (figure 3.5) [21][25].
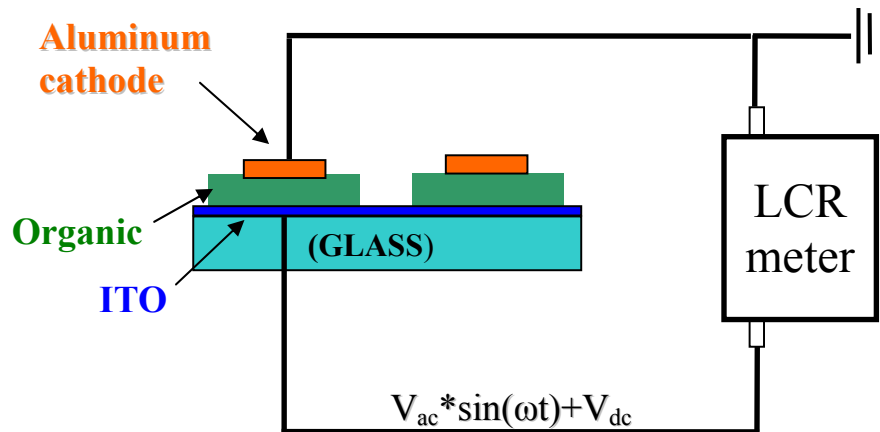
Fig. 3.4: An exemplificative electric scheme of the device under test and the AC experimental set-up
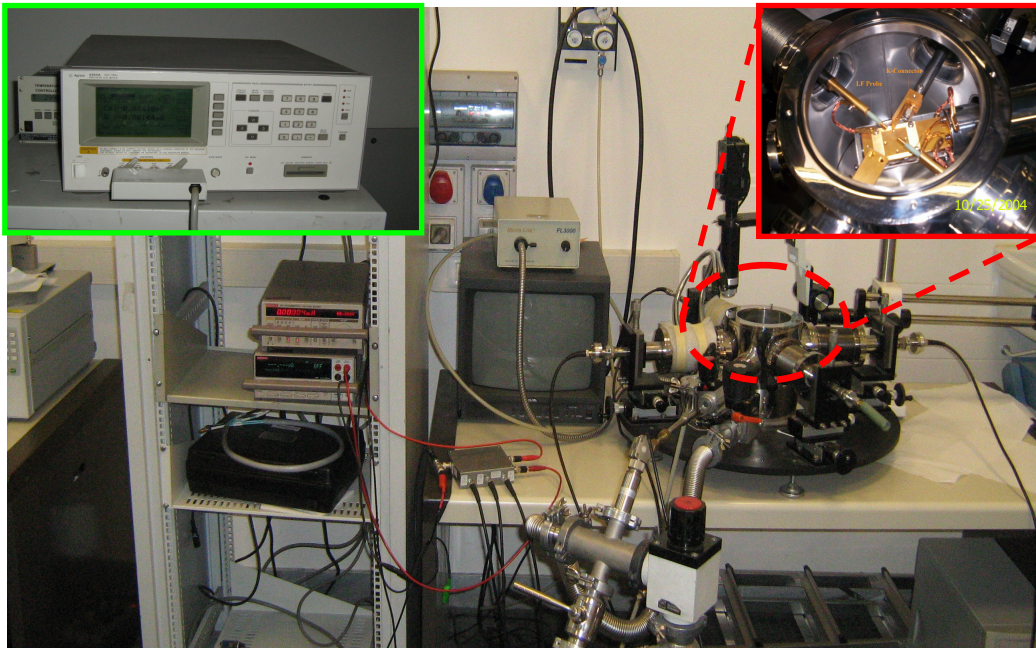
Fig. 3.5: The apparatus used during the Ac campaign measurements. Inset, on the left it is possible to see the Agilent LCR meter while on the right it is possible to see the device

holder through the optical window of the probe station.

With this kind of measures we tried to correlate the devices limits with the temperature-dependent electrical parameters. Heating the devices it is possible to appreciate a sensible change in terms of conductance and capacitance parameters, as reported in the three figures 3.6a,b,c.

In particular the conductance changed of several orders of magnitude for devices A and C when lead temperature around 340 K, instead there is no appreciable changes for device B. This can be simply explained with the reaching of the TPD glass transition temperature (Tg) that is not present in the device B. Furthermore, if we analyze with more attention the data is possible to see that the presence of the AlQ3 layer in the device C slightly mask the behaviour.

These considerations are even more valid if we plot the capacitance versus the temperature (figures 3.6a,b,c). In this case, it has to reach temperature around 350K to have an appreciable change in the capacitance related only to the device A, probably due to the TPD mechanical/structural fail.
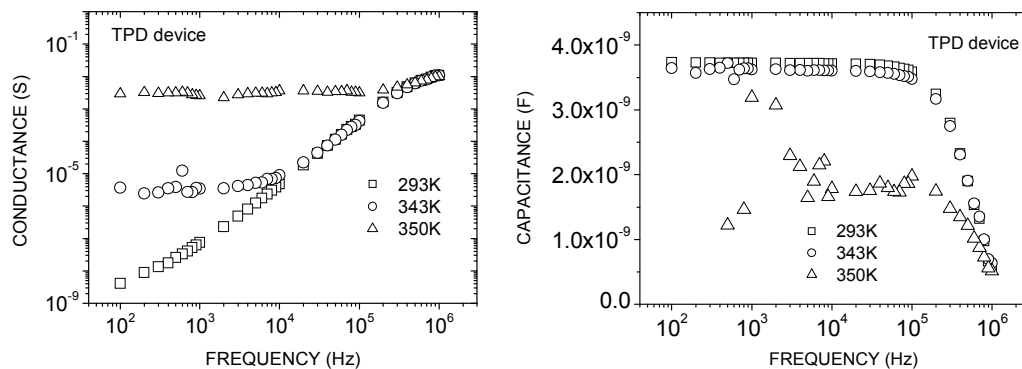
Fig. 3.6a: Conductance and capacitance measured at different temperatures for device A.
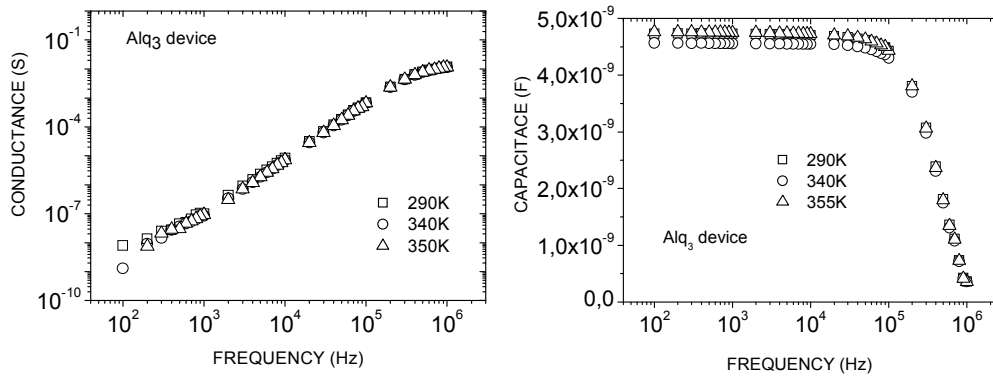
Fig. 3.6b: Conductance and capacitance measured at different temperatures for device B.
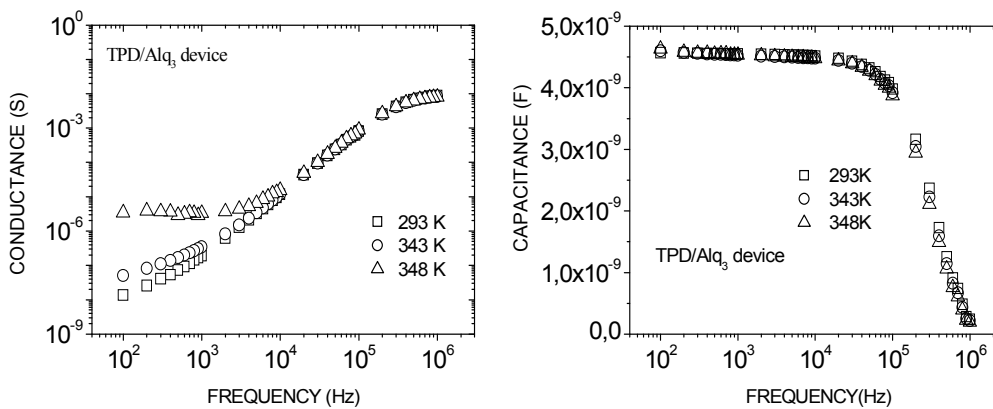
Fig. 3.6c: Conductance and capacitance measured at different temperatures device C.

3.2.2 TPD device frequency response data analysis

Our analysis has been limited to the temperature range between room temperature and 343 K, being mainly focused on the TPD glass transition effects. For TPD devices, AC measurements at higher temperatures (up to 360 K) have shown the occurrence of electrical instabilities sample dependent, see also figure 2.11, with large and irreversible low frequency conductivity switching. A detailed discussion of these effects, generally attributed to extrinsic phenomena related to the device mechanical/structural fail, is out of the scope of this work.

Figure 3.7 reports a comparison of the real part (ReZ) of the measured impedances for three typical devices A, B and C for a temperature variation from 297 K to 343 K. For

device A (single TPD layer), two orders of magnitude change can be appreciated for ReZ by increasing the temperature, while, in comparison, a very small evolution can be noted for the Alq_3 device (B) in the same range. Obviously, this different temperature sensitivity is due to the TPD glass transition occurrence, being Alq_3 Tg located at much higher temperatures [29]. In similar way, the presence of Alq_3 in device C seems to mask the TPD temperature behaviour, reducing the corresponding ReZ increase.
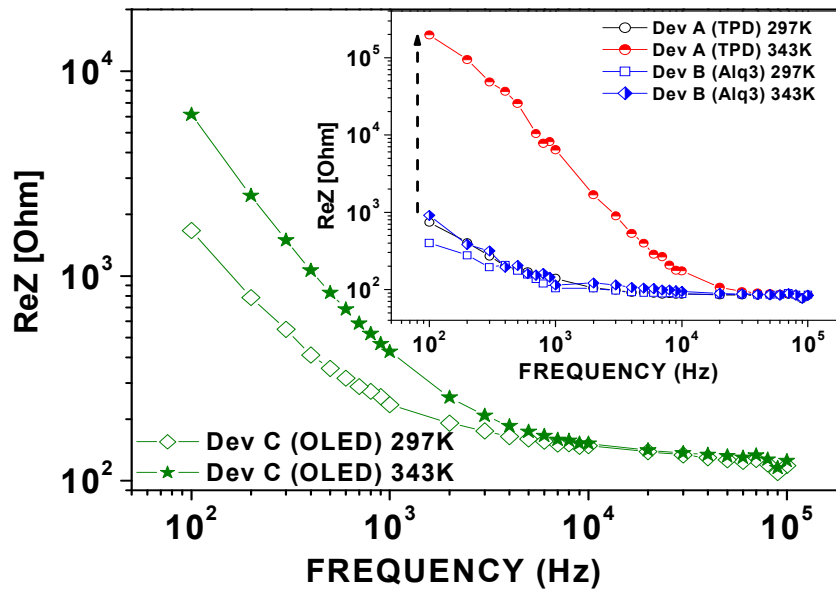
Fig. 3.7: Real part of the impedance (ReZ) for device C and (inset) for devices A and B, measured at 297 K and 343 K.

Provided those results, in the following, our attention is focused on the analysis of the device A (ITO/TPD/Al) frequency response and on its temperature dependence. To this regard, the corresponding variable temperature real and imaginary parts of the impedance are reported in figure 3.8.
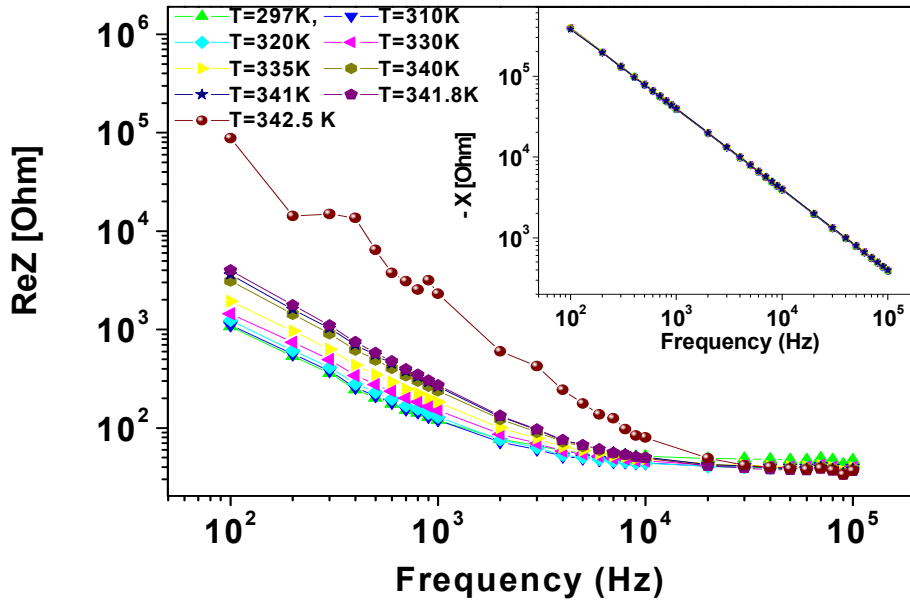
Fig. 3.8: Real part of impedance (ReZ) measured at different temperatures for device A. In the inset, It is shown the corresponding imaginary part (–X).

This figure makes clear that variation of ReZ along temperature becomes actually significant above 330 K, while no appreciable change can be detected from the imaginary part (-X) data, showing an almost constant slope as a function of frequency. By this last occurrence, it is possible to conclude that a simple circuit with a single RC parallel loop and a series resistance Rs (30 Ω ÷ 40 Ω), modelling the ReZ high frequency (f > 20 kHz) plateau, is suitable to describe the device A frequency response in all the investigated temperature range [30].

Furthermore, the Rs slight lowering at increasing temperatures reveals that it can be mainly due to the ITO anode contact. In order to focus the attention only on the temperature dependence of TPD intrinsic electrical properties, the Rs contribution has been subtracted from frequency data and a conductance/capacitance parallel mode representation has been adopted, directly accounting for TPD conductivity and dielectric permittivity (figure 3.9 and 3.10). Anyway, hereafter, the data analysis will be referred to the frequency range between 100 Hz and 10 kHz, where any residual contact resistance contribution can be excluded.
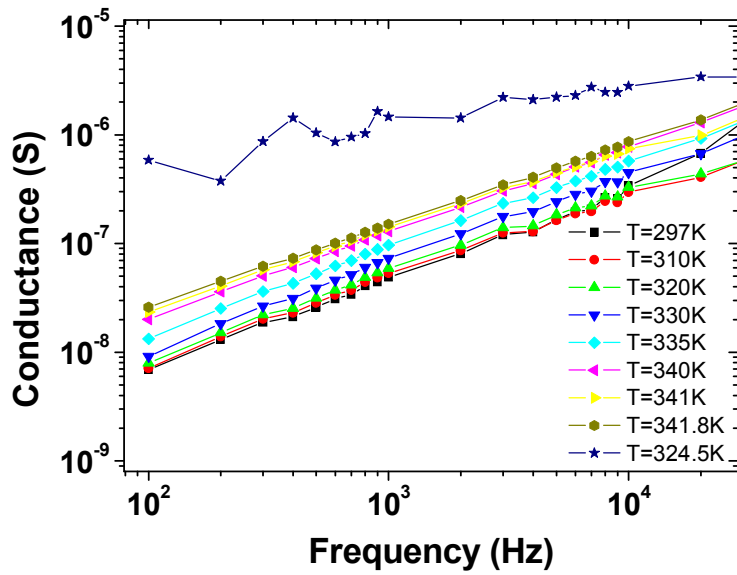
Fig. 3.9: Conductance as a function of frequency, measured at different temperatures.
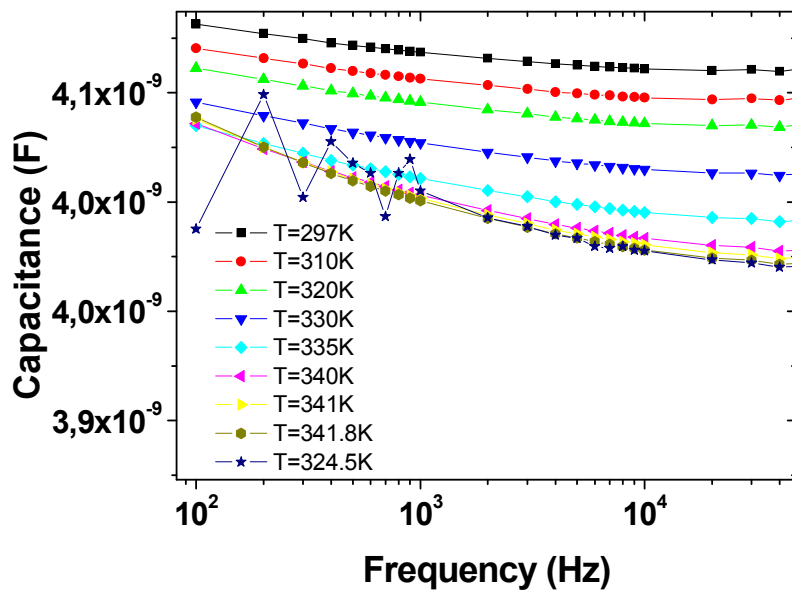
Fig. 3.10: Capacitance as a function of frequency, measured at different temperatures.

As shown, conductance (G) and capacitance (C) follow a complementary behaviour: the former increases with temperature while the latter decreases.

Moreover, the conductance variation rate gets more pronounced approaching the upper temperature limit (343 K), while the capacitance behaviour seems much more complex and depending on frequency.

It should also be noted that low frequency experimental data appear noticeably scattered close to 343 K for both capacitance and conductance. Anyway, no irreversible effect is detected below this value.

The frequency dependence of conductance in the log-log plot suggests that experimental data can be well described by the UDR model [31][32], which for G predicts the expression (see also eq. 3.10):

$$G(\omega) = G_0 + A_G * \omega^s \qquad\qquad (3.11).$$

Here, A_G is the constant phase element that shows dispersion of conductivity and dielectric properties of the filling material [33], while G_0 is basically related to the conductivity in the limit $\omega \rightarrow 0$. Usually, the exponent s allows classifying empirically the electrical nature of the investigated disordered materials: s was experimentally demonstrated to be close to 0.8 [34] or to 1 [10] for amorphous semiconductors and insulators, respectively.

By using equation 3.11, temperature dependence of the s parameter has been extracted from conductance data in figure 3.9 and it is reported in figure 3.11. As shown, s results to be close to 0.8 and displays weak temperature dependence, with a more pronounced reduction only near 340 K and a final drop in the 343 K proximity. In general, s decreasing behaviour at increasing temperature is expected in organic compounds, where basic hopping mechanisms rule the conduction processes [35]. Here, we want also to stress that Rs subtraction from impedance data is essential for the correct evaluation of s which, otherwise, could be estimated even greater than 1.
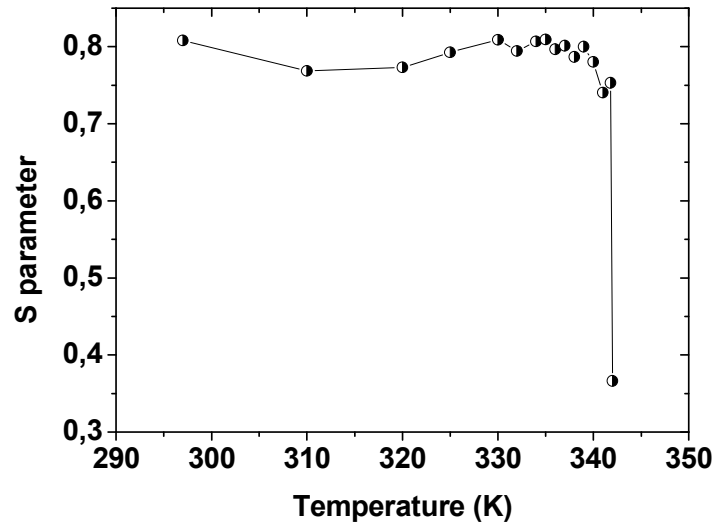
Fig. 3.11: UDR *s* parameter as a function of temperature.

In order to relate more directly the AC measurements on TPD-only devices with the OLED temperature behaviour, capacitance and conductance data have been plotted as a function of temperature for frequencies in the range between 100 Hz and 1 kHz (figure 3.12 and 3.13). This representation helps to clearly identify characteristic temperature regions, resembling those evidenced in the OLED response analysis.
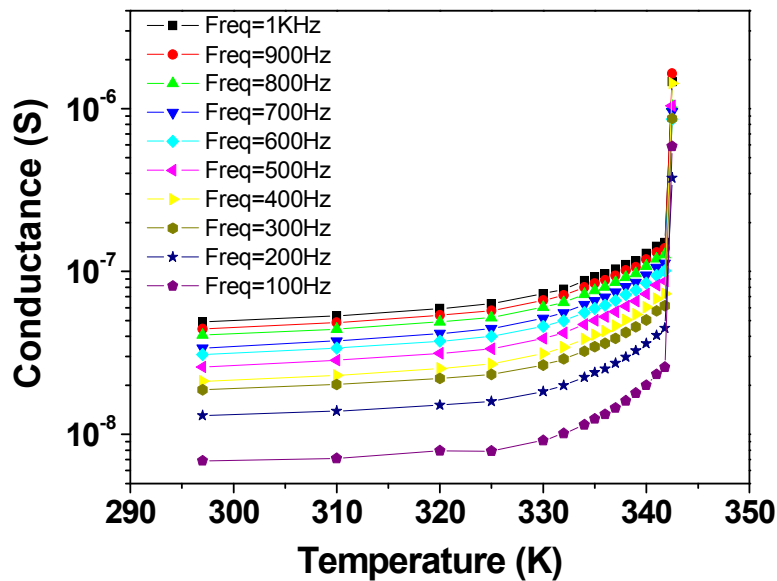
Fig. 3.12: Temperature-dependent conductance for the device A at different working frequencies.
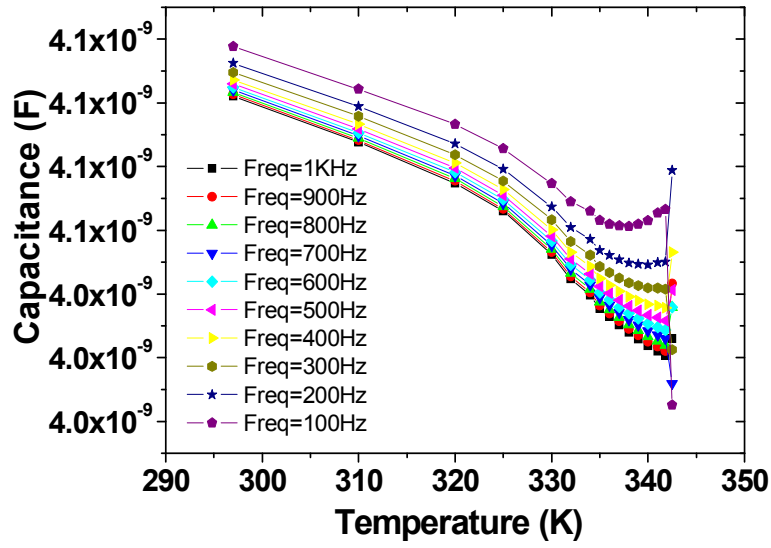
Fig. 3.13: Temperature-dependent capacitance for the device A at different working frequencies.

At each frequency, approaching 343 K, conductance increases with temperature, according to a law given by the superimposition of more than exponential behaviours. On the contrary, capacitance linearly decreases from room temperature up to about 320 K, independently on frequency. In this temperature range, in a first approximation, the capacitance reduction can be completely ascribed to the TPD thermal expansion that allows an estimation of the related coefficient by the expressions (eq. 3.12):

$$\Delta C = \varepsilon_0 \varepsilon_r \frac{A}{\Delta d} \qquad \text{and} \qquad \frac{\Delta d}{d_0} = \alpha * \Delta T \qquad (3.12)$$

where d_0 is the starting TPD thickness. By this simple approach, α has been estimated to be about $2.57*10^{-4}$ K^{-1} which is similar to the value evaluated by x-ray reflectivity measurements [29].

Above 320 K, capacitance behaviour becomes much more frequency dependent and is no longer monotonically decreasing. In particular, at the lowest frequencies (100 Hz, 200 Hz), C reveals the occurrence of a minimum between 335 K and 338 K, where Tg is located. Furthermore, it is possible to observe that at higher frequencies the capacitance minimum tends to shift to higher temperatures, in agreement with Tg frequency dependence [21]. Hence, by these observations, it seems that the incoming molecular

rearrangement towards to the new quasi-glassy state and the related variation in the material viscosity find a direct manifestation in the temperature-dependent dielectric relaxation. A more concise representation of C and G data is proposed in figure 3.14, where the ratio between C and G is reported as a function of temperature at different frequencies.
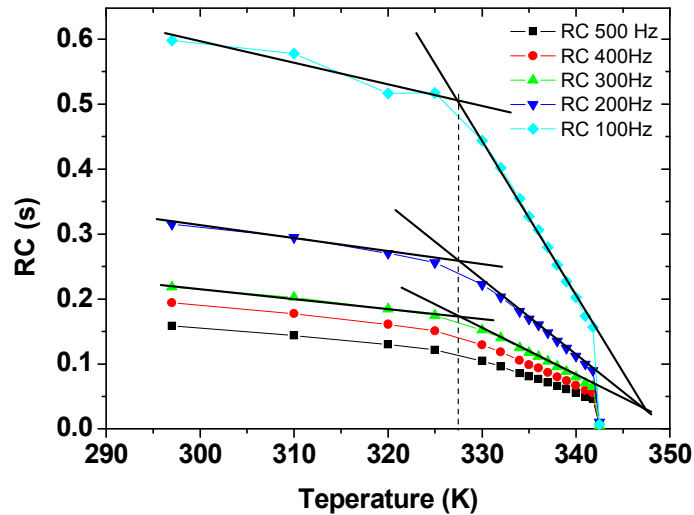
Fig. 3.14: RC data versus temperature at different working frequencies.

The resultant RC dispersive behaviour, with its significant frequency dependence, is another direct consequence of the UDR model. By these data, temperatures around 328-329 K still appear as a separation point between two different working regimes. Anyway, in both the two ranges, RC data display linear temperature dependences with two different slopes. These experimental findings relate definitively the OLED electro-optical response in the temperature range between 328K and 340K to the TPD behaviour and to the occurrence of the glass transition. In more detail, we infer that the slope changes in the OLED electroluminescence and current occurring at 328-329 K can be related to glass transition effects mainly involving the interface regions between HTL and ETL, and HTL and the anode (see also figures 2.6 and 2.11).

Although our measurements account for a glass transition occurrence in the bulk material located between 335 K and 338 K, Tg interface localized effects at lower temperatures can not be excluded [36], pointing out for more care in the definition of device operational limits. Further experiments considering OLED with different HTL layer thickness are envisaged. In any case, OLED behaviour above 340K is strongly affected

by the TPD glassy state which introduces remarkable current perturbation and makes more critical the role of ETL layer.

In conclusion, the AC electrical response of thin TPD films approaching the glass transition region has been investigated. The results analysis shows that the glass transition occurrence has a strong impact on the electro-optical behaviour of an OLED based on TPD Hole Transport Layer, defining different working regimes. In particular, glass transition kinetics seems to involve a temperature range of about 10 K below the nominal glass transition temperature. Interface effects have to be considered to this concern. AC impedance spectroscopy coupled with thermal stress has confirmed to be a useful technique to study the processes governing the dynamics of glass transition and a tool to evidence the device operational limitations.

References

[1] P. Debye, Physik. Zeit., 13, 97 (1912).

[2] J. H. Van Vleck, "On Dielectric Constants and Magnetic Susceptibilities in the new Quantum Mechanics Part I. A General Proof of the Langevin-Debye Formula", Phys. Rev. 29, 727 - 744 (1927)

[3] Lars Onsager "Electric Moments of Molecules in Liquids" J. Am. Chem. Soc., 58 (8), pp 1486–1493 (1936)

[4] H. S. Cole and R. H. Cole "Dispersion and Absorption in dielectrics", Journal of Chemical Physics, vol. 9, 341 (1941)

[5] K. L. Ngai, A. K. Jonscher, C. T. White, "On the origin of the universal dielectric response in condensed matter", Nature, vol. 277,185 (1979)

[6] S. Havriliak, and S. Negami, "A complex plane representation of dielectric and mechanical relaxation processes in some polymers", Polymer, vol. 8 (4), 161 (1967)

[7] A. K. Jonscher, "The Universal Dielectric Response", Nature vol.267, 673 (1977)

[8] L. A. Dissado and R. M. Hill, "The fractal nature of cluster model dielectric response function", Journal Applied Physics, vol. 66 (6), 2511 (1989)

[9] A. K. Jonscher, "Dielectric characterization of semiconductors", Solid-State Electronics, vol. 33, No. 6, 737-742 (1990)

[10] A. K. Jonscher, "The Universal Dielectric Response and its physical significance", IEEE Transactrion on Electrical Insulation, vol. 27, No. 3, 407 (1992)

[11] A. K. Jonscher, "Dynamics of deep level trapping in space charge region", Solid-State Electronics, vol. 33, No. 1, 139-142 (1990)

[12] Cok, Ronald S. Leon, Felipe A., "Temperature measurement using an OLED device", US Patent 7158106, application No. 11034032, filed on 01/12/2005.

[13] D. Y. Kondakov, J. R. Sandifer, C. W. Tang, R. H. Young, "Nonradiative recombination centers and electrical aging of organic light-emitting diodes: Direct connection between accumulation of trapped charge and luminance loss", Journal Applied Physics., 93, 1108 (2003).

[14] D. H. Chung, S. W. Hur, S. K. Kim, J. U. Lee, C. H. Kim, J. W. Hong, T. W. Kim, "Temperature-dependent electrical properties of organic light-emitting diodes depending on cathodes", Current Applied Physics, 4, 667–670 (2004).

[15] D. F. O'Brian, P. E. Burrows, S. R. Forrest, B. E. Koene, D. E. Loy, M. E. Thompson, "Hole Transporting Materials with High Glass Transition Temperatures for Use in Organic Light-Emitting Devices", Advanced Materials, 14, 1108–1112 (1998).

[16] G. Vamvounis, H. Aziz, N-X. Hub, Z. D. Popovic, "Temperature dependence of operational stability of organic light emitting diodes based on mixed emitter layers", Synthetic Metals, 143, 69–73 (2004).

[17] P. N. M. dos Anjos, H. Aziz, N. X. Hu, Z. D. Popovic, "Temperature dependence of electroluminescence degradation in organic light emitting devices without and with a copper phthalocyanine buffer layer", Organic Electronics 3, 9–13 (2002).

[18] V.I. Adamovich, M.S. Weaver, R.C. Kwong, J.J. Brown, "High temperature operation and stability of phosphorescent OLEDs", Current Applied Physics, 5, 15–18 (2005).

[19] G. Nenna, G. Flaminio, T. Fasolino, C. Minarini, R. Miscioscia, D. Palumbo, M. Pellegrino, "A Study on Thermal Degradation of. Organic LEDs Using IR Imaging", Macromol. Symp., 247, 326–332 (2007).

[20] X. Zhou, J. He, L. S. Liao, M. Lu, X. M. Ding, X. Y.Hou, X. M. Zhang, X. Q. He, S. T. Lee, "Real-Time Observation of Temperature Rise and Thermal Breakdown Processes in Organic LEDs Using an IR Imaging and Analysis System", Adv. Mater. 12, 265–269 (2000).

[21] P. D'Angelo, M. Barra, M. Nicodemi, and A. Cassinese, "Phase transitions and aging phenomena in dielectriclike polymeric materials investigated by ac measurements", Journal Applied Physics 101, 044910 (2007).

[22] J. A. Quintana, P. G. Boj, J. M. Villalvilla, M. A. Díaz-García, J. Ortiz, L. Martín-Gomis, F. Fernández-Lázaro, Á. Sastre-Santos, "Determination of the glass transition temperature of photorefractive polymer composites from photoconductivity measurements", Applied Physics Letters 92, 041101 (2008).

[23] K.A. Osipov et al., "Influence of thermal annealing on photoluminescence and structural properties of N,N′-diphenyl-N,N′-bis(1-naphthylphenyl)-1, 1′-biphenyl-4,4′-diamine (α-NPD) organic thin films", Thin Solid Films 515, 4834–4837 (2007).

[24] Shizuo Tokito, Hiromitsu Tanaka, Koji Noda, Akane Okada, and Yasunori Taga, "Temperature Dependences of Electroluminescent Characteristics in the Devices Fabricated with Novel Triphenylamine Derivatives", IEEE Transaction on Electron Devices, 44, n. 8, (1997).

[25] A. Castaldo, L. Quercia, G. Di Francia, A. Cassinese, and P. D'Angelo, "AC electrical investigation of polysilsesquioxanic films used as humidity sensors", Journal Applied Physics 103, 054511 (2008).

[26] G. E. Jabbour, B. Kippelen, N. R. Armstrong and N. Peyghambarian, "Aluminum based cathode structure for enhanced electron injection in electroluminescent organic devices", Applied Physics Letters 73, 9 31 (1998).

[27] Haichuan Mu, Hui Shen, David Klotzkin, "Dependence of film morphology on deposition rate in ITO/TPD/Alq3/Al organic luminescent diodes", Solid-State Electronics 48, 2085–2088 (2004).

[28] Junqing Zhao Shijie Xie, Shenghao Han, Zhiwei Yang, Lina Ye, and Tianlin Yang, "A Bilayer Organic Light-Emitting Diode Using Flexible ITO Anode", Phys. Stat. Sol. (a) 184, No. 1, 233–238 (2001).

[29] P. Fenter, F. Schreiber, V. Bulovid, S.R. Forrest, "Thermally induced failure mechanisms of organic light emitting device structures probed by X-ray specular reflectivity", Chemical Physics Letters 277, 521-526 (1997).

[30] M. Barra, P. D'Angelo, A. Cassinese, L.E. Hueso, P. Graziosi, V. Dediu "Manganite/Alq3 interfaces investigated by imedance Spectroscopy technique" Organic Electronics 9, 911-915 (2008)

[31] A. K. Jonscher, "The Universal Dielectric Response: Part I", IEEE Electr. Insul. Mag. 6, 2, 16- (1990).

[32] M. Barra, M. Biasiucci, A.Cassinese, P. D'Angelo, A. C. Barone, A. Carella, A. Roviello, "Direct current and alternating current electrical transport properties of regioregular poly[3-(4-alkoxyphenyl)-thiophenes]" J. Appl. Phys. 102, 093712 (2007).

[33] Z. G., Zhang D. P. Chu, and M. McGregor, "Frequency dependence of the dielectric properties of La-doped Pb(Zr0.35Ti0.65)O3 thin films", Applied Physics Letters 83, 2892 (2003).

[34] M. Pollak and T. H. Geballe, "Low-Frequency Conductivity Due to Hopping Process in Silicon", Phys. Rev. 122, 1742 (1961).

[35] S. R. Elliott, "A.C. conduction in amorphous chalcogenide and pnictide semiconductors", Advances in Physics 36, 135 (1987).

[36] C. Kim, A. Facchetti. T. J. Marks, Polymer Gate Surface Viscoelastacity Modulates Pentacene Transistor Performance, SCIENCE 318, 76-80 (2007).

The performance of OLED devices, and in particular their efficiency, are linked to many peripheral factors, which are all to be taken into account to develop a really good optimization strategy.

This chapter is addressed on the issue of optical losses, conditioned by the different refractive indices of the materials used, which is crucial to improve the performance of devices and to interpret in better way their overall behaviour. We will try to decouple the problems due to optical aspects from those due to electrical issues, which otherwise may be difficult to interpret.

In particular, it might happen that a device with high internal efficiency may be considered not good only because of a bad coupling between the used materials, and therefore, it would be in a wrong way putted aside.

In the following paragraphs we will analyze the causes of losses around the device, an experimental method is explained to quantify the losses and it will identify some possible strategies for the improvement of optical paths and finally the external efficiency.

4.1 Out-coupling: origin of the problem

As we already mentioned in the first chapter, to give an understanding about the basic operation principles of an organic LED we have to consider all the mechanisms that lead to an external loss in efficiency.

The external efficiency (eq. 1.1 and 1.6) can be represented by the product of several loss factors that analyze all the physical mechanisms that deny the creation and emission of photons and their optical path.

The first loss factor is due to the charges that cannot recombine to create the exciton, this is due by the not perfect balance between positive and negative charges injected inside the device. At this point, however, not all the created excitons will decay in a radiative

way, due to various intrinsic dissipative phenomena related to temperature, pressure, humidity and chemical process (i.e. quenching). Finally, a substantial part of the generated photons will be unable to escape from substrate due to an imperfect optical coupling [1][2].

The last loss factor is determined from the presence of several different optical materials constituting the device, and so depends strongly on the geometry and materials used.

The optimization strategy can be summarized essentially in two types, namely optoelectronic type, linked to the generation of photons, and optical, linked to the propagation of photons.

The optoelectronic optimization is used to optimize the balance of electrical charges, to increase the percentage of excitons created by recombination of these charges and therefore to optimize the generation of photons. The optical optimization, it is instead used to improve the path of light generated by the device and can be developed due to the change in geometric parameters or the refractive index of the layers constituting the device. The latter approach may be partly in opposition with the first one, because changes the refractive index of a material means also changes the electrical behavior and thus generally it is necessary to find a good compromise (figure 4.1).
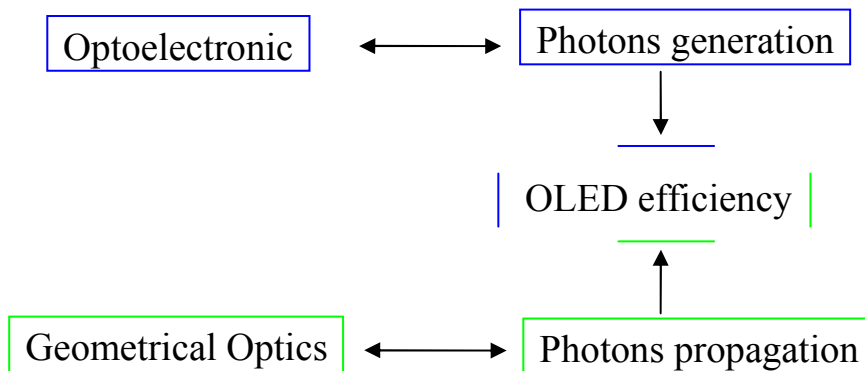
Fig.4.1: Block diagram of the optimization strategies related to the photon generation and propagation in an OLED device

Now, if we analyze the optical path of photons for a typical OLED device, it can be seen immediately that there are many materials used during its realization process and consequently many refractive indices to be considered for an appropriate analysis of the problem.

From figure 4.2 we can see that the light paths that do not allow the escape of photons through the substrate are mainly due by two interfaces, one between the TCO (Transparent Conductive Oxide), ITO at this moment, and the glass substrate and the second between the glass substrate and the air. Thus in both cases it is due by the presence of big jumps in the refractive index.

The light trapped within the device will be waveguided, either eventually becoming absorbed or emitted from the edge of the substrate.
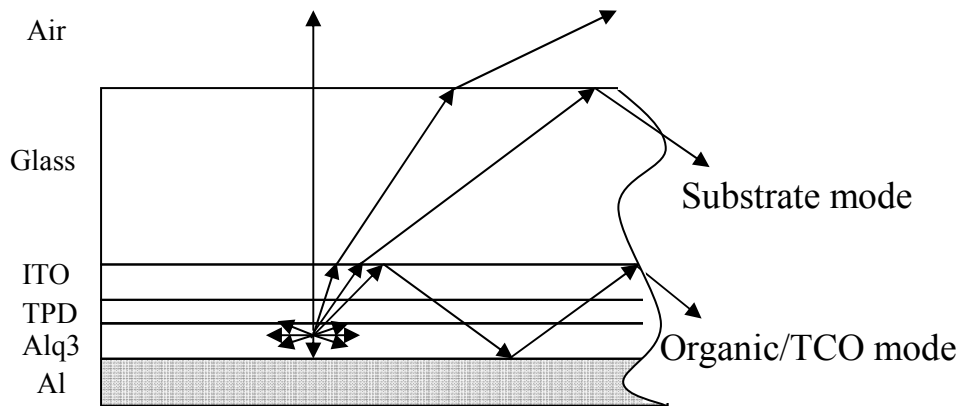
Fig. 4.2: Schematic picture of the possible light paths through an OLED device. It is possible to note the two possible loss modes.

The large mismatch between the refractive index of the polymer and air results in a large proportion of the light rays undergoing total internal reflection as light tries to pass from a high to a low refractive index material.

Some of the light generated inside the device, thus becomes trapped, unable to escape into the air, an effect that involve both inorganic and organic LED structures (figure 4.3).
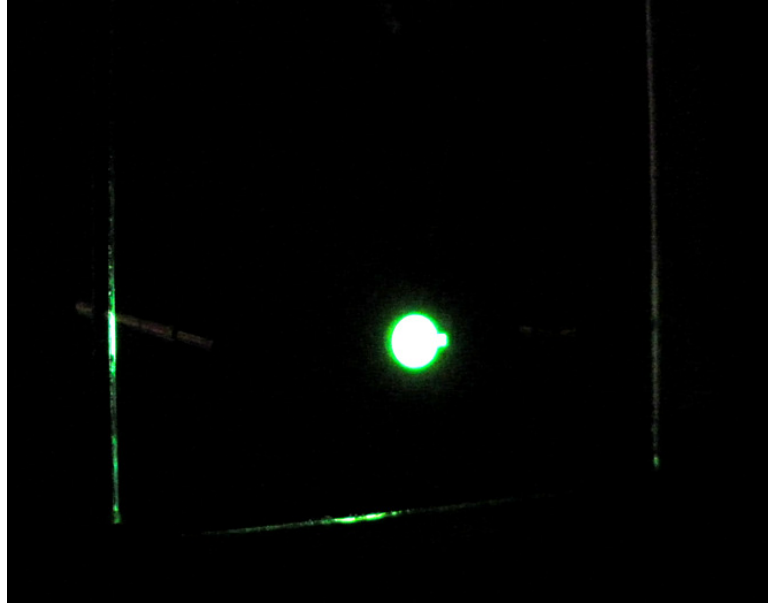
Fig. 4.3: An OLED picture where is possible to note the light trapped that escape at the border of the substrate.

All the mentioned argumentations can be easily summarized by one of the most important law in the geometrical optics, the Snell law.

Another important feature is related between the optical coupling device and the distribution of excitons within the emissive material. Therefore, the electron-hole pair, a dipole, depending on whether the material is a polymer or small molecules, respectively, there will be an emission following an in-plan or an isotropic behavior.

Returning to the formulas 1.1 and 1.6, they can be rewritten in more succinct way (eq. 4.1):

$$\Phi_{el} = \Phi_{int}\eta_e \tag{4.1}$$

A simple expression can be derived for the maximum emission efficiency based on ray optics and Snell's law for refraction. This assumes that one side has a perfect reflector and the emission is isotropic not subjected to optical interference with the reflector, in this case the output coupling efficiency is given by the often-cited relationship (eq. 4.2),

$$\eta_e = 1 - \left(1 - \frac{1}{n^2}\right)^{\frac{1}{2}} \tag{4.2}$$

that for large n become $\eta_e \sim 0.5/n^2$ [3].

For emission from inplane dipoles, not subjected to optical interference with the reflector, the proportion of light travelling perpendicular to the surface is increased and thus more of the light is emitted at angles less than the critical angle, the expression for the light out coupling now approximates to the following (eq. 4.3):

$$\eta_e = 1 - \frac{3}{4}\left[\left(1 - \frac{1}{n^2}\right)^{\frac{1}{2}} + \frac{1}{3}\left(1 - \frac{1}{n^2}\right)^{\frac{3}{2}}\right]$$

(4.3)

that for large n become $\eta_e \sim 0.75/n^2$

Moreover, for isotropic dipoles the presence of optical interference with the cathode bring to $\eta_e \sim 0.75/n^2 \pm 0.1$ and $\eta_e \sim 1.2/n^2$ for in-plane dipoles.

In small molecule-based OLEDs there is no preferential arrangement of the dipoles and the emission is thus expected to be isotropic. However, in polymer based OLEDs the polymer chains are found to be aligned preferentially inplane [3] [4] [5] which leads to increased output coupling.

So, if now we use a small molecules material as can be the Alq_3 (tris (8-Hydroxyquinoline) Aluminum) molecule with refractive index $n = 1.72$ we will find that η_e factor goes from 0:29 to 0:25 [6].

This gives us enough elements to understand the magnitude of the problem and how is important to optimize the out-coupling aspect for the efficiency of OLED devices.

We have seen how is important to know the correct refractive index of organic compounds present into the device under test to reconstruct the right optical path of the photons. The solution that enable a better optical path for light pass also through the choice of an emissive material with a low refractive, or for example using a "host" material with the appropriate refractive index [7].

Great importance in the study of materials for optical coupling is covered in a study of the properties of the substrates on which are realized the devices, to adjust the optimization strategy with their characteristics. If we analyze the table 4.1, which summarizes the characteristics of the used polymer substrates, we find that the optical properties change drastically case by case.

Table 4.1: Optical and morphological properties for several plastic substrates

Polymer	PET	PEN	PC	PES	PCO	PI	PAR
Trasmission (%)	> 85	>80	>90	90	91.6	70	90
Refractive Index	1.66	1.75	1.59	1.60	1.60	1.66	1.51
RMS surface roughness (nm)	5.2	2.0	3.6	3.0	1.8	1.6	1.8
Surface energy (mJ/m2)	43.3	43.8	46.1	41.2	40.7	40.2	43.0

For this reason, even if you find a solution that is appropriate for one type of substrate it don't necessarily remain appropriate for the others and so you must adjust it from time to time.

4.2 State of the art

Brightness and efficiency are extremely important factors for the employment of organic light emitting diodes (OLEDs) in lighting and displays application in the competition against more standard technologies. For this reason, extracting the wave-guided light trapped within OLED and more in general within electroluminescent flat multilayer device structure is one of the main driving forces to improve the device efficiency.

There are many strategies that have been used over the years to improve the optical coupling in OLED devices and there is not only one answer to this problem. The choice of the strategy must necessarily be linked with the technology you have, to take advantage about the knowledge accumulated in the past on the used materials. Then, chosen the strategy it is necessary to find the right solutions to optimize the process and geometry.

The examples that can be found in the literature exploit many different technologies and can be grouped into two categories: one related to the change in refractive index, as mentioned in the first paragraph, between the TCO and the substrate and another related to the index variation between substrate and air.

One of the simplest methods is represented by 'increasing the substrate-air interface roughness (figure 4.4). This technique helps the escape of light trapped in the substrate that is scattered at different angles and therefore has more chance of escape reaching also 30% of efficiency improvement [8] [9].
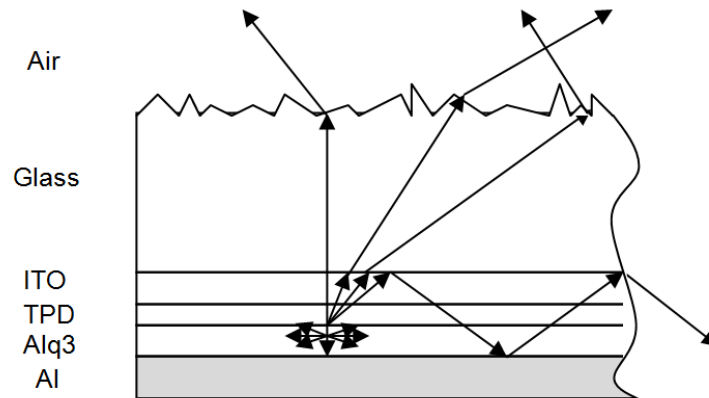
Fig.4.4: A texturing example and its effects on the external efficiency.

This kind of effect can be emphasized using silica spheres [10] or an additional layer in which are dispersed particles which increase the possibility of scattering for the photons and thus their escape from the substrate [11].
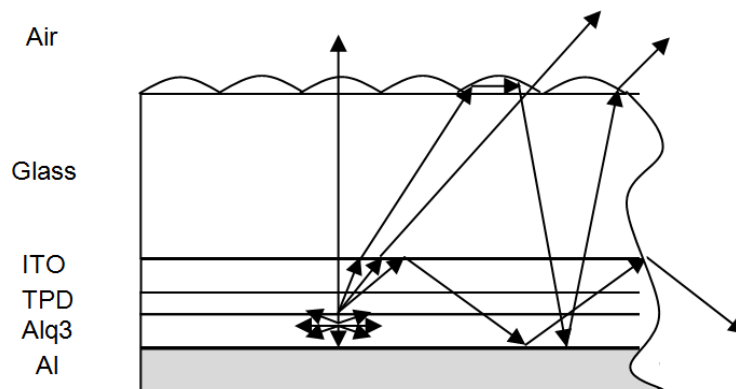
Fig. 4.5: Simplified example of "ray-trace" in the presence of microlens at the interface substrate-air.

Another method to optimize the optical efficiency is made by the change in shape at the interface substrate-air using a pattern of microlenses [12] [13] [14]. This application has guaranteed very good performance, but the photon emission profile has also noted to be changed by the geometry of the applied lenses (figure 4.5).

Also regarding the jump in the refractive index at TCO-substrate interface can be found in the literature many suggestions and directions. Technological solutions require the

introduction of an additional layer between the TCO and the substrate. Introducing a layer with higher refractive index respect to TCO one and a special "patterning" that can drive the light with a different and more efficient way [15].

It has also demonstrated that embedding a low-index grid in the organic layers can enhance the out-coupling of the waveguided light without spectral distortion [16].

A further application makes use of wrinkling the emissive area, as shown in figure 4.6, with which we can obtain even a doubling in the performance due to the presence of a Bragg scattering [17]. A final technique much more complex in technology terms makes use of a two-dimensional nanopattern to create a photonic crystal which improves substantially the outcoupled light as already shown with inorganic LEDs [18].

In the last two mentioned techniques there is a change not only the profile but also the emission spectrum depending on the used geometry, which must be taken into account in applications that must be used in established framework.
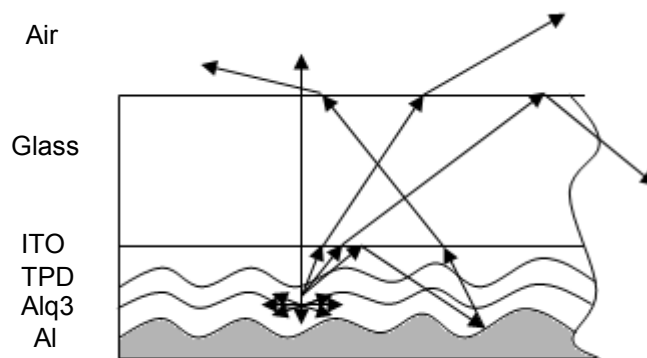
Fig. 4.6: An example of crumpling the emissive area to have an enhanced efficiency.

4.3 Microlenses

As discussed in the previous paragraph, the change in the geometry of the substrate appears to be crucial for improving the optical coupling at the substrate-air interface and for this reason we have started to develop simulations that give us indications about the geometric parameters to be used by comparing them with data produced during the experiments and reported in the literature [19] [20].

A first approach was to analyze the geometry of the microlenses in order to have the right constraints to achieve our purpose for this particular type of structure, without making too many and expensive tests.

After the data analysis it will be shown the characterization of a PDMS microlens structure realized by gravure printing technique.

4.3.1 Simulations

The pattern tested for the simulations is given by microlenses of about 100μm diameter alternating with a pitch of 200μm, as shown in figure 4.7, on a square area 3mm*3mm on the surface of a substrate with a refractive index of 1.57. The OLED active area is equal to a circle with a diameter of 3mm (figure 4.10) that fall into the center of the square created by the microlenses.
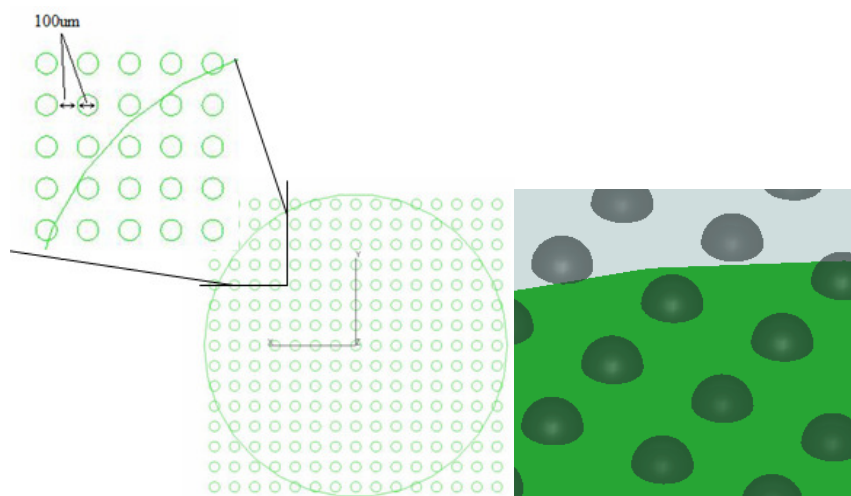
Fig. 4.7: Model of patterning used in the simulations carried out by an optical CAD

(computer-aided design) (left) and 3D profile of the same patterning (right).

The other parameters used during the simulations are shown in table 4.2, where we can note that the thicknesses of organic layers have dimensions much higher than the conventional ones, only because a software limit on thickness parameter. This does not affect the type of analysis that we actually want to be qualitative.

Table 4.2: Material parameters used during the simulations

Material	Refractive index	Thichness (m)
Alq_3	1.742	1e-7
TPD	1.787	1e-7
ITO	1.827	1e-7
Glass	1.575	1e-3

The simulation, thus, begins with the departure of the rays at the interface between Alq_3 and TPD with a spherical emission profile, and then the rays, after passing through several device layers, are captured by an absorbing wall placed at 1 mm from the surface of substrate figure 4.8.

In this way you could make a comparison between the various structures considered analyzing the variation of the average light power absorbed by the wall. In figure 4.9 we can observe the distribution of incident rays and the values of the simulation performed without the presence of microlens, this simulation therefore become a sort of base line for the following simulations.
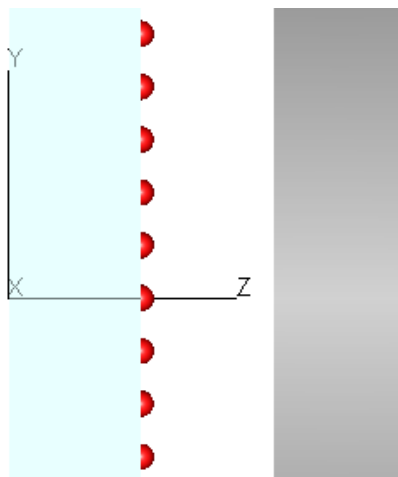
Fig.4.8: The profile structure used during the simulations, it is shown in gray the absorbing wall that was used for the data analysis and that is much extended than the device active area under test.
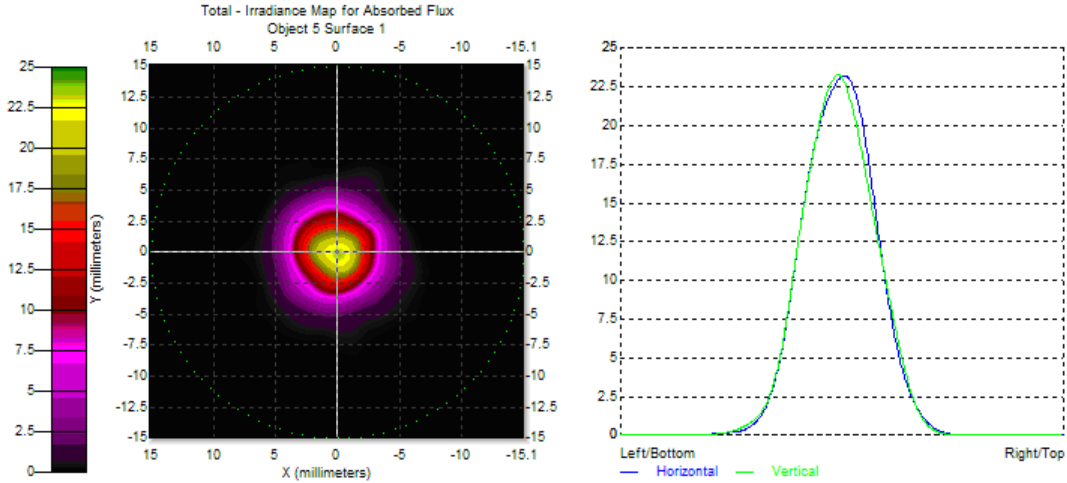
Fig. 4.9: Distribution of incident rays regarding the simulation performed without the presence of microlens.

Then, we have carried out three types of analysis, the first devoted to the geometry of the microlens, the second regarding the material to be used and a third related to the pattern density of microlenses on the substrate.

The first analysis was performed by varying the height of the microlenses to realize the best compromise. In figure 4.10 you can observe the evolution of the simulated data about the device efficiency in function of the ratio between the height and the base radius of the microlenses. The percentage improvement of photon emission, which we call for simplicity η_{en}, is given by equation 4.4:

$$\eta_{en} = \frac{P_{micro} - P_{nomicro}}{P_{nomicro}} * 100$$

(4.4)

where P_{micro} is the output light power come from the substrate surface with the presence of microlens and $P_{nomicro}$ is the output power come from the substrate surface perfectly flat.

This first analysis reveals that the best performance is obtained with microlenses having the form closest to a hemisphere.
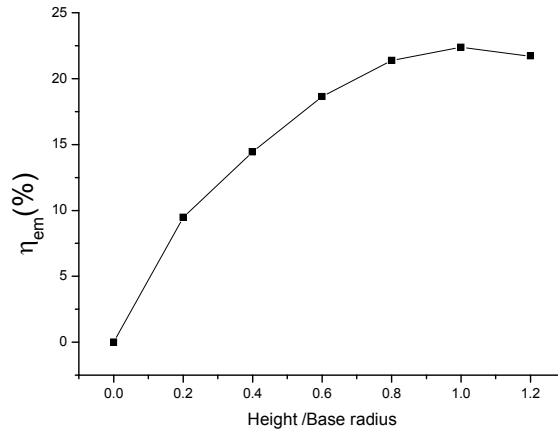
Fig. 4.10: The simulated data for the percentage improvement of photon emission versus the ratio between the height and the base-radius of the microlenses.

The second analysis was performed for the choice of materials used in the microlenses manufacture. From these simulations (figure 4.11) the data shown that the most appropriate refractive index is the one that approaches close as possible to the substrate one. This type of analysis is essential if we keep in mind the data reported in table 4.2.
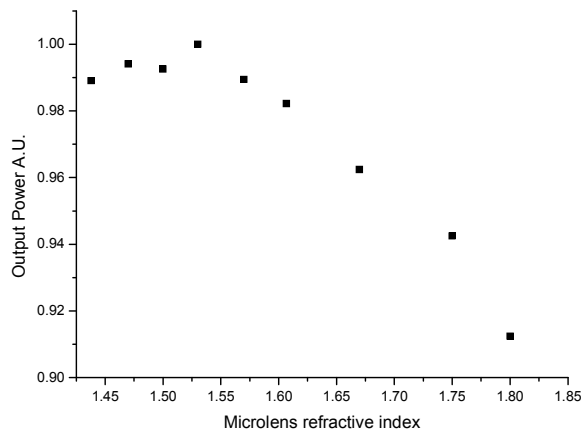
Fig. 4.11: Normalized output power versus the microlens refractive index.

The third analysis was carried out by changing the density of patterned microlenses in a way that the density was respectively 2, 3 and 4 times the size of the first geometry, figure 4.12.
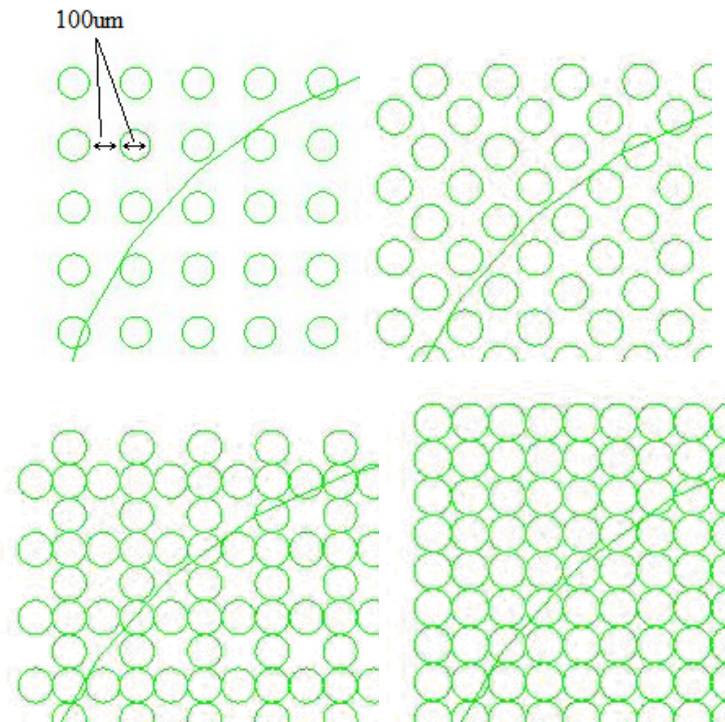
Fig. 4.12: Microlenses patterning used during the simulations.

The evolution of output power versus the change of microlenses density is shown in figure 4.13, this trend shows us how important it is cover the substrate surface to eliminate most of the light trapped paths.
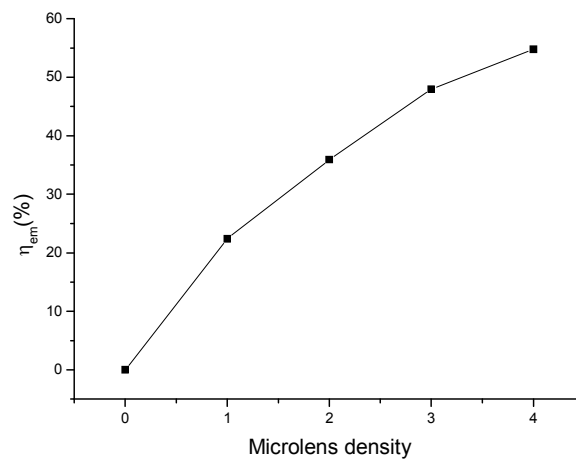
Fig 4.13: The simulated data for the percentage improvement of photon emission versus the microlenses density.

Although this behaviour follow for a while the one predicted in literature [21] it start to saturate and probably could still be improved for a while if we pack in other ways the microlenses but finally there were active device areas left uncovered and without the microlenses presence.

4.3.2 Experimental

Microlenses and microlens arrays can be used for beam shaping purposes like collimation and focusing (e.g. in combination with laser-diode arrays, detector arrays or fibres), for illumination (e.g. in display systems and projection systems) and for imaging purposes.

Various fabrication techniques have been proposed for this purpose [22]; among these are photothermal expansion, ion exchange and CO_2 laser irradiation. More recently fabrication techniques of microoptical components in new lightweight optical materials have become the research topic of interest.

Several researchers have reported on fabrication methods for microlenses and lens arrays with these materials. They include techniques like photoresist reflow [23], laser beam shaping [24], deep lithography with protons [25], photopolymerization [26], microjet printing [27], laser ablation and direct laser [28], e-beam writing [29] or electrowetting process [30].

Here we present some experimental results about the realization of a microlenses array by gravure printing technique using a metal moulder realized by CSEM (Centre Suisse d'Electronique et de Microtecnique) of Zurig [31] (figure 4.14).

For this purpose it was deposed by casting technique on a glass substrate a layer of Sylgard 184 PDMS (Polydimethylsiloxane) supplied by DowCorning, after the polymer deposition the substrate was pressed with the CSEM molder to obtain the microlenses surface profile and putted into the oven at 115 K waiting the end of polymerization process (25minutes baking in clean room atmosphere).
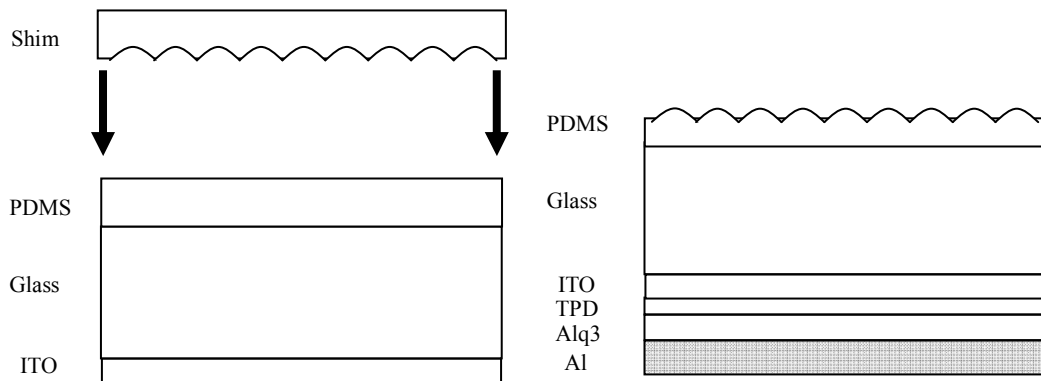
Fig. 4.14: Illustrative picture with the substrate and the shim molder (right). The ultimate divice with of the presence of the PDMS microlenses (left).

The realized profile was measured by Tencor alpha-step IQ and it is reported in figure 4.15. The OLED device was realized only at the end of the implementation process of microlenses array.
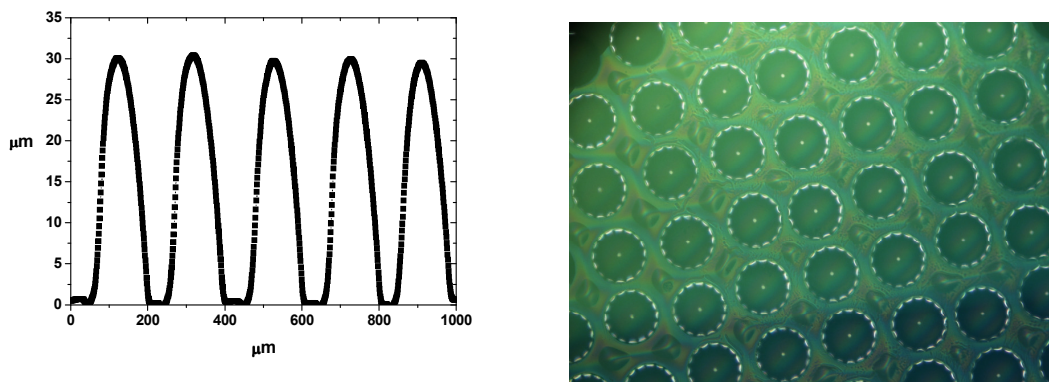
Fig. 4.15: A profile of the realized PDMS microlenses (left) and a photo of the array realized by a microscope.

The efficiency behaviour of the device with the presence of a flat PDMS layer and with the microlens array is reported in figure 4.16. The reported improvement of luminance efficiency in this study is around 25% and is more pronounced than the one predicted in figures 4.10 and 4.13, with a height-base ratio around 0.5, probably because a higher microlenses density in our experiment respect to the one reported in the proposed simulation.
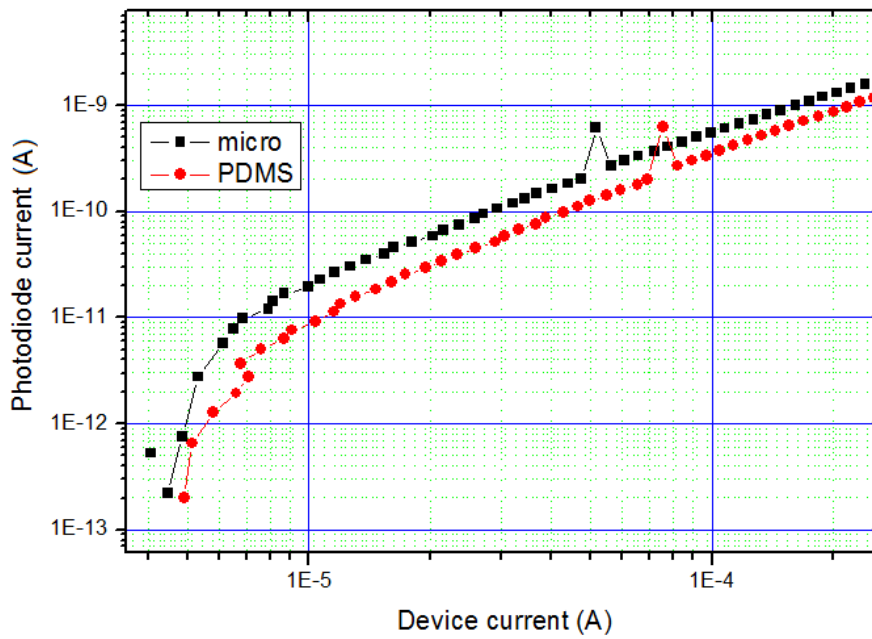
Fig. 4.16: The photodiode current versus the device current with the presence of a flat PDMS layer (red) or with the microlens array (black).

The effect in the use of the microlens array it is evident with a substantial reduction in the trapped light and so a less relevant effect on the border of the substrate (figure 4.17). Furthermore, the active area seems to be increased because of the rays that are not out-coupled with the first light path and are also guider for a while.
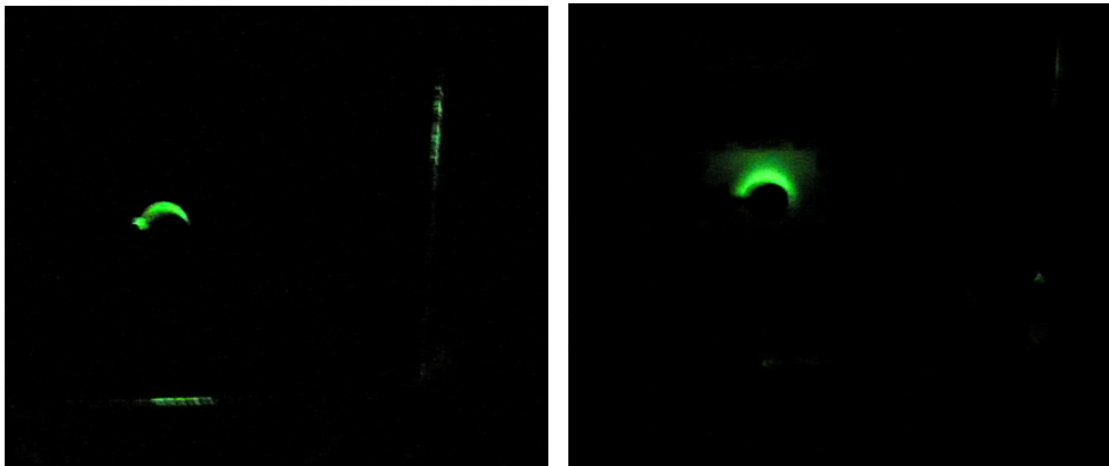
Fig. 4.17: Two picture of the devices under test from the cathode side. On the left is reported the picture of the device with the flat PDMS layer in which is evident the border of the substrate because of the trapped light. On the right is reported the picture of the device with the presence of microlens array.

4.4 TCO and substrate Texture

Another way to improve the external efficiency is the fabrication of texture structure to guide the light in transversal way using the same effect that guide the light along the substrate. To achieve this result we prepared a pattern on the glass side (using a buffered HF solution) of our substrate by photolithographic process and the related profile is reported in figure 4.18.

Analyzing the ultimate structures at the profilometer was noted, as expected, a higher roughness respect to the untreated substrate, and also the formation of a tilt angle θ [19], which amplifies the effect to funnel structure and further facilitates the photons emission. These two properties have provided further justification taking into account the measures realized with a first campaign of OLED devices.
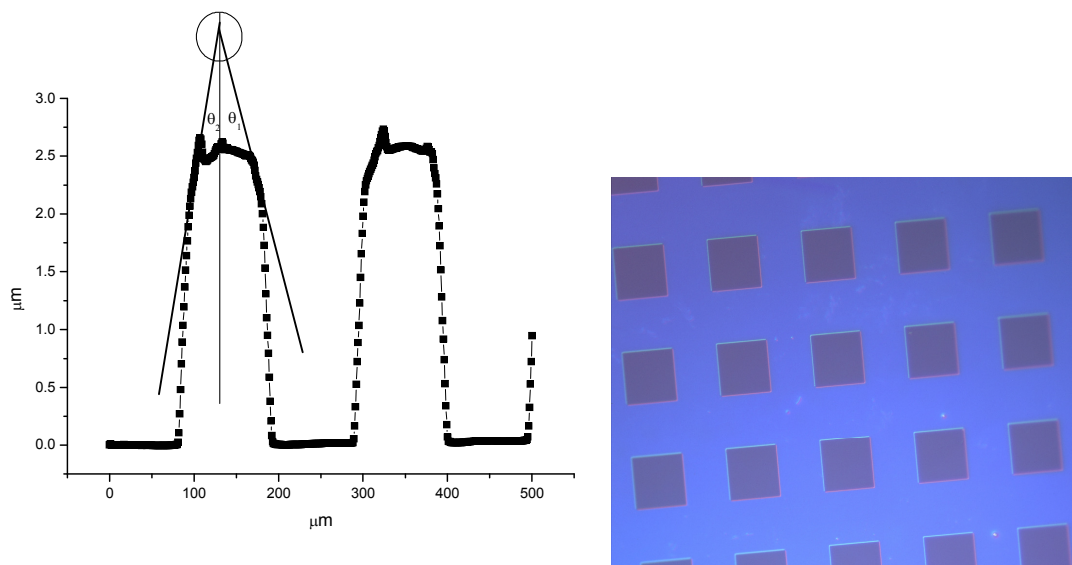
Fig 4.18: Profile of the realized structure on the glass surface (left) and a microscope picture of the realized structure (right).

This kind of pattern was reproduced also on the anode contact (ITO) for a further set of devices wrinkling the metal contact (Al) which redirects the light towards the glass substrate in a way like the one illustrated in figure 4.6. From figure 4.19 we can see that the profile of the structure realized on ITO is slightly concave which helps to improve the emission of photons too.
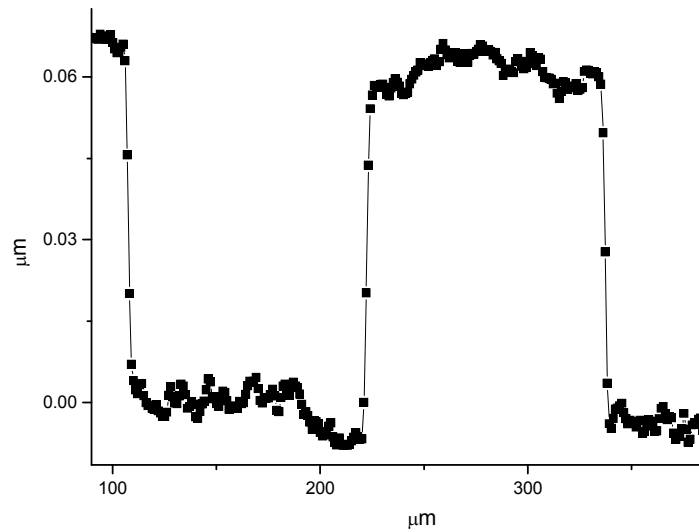
Fig 4.19: Profile of the realized structure on ITO surface.

The realized devices structures in this experiment can be summarized as follows:

- GLASS/ITO/TPD/AlQ3/Al (reference)
- TEXTURED GLASS /ITO/TPD/AlQ3/Al
- GLASS/ TEXTURED ITO /TPD/AlQ3/Al

The analysis of the devices external efficiencies showed many differences between the proposed structures. If we report the photodiode current versus the device current, we realize that the best performances are achieved with the device realized on the textured substrate (figure 4.20). In particular, we can note that in proximity of 1 mA the devices made on the untreated substrate report a reduction in the light emission of about 30% while the devices made on texturized report a difference in the light extraction off about the 13%. These measures reveal a noticeable improvement in the performance in both types of textured devices, so it can be a good approach to the external efficiency issues in OLED devices.
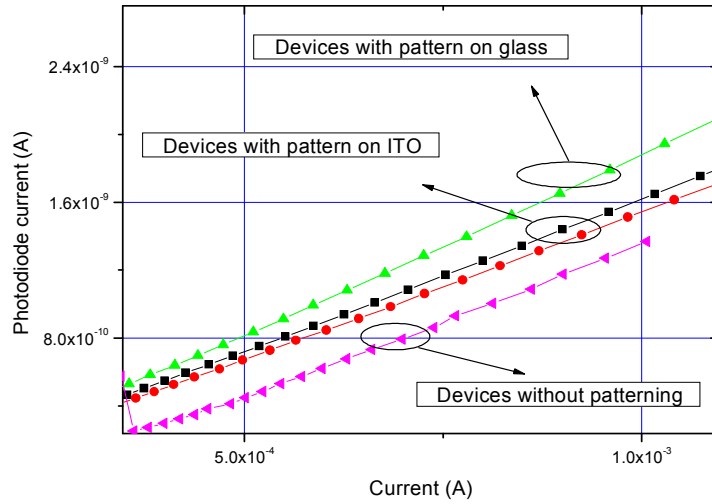
Fig. 4.20: Performances of textured devices compared with a "classic" device one.

However, it should be said that the difference in the performances between the two textured devices is attributable only to the fact that the variation in index between the ITO and the glass substrate is less relevant than the difference in refractive index between the substrate and air.

Furthermore it have be also said that the two techniques are not mutually restricted but can and should be used simultaneously in order to have an additional advantage in improving the absolute performance.

References

[1] N. K. Patel, S. Cinà, and J. H. Burroughes "High-Efficiency Organic Light-Emitting Diodes", IEEE Journal on selected topics in quantum electronics, Vol. 8, No. 2 (2002)

[2] Chihaya Adachi, Marc A. Baldo, Mark E. Thompson, and Stephen R. Forrest Nearly "100% internal phosphorescence efficiency in an organic light emitting device", Journal Of Applied Physics Vol. 90, No. 10,15 (2001)

[3] Ji-Seon Kim, Peter K. H. Ho, Neil C. Greenham, and Richard H. Friend "Electroluminescence emission pattern of organic light-emitting diodes: Implications for device efficiency calculations" Journal of Applied Physics Vol. 88, No. 2 (2000)

[4] H. Becker, S. E. Burns, and R. H. Friend, "Effect of metal films on the photoluminescence and electroluminescence of conjugated polymers" Phys. Rev. B, vol. 56, pp. 1893–1905 (1997)

[5] Y. Shi and Y. Yang, "Device performance and polymer morphology in polymer light emitting diodes: The control of thin film morphology and device quantum efficiency," J. Appl. Phys., vol. 87, p. 4254 (2000)

[6] V. Bulovic, V. B. Khalfin, G. Gu, P. E. Burrows, D. Z. Garbuzov, and S. R. Forrest, Phys. Rev. B 58, 3730 (1998)

[7] L.H. Smith, W.L. Barnes, "Using a low-index host layer to increase emission from organic light-emitting diode structures", Organic Electronics, 7, 490–494 (2006)

[8] 30% external quantum efficiency from surface textured, thin-film light-emitting diodes I. Schnitzer and E. Yablonovitch Appl. Phys. Lett., Vol. 63, No. 16, (1993)

[9] R.Windisch, P. Heremans, A. Knoloch, P. Kiesel, G. H. Döhler, B. Dutta, and G. Borghs, "Light-emitting diodes with 31% external quantum efficiency by outcoupling of lateral waveguide modes", Applied Physics Letters, vol. 74, pp. 2256 (1999)

[10] Takashi Yamasaki, Kazuhiro Sumioka, and Tetsuo Tsutsui "Organic light-emitting device with an ordered monolayer of silica microspheres as a scattering medium", Applied Physics Letters, Vol. 76, No. 10 (2000)

[11] Yoshitaka Izumi, Shinji Okamoto, Kuniharu Takizawa and Katsu Tanaka, "Improving the Light Out-Coupling Properties of Inorganic Thin-Film Electroluminescent Devices", Jpn. J. Appl. Phys., Vol. 41, pp. 1284–1287 (2002)

[12] Weixin Li et al. "Maximizing Alq3 OLED Internal and External Efficiencies" Journal of Display Tech., Vol. 2, No. 2 (2006)

[13] C. F. Madigan, M. H. Lu, and J. C. Sturm, "Improvement of output coupling efficiency of organic light-emitting diodes by backside substrate modification" Applied Physics Letters, Vol. 76, No. 13 (2000)

[14] Ming-Lung Chen, An-Chi Wei, and Han-Ping D. Shieh, "Increased Organic Light-Emitting Diode Panel Light Efficiency by Optimizing Structure and Improving Alignment of Pyramidal Array Light-Enhancing Layers" Japanese Journal of Applied Physics Vol. 46, No. 4A, pp. 1521–1525 (2007)

[15] G. Gu, D. Z. Garbuzov, P. E. Burrows, S. Venkatesh, and S. R. Forrest , M. E. Thompson, High-external-quantum-efficiency organic light-emitting devices Optics Letters, Vol. 22, No. 6 (1997)

[16] Yiru Sun and Stephen R. Forrest "Enhanced light out-coupling of organic light-emitting devices using embedded low-index grids" Nature Photonics, vol. 2, 483-487 (2008)

[17] John M. Lupton, Benjamin J. Matterson, and Ifor D. W. Samuel "Bragg scattering from periodically microstructured light emitting diodes" Applied Physics Letters Vol. 77, No. 21 (2000)

[18] Yong-Jae Lee, Se-Heon Kim, Joon Huh, Guk-Hyun Kim, Yong-Hee Lee, Sang-Hwan Cho, Yoon-Chang Kim, and Young Rag Do "A high-extraction-efficiency nanopatterned organic light-emitting diode", Applied Physics Letters, Vol. 82, No. 21 (2003)

[19] Huajun Peng, Yeuk Lung Ho, Xing-Jie Yu, Man Wong, and Hoi-Sing Kwok, "Coupling Efficiency Enhancement in Organic Light-Emitting Devices Using Microlens Array - Theory and Experiment" Journal of Display Tech., Vol. 1, No. 2 (2005)

[20] S. Moller et al. "Improved light out-coupling in organic light emitting diodes employing ordered microlens arrays" Journal of Applied Physics Vol. 91, No.5 (2002)

[21] Mao-Kuo Wei, I-Lin Su "Method to evaluate the enhancement of luminance efficiency in planar OLED light emitting devices for microlens array" Optics Express Vol. 12, No 23, 5777-5782 (2004)

[22] H. Ottevaere, R. Cox, H. P. Herzig, T. Miyashita, K. Naessens, M. Taghizadeh, R. Völkel, H JWoo and H. Thienpont, "Comparing glass and plastic refractive microlenses fabricated with different technologies", Journal of Optics A: Pure Appl. Opt. Vol. 8, S407-29 (2006)

[23] Popovic Z. D., Sprague R. A. and Neville Connell G. A. "Technique for monolithic

fabrication of microlens arrays" Appl. Opt. Vol. 27, pp. 1281-4 (1988)

[24] Jay T. R. et al. "Preshaping photoresist for refractive microlens fabrication", Opt. Eng., 33, 3552-5 (1994)

[25] Ottevaere H, Volckaerts B, Lamprecht J, Schwider J, Hermanne A, Veretennicoff I and Thienpont H. "2D plastic microlens arrays by deep lithography with protons: fabrication and characterization", J. Opt. A: Pure Appl. Opt. Vol. 4 S22-8 (2002)

[26] Croutx´e-Barghorn C., Soppera O. and Lougnot D. J. "Fabrication of refractive microlens arrays by visible irradiation of acrylic monomers: influence of photonic parameters", Eur. Phys. J.: Appl. Phys. Vol. 13, pp.31-7 (2001)

[27] MacFarlane D. L., Narayan V., Cox W R, Chen T. and Hayes D. J. "Microjet fabrication of microlens arrays" IEEE PTL 6, pp.1112-4 (1994)

[28] Naessens K., Ottevaere H., Baets R., Van Daele P. and Thienpont H., "Direct writing of microlenses in polycarbonate with excimer laser ablation", Appl. Opt. Vol. 42, pp. 6349-59 (2003)

[29] Kley E. B., Possner T. and Göring R. "Realization of micro-optics and integrated optic components by electron-beam lithographic surface profiling and ion exchange in glass" Int. J. Optoelectron., 8, pp. 513-27 (1993)

[30] S. Grilli, L. Miccio, V. Vespini, A. Finizio, S. De Nicola, and P. Ferraro "Liquid micro-lens array activated by selective electrowetting on lithium niobate substrates". Optics Express, 16, pp. 8084-93 (2008).

[31] www.csem.ch

CHAPTER V

"Light scattering and OLED efficiency"

In this last chapter, experimental measurements on polystyrene-ZnO nanocomposite scattering films and on organic light emitting device (OLED) with and without the scattering layers are presented and compared with Henyey-Greenstein radiative-transfer model to narrow down the parameters that can be important in the identification of more suitable scattering layers. The results yield to an increase of efficiency of about ~30% that it can be translated in a ~60% of outcoupled light respect to the total generated amount.

5.1 Light scattering layer on OLED light output.

In the last years several strategies were developed concerning the surface modification to increase the efficiency factor by using ordered micro-lenses, bragg reflectors, 2D photonic crystal or modifying the cavity effects [1-4]. In all these high-tech applications, that sometime require dedicated processing tools and/or new materials with special properties, there is not only an improvement in the light extraction but also a substantial modification in angular device light intensity and/or spectrum [2-4]. Another approach can be played by a more unsophisticated structure simply performing polymer-matrix by spin-coating or casting processes introducing scattering centres consisting of nanoparticles that locally change the refractive index [5-11].

Following the last approach, in many papers [5,6,11], the analysis of volumetric scattering layers has been addressed to determine the right optical parameters (reflectance, transmittance and scattering properties) and make them suitable for the employment in OLED light out-copupling purposes.

In this chapter will be exposed the advantages of Polystyrene-ZnO nanocomposites as volumetric light scattering layers in OLED lighting applications.

We tried to obtain the out-coupling enhancements already reported in literature by means of thinner scattering films. In our approach, we focussed on high-concentrations of nanoparticles in polymeric films to increase the probability of the scattering event between small refracting index differences in mediums. To accomplish this task, we adopted ZnO dispersions in Polystyrene (PS) films which are already reported in some works where several PS/ZnO nanocomposites have been investigated considering the effects of nanoscale ZnO on the electrical and physical characteristics of PS nanocomposites [12, 13]. In particular, Chae and Kim found that the thermal stability of PS was enhanced with increasing ZnO content [13].

In this chapter, experimental measurements on polystyrene-ZnO nanocomposite scattering films and on organic light emitting device (OLED) with and without the scattering layers are presented and compared with Henyey-Greenstein radiative-transfer model to narrow down the parameters that can be important in the identification of more suitable scattering layers.

5.2 An introduction on the theory of light scattering

A single particle can be considered a collection of tiny dipolar antennas driven to radiate (scatter) by an incident oscillating electric field. Scattering depends on size and shape, the observation angle called scattering angle, the response of the individual particle, on the polarization state and frequency of the incident wave. Geometry, composition of the medium, and the properties of the illuminating source are the fundamentals for the effect of scattering by particles [14].

If now, a particle is illuminated by a beam with irradiance I_i. The total power scattered by this particle is W_s. The scattered power will be proportional to the incident irradiance and this proportionality can be transformed into an equation by means of a factor K_s (eq. 5.1):

$$W_s = K_s * I_i \tag{5.1}$$

For equation 5.1 to be dimensionally correct K_s must have the dimensions of an area, for this reason K_s takes the name of scattering cross section.

Particles absorb as well as scatter electromagnetic radiation. The quantity absorbed W_a by an illuminated particle, like scattered power, is proportional to the incident irradiance (eq. 5.2):

$$W_a = K_a * I_i \tag{5.2}$$

where K_a is the absorption cross section. The sum of these cross sections is the extinction cross section (eq. 5.3):

$$K_e = K_s + K_a \tag{5.3}$$

The extinction cross section can be determined by measuring transmission by a portion of material populated by N identical particles per unit volume. Provided that multiple scattering is negligible, the incident and transmitted irradiances I_i and I_t are related by (eq. 5.4):

$$I_t = I_i \, exp(-NK_e \, h) \tag{5.4}$$

where h is the thickness of sample under test. Only the sum of scattering and absorption can be obtained from transmission measurements. To separate extinction into its components requires additional measurements.

Equation 5.4 requires that all particles are identical. They are different if they differ in size, shape, composition, or orientation. Equation 5.4 can be generalized to a distribution of particles by replacing NK_e with (eq. 5.5):

$$\sum_j N_j * K_{e,j} \tag{5.5}$$

where j denotes all parameters distinguishing one particle from another .

Instead of cross sections, normalized cross sections called efficiencies or efficiency factors, Q_s, Q_a, and Q_e, often are presented. The normalizing factor is the particle's area G projected onto a plane perpendicular to the incident beam. No significance should be attached to efficiency used as shorthand for normalized cross section. The normalization

factor is arbitrary. It could just as well be the total area of the particle or the area of his thumbnail.

Proper efficiencies ought to be less than unity, whereas efficiencies for scattering, absorption, and extinction are not so constrained. Moreover, some particles (for exemple the aggregates) do not have well-defined cross-sectional areas. Such particles have cross sections for scattering and absorption but the corresponding efficiencies are not well designed.

If any quantity deserves the designation efficiency it is the cross section per particle volume v. Equation 4 can be rewritten to display this (eq. 5.6):

$$I_t = I_i \exp[-fh(K_e/v)] \qquad\qquad (5.6)$$

where $f=Nv$ is the total volume of particles per unit slab volume. For a given particle loading, specified by fh (volume of particles per unit slab area), transmission is a minimum when K_e/v is a maximum.

5.2.1 Henyey-Greenstein and free mean path

The HG function was first presented in 1941 by Henyey and Greenstein in the astrophysical literature. It was employed to approximate Mie scattering [15] in the study of diffuse radiation in galaxies [16]. It has no physical basis, and was introduced to fit scattering data of stellar radiation. However, it has since been widely used in many different fields that require light scattering approximations due to its mathematical tractability.

As already stated the form of the phase function is quite complex to analyze using Mie theory approach [15], but we shall further simplify our analysis by using two parameters analysis: one angular and another spatial. The first is the Henyey and Greenstein phase function [16] due to the difference in the refractive index between matrix and particles and the second is the scatterance due to the mean free path from a scattering event to another.

The Henyey-Greenstein scattering distribution function can be written in this way:

$$p(\theta) = \frac{1 - g^2}{4\pi(1 + g^2 - 2g\cos\theta)^{3/2}}$$ (5.7)

where g parameter is the so-called *anisotropy* of the scattering layer and gives rise to the shape of the output profile as a response to an incident light beam (figure 5.1).
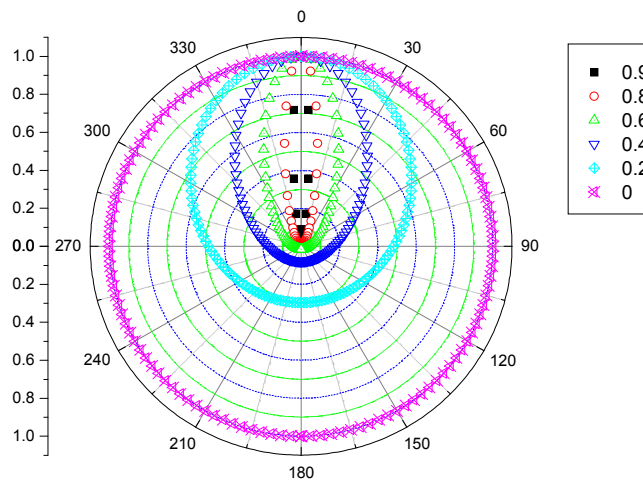
Fig. 5.1: The normalized Heney-Greinstein phase function distribution

Furthermore, for a directly consequence of eq. 5.6, when a ray enters in the scattering film, it will be propagated with a random distance x and with a distribution of probability (eq.5.8):

$$P(x) = e^{-sx} dx$$ (5.8)

where the s parameter is the scattering coefficient [5,6].

5.3 Scattering nanocomposite-polymer matrix

PS (with average Mw~192,000) and ZnO nanopowder (with average size<100nm) are commercially available products from Aldrich.

Chlorobenzene (Clbenz) was selected as a co-solvent of PS and ZnO. PS/ZnO

nanocomposite layers with varying concentrations of ZnO were prepared by solution mixing technique. PS was dissolved in Clbenz at 90°C for 30min with vigorous stirring at concentration of 15wt%. ZnO was dispersed in this solution by ultrasonic vibration for 10min. ZnO contents were 10 and 20% based on the polymer matrix.

To obtain a nanocomposite layer, the suspensions PS/ZnO were spin coated (with 500rpm for 30sec) onto glass side of the ITO-coated "Float glass" substrates, purchased from Delta Technology. These substrates are provided with a passivation layer of about 300Å of SiO_2 between the glass and a 120nm to 160nm-thick Indium-doped Tin Oxide (ITO) layer having a sheet resistance (Rs) from 8 to 12 $\Omega/\square$.

The optical parameters for the substrates and the ITO layer were specified by supplier [17]. Nominal refracting index was 1.517 for the float glass substrate and n = 1.775 and k = 0.012 for ITO. Substrate tichkness was 1.1 mm and declared optical transmittance grater than 83%.

The substrates were cleaned by sonication in deionised water and detergent and dried in oven at 115°C for 2 hours.

In this study, a basic double-layer OLED configuration was fabricated with a 40 nm thick NPD film as HTL (Hole Transport Layer) and a 60 nm thick Alq3 film as ETL (Electron Transport Layer), see figure 5.2.
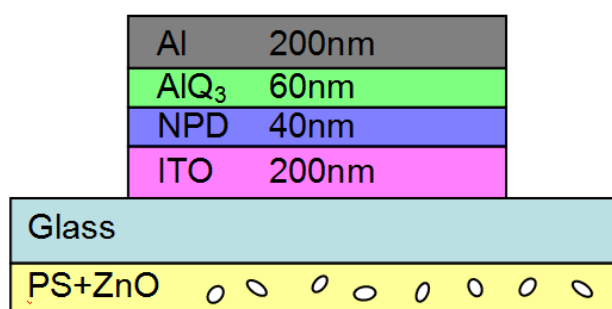
Fig.5.2: The device structure considered in this work.

Active layers of our OLEDs were deposited on ITO patterned anodes.

In this configuration, Alq3 is both ETL and emissive layer (EML). An Aluminium (Al) cathode was finally evaporated to complete the device structure.

The anodic structures were patterned through inverse photolithography and HCl-based solution etching.

From the ITO side, the organic layers were thermally evaporated sequentially with no vacuum breaking between their depositions. The pressure in deposition chamber was kept always between 10^{-6} and 10^{-7} mbar and the growth rate for the organic layers was between $1 \div 2$ Å/s. The Al cathode was evaporated through shadow mask, with growth rate of about $2 \div 3$ Å/s determining a circular active area having a diameter of 4 mm.

For this study, we have fabricated six different series of devices as reported in table 1. PS/ZnO films at different thickness are obtained by depositing several layers of dispersion.

Table 1. Thickness and ZnO contents in the PS/ZnO nanocomposite layers

Device	Thickness of scattering layer (μm)	ZnO (%)
A	no layer	0
B	4.6	0
C	5.1	10
D	8.3	10
E	12.1	10
F	5.3	20

The films thicknesses have been evaluated by a KLA Tencor P-10 Surface Profiler.

To have an idea about the optical performance of our scattering films we realized two of them on quartz substrate as the two realized for the devices C and F (see table 1)

The transmittance spectra have been measured with a Perkin_Elmen lambda 900 spectrophotometer.

The scanning electron microscopy (SEM) images were performed by means of a LEO 1530 microscope while the Atomic Force Microscopy (AFM) pictures were performed by means of a Nanoscope 4 from Digital Instruments VEECO.

The current-voltage (I-V) measurements on OLED devices were performed by a Keithley 2400 Power Supply Source-Meter in voltage mode, with constant increment steps and delay time of 1s before each measurement point. A calibrated integrating sphere, with a

circular open window of about 1cm diameter on which are mounted the devices, and a photodiode (Newport 810UV) connected to a Keithley 6517A Electrometer were employed for the Electroluminescence (EL) analysis. The Newport 810UV photodiode was used also to perform the angular measures.

5.4 Modelling and understanding of scattering processes

Optical measurements were performed at different nanoparticles concentrations on scattering films before testing them coupled with OLEDs in order to investigate the effects of light scattering before the realization of a complete device.

5.4.1 Scattering film characterization

The ZnO nanoparticles were characterized by SEM and AFM imaging to analyze the shape and size (fig. 5.3 and 5.4). From those images we can see that the nano-particles are not spherical and they are much more similar to nano-rods with the long axis around 200nm or smaller.

From the spectrophotometer measurements performed on the scattering films is possible to see (fig. 5.5) no appreciable absorption in the visible range. Furthermore, the two kinds of ZnO dispersion percentage are very simple to resolve and discriminate.
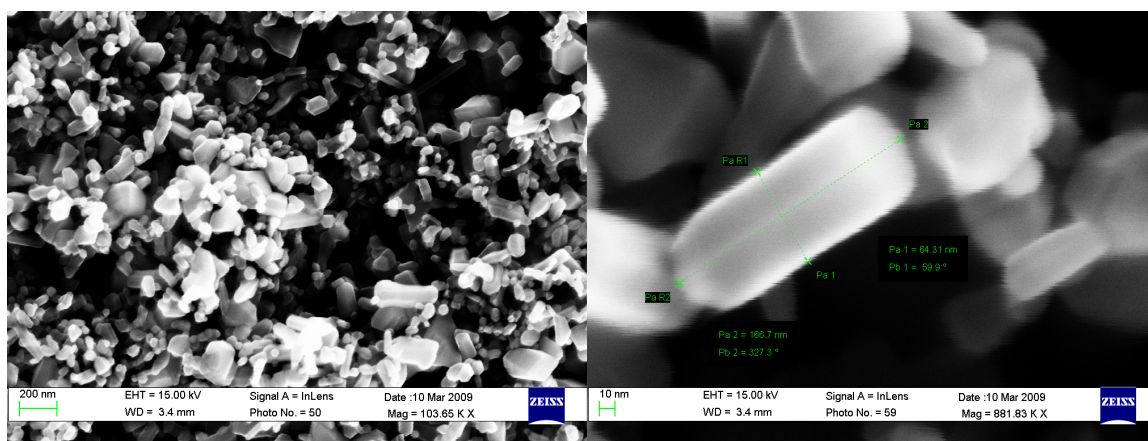
Fig. 5.3: SEM image of ZnO nanoparticles deposited on a silicon substrate, and a particular zone of the same image.
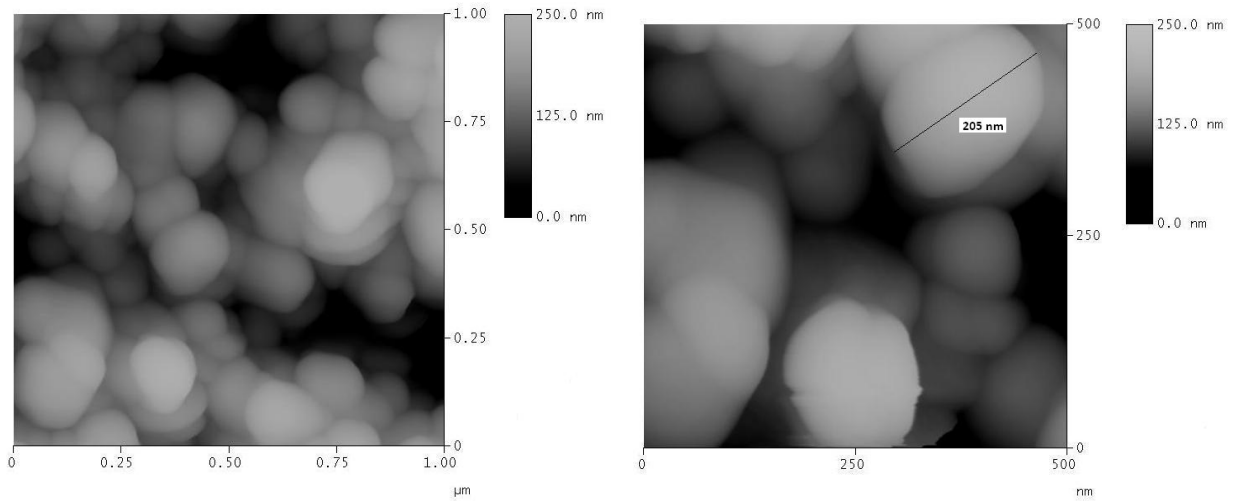
Fig. 5.4: AFM images of a ZnO nanoparticles layer deposited on a glass substrate at different magnifications.

For both PS/ZnO films is possible to see a decrease in transmittance and a relative increase in the reflectance from 800nm to 400 nm range following the refractive index variation in the same wavelength range of the ZnO nanoparticles [18,19].

The simple PS layer without nanoparticles shows a very good transmission (higher than 90%) almost on all over the investigated range from 2500nm to 250nm. From the same measure we can observe that our film give rise to interference effects we utilized to evaluate the refractive index [20-22], that is approximaterly near to n=1,58. This effect is broken by the presence of nanoparticles and the consequent scattering mechanism for the PS/ZnO layers.
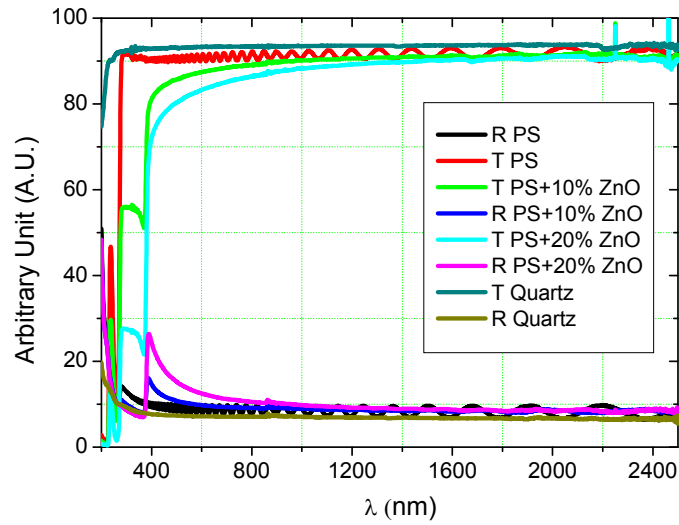
Fig. 5.5: Transmittance (T) and reflectance (R) spectra related to the free standing quartz substrate, PS film, and to two nanocomposites with 10% and 20% of ZnO.
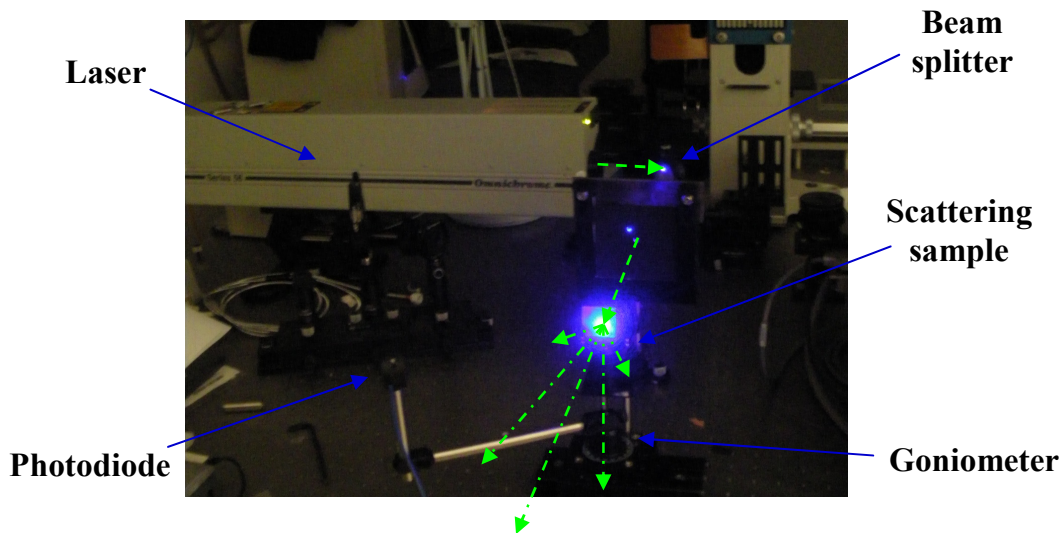
Fig. 5.6: One of the equipment configuration used for the angular resolved measurements campaign.

For further investigations we realized angular measurements to describe the ellipsoid profile determined by the light coming out from the sample when it has been irradiated by a laser source ($\lambda \sim 442$nm) perpendicularly (fig. 5.6).

In figure 5.7 were shown the results coming from the angularly-resolved intensity versus for the two PS/ZnO nanocomposites with 20% of ZnO.

Since *n* matrix is determined, we can perform our simulation using (eq. 5.7) and (eq. 5.8), changing g and s to acceptably fit the data coming from the angular measurements, as shown in figure 5.7.

In particular, the *g* parameter results to be slightly higher than literature results [5,6] but this can be easily explained if we consider the little refractive index difference between the polymer matrix (1,58) and the particles (from 1.9 to 2.1) [15]. Furthermore, nanoparticle shape can induce an increase in the *g* parameter [23] if compared to the one obtained by perfectly-spherical nanoparticles.
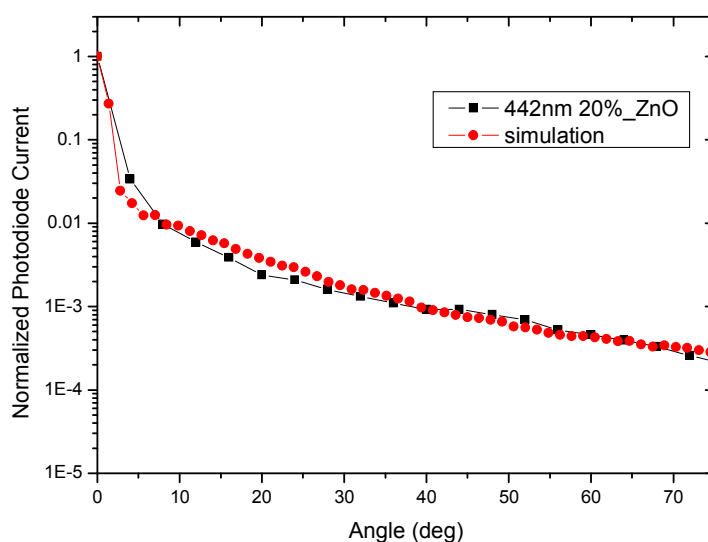
Fig. 5.7: The angularly resolved normalized intensity versus angle for the scattering film performed on quartz with the presence of 20% of nanoparticles. The simulated data were obtained with g~0.91 and s~200 1/mm

With an anisotropy factor around 0.9 or higher, as discussed in such papers [11], we obtained a very broad optimum zone leading to an enhancement of OLED light output as a function of scatterance with a consequent easier way to reach the optimum of behaviour.

Furthermore, regarding this results to the glass substrate (n~1.52) we have a good scattering film with a refractive index matrix little bit higher than the substrate one.

These results give the possibility to the light to completely pass from the glass to the scattering layer. Even if the device active area seems to optically increase, because the light is not only scattered but also guided, we will have an increase in the OLED efficiency too (fig. 5.8).
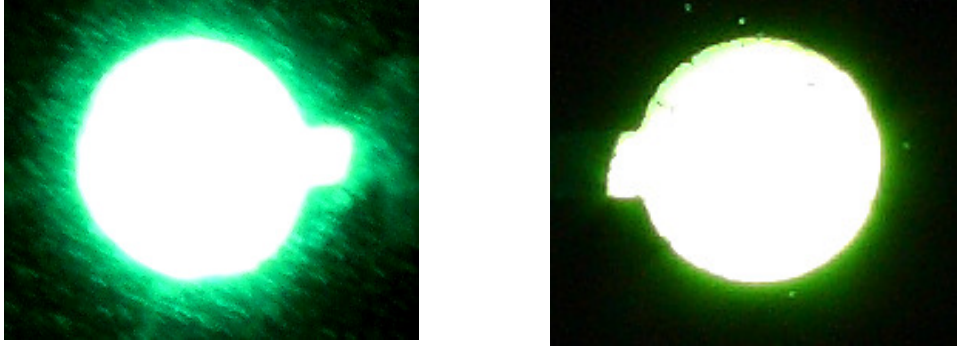
Fig. 5.8: A working OLED picture with the scattering layer (left) and with the PS layer without the ZnO nanoparticles.

5.4.2 Device characterization

In presence of light scattering, one of the most critical parameters in the determination of light extraction is the effective cathode reflectivity. In figure 5.9 is showed the cathode reflectivity related to our stacked device in the same range of wavelength of the OLED spectra. For the chosen range of wavelengths the reflectivity values is always much higher than 80% that is a good compromise for the aims of our investigation [5][11].
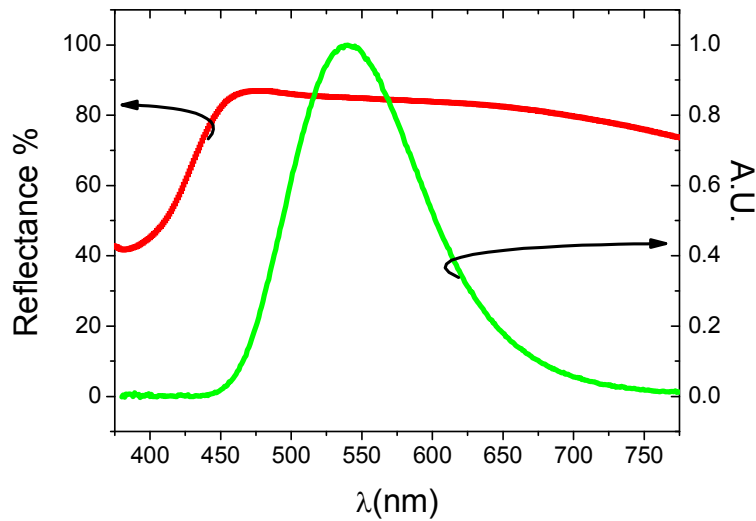
Fig. 5.9: Measured cathode reflectivity from the glass side through the OLED device and the normalized spectra measured from our devices.

Scattering films with different particles concentrations and different thickness were performed (see table 1) and their effect on light out-coupling on the associated OLED efficiency was evaluated realizing six different devices.

A first measure to evaluate the total internal reflection and the relative trapped light on device A was performed introducing the device inside to an integrating sphere and than mounting the same device outside in front of the optical window as previously described.

As expected, only the 30% of light is able to goes through the glass substate [24]; thus, the trapped light amount is around 70% and it is completely loss.

Now we are able to evaluate correctly the efficiency improvement of our devices simply performing the measurement on the remaining devices accomplishing to the plots of figure 5.10 where it is shown the luminance behaviour versus the devices current density.

Analysing the data of our devices is possible to note an improvement of efficiency in both the directions, increasing the ZnO wt% or the thickness of scattering layer.
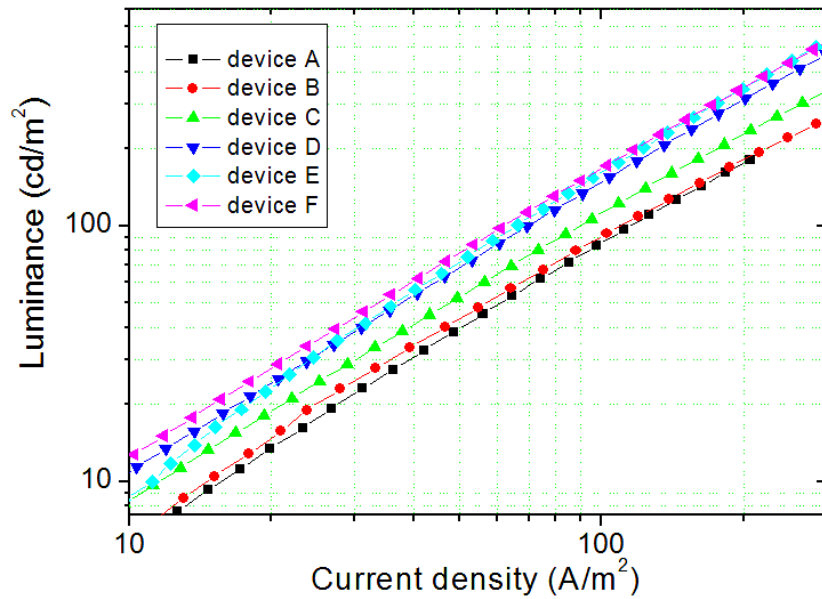
Fig. 5.10: Luminance versus current density of OLED devices.

In particular, a maximum enhancement of luminance of about 1.7 times is observed for devices E and F that can be translated in a ~30% of improvement respect to the out-coupled light and in a ~60% of light that can be utilized respect to the totally generated.

These results indicate also a saturation behaviour of efficiency versus the scattering layer thickness as expected. In fact, it is due to the optical parameters of our PS+ZnO nanocomposite, and in particular to the g parameter value, and for these reason the peak of efficiency is shifted to high scatterance values. To this regard in figure 5.11 the behaviours about the angularly resolved normalized intensity versus angle for the scattering film performed on glass substrate are presented using the same technique to obtain the profile of figure 5.7.

Furthermore, this result demonstrate once again that our films have no relevant absorption (fig. 5.5) and so it does not matter if the peak for the outcoupling efficiency is achieved by changing the nanoparticle concentration, or through adjusting the free mean path in the film by increasing the thickness.
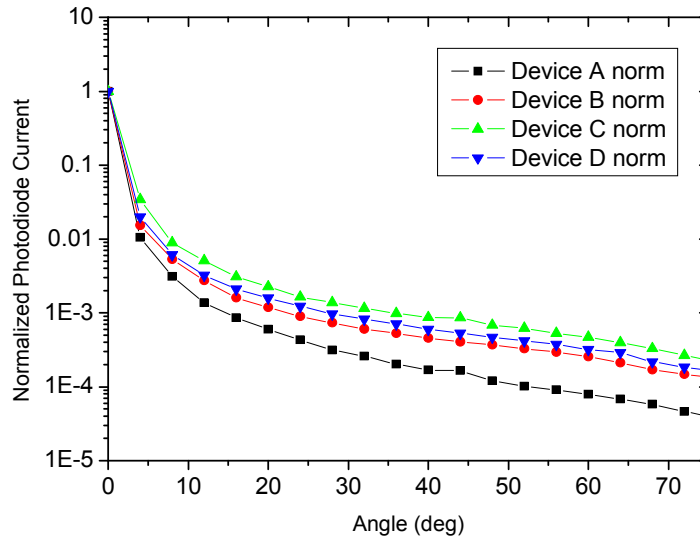
Fig. 5.11: The angularly resolved normalized intensity versus angle for the scattering film performed on glass

Another observation that we have to underline is that using so high concentration of nanoparticles also the film roughness will change, especially if there is formation of clusters, but in this moment we didn't care about it [25,26].

To complete our analysis we performed angular measurements to investigate if the film under examination has an impact on the device light emission profile.

The method that was used to detect the angular emission consist in placing the OLED device on a goniometer while a photodiode was mounted at about 10cm of distance in a way that the centre of the device is exactly in front of the centre of the photodiode and the normal axis of the substrate device is parallel to the direction of photodiode observation. Consequently the measures were performed changing the goniometer angle.

If now we consider figure 5.12 we can evaluate the behaviour of the OLED emission profile changing the amount of nanoparticles in the scattering layer. Consequently, we can assert that there is no appreciable change in the angular distribution if compared to the lambertian behaviour supporting what we already mentioned in the introduction.
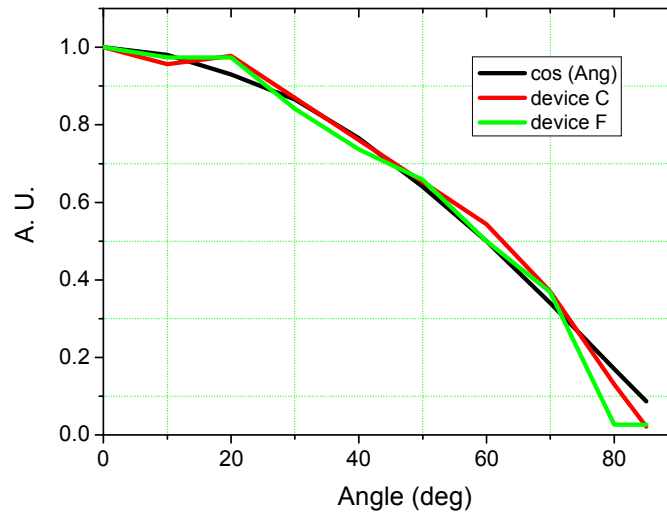
Fig. 5.12: Distribution of light intensity of OLEDs under investigation versus angle changing the ZnO nanoparticles amount in the scattering film.

In summary, several kind of polystyrene-ZnO nanocomposites have been characterized to study the optical parameters of this mixture to be used as scattering film in lighting application.

The optical parameters have been investigated and an anisotropy factor around 0.91 was found.

We have found that increasing the thickness or the percentage in weight of ZnO nanoparticles there is an improvement of device efficiency. In particular, with a thickness of around 12μm is possible to reach around a 30% of improvement in the light emission.

In conclusion, we have utilized a radiative-transport analysis to develop a simple light extraction system that can be suitable in OLED lightning applications, while it must be carefully used for displays application because the device active area seems to increase.

References

[1] S. Moller, S. R. Forrest, Journal of Applied Physics, 91, 3324 (2002)

[2] J. M. Lupton, B. J. Matterson, and I. D. W. Samuel, Applied physics Letters, 77, 3340 (2000)

[3] Y.J. Lee, S.-H. Kim, J. Huh, G.-H. Kim, Y.-H. Lee, S.-H. Cho, Y.-C. Kim, and Y. Rag Do, Applied physics Letters, 82, 3779 (2003)

[4] Weixin Li,Robert A. Jones,Steven C. Allen,Jason C. Heikenfeld,and Andrew J. Steck,l Journal of Display Thecnology, Vol 2, No 2, 143-152 (2006)

[5] J. J. Shiang, T. J. Faircloth, and Anil R. Duggal J. Appl. Phys., Vol. 95, No 5, 2889-2895 (2004)

[6] R. Bathelt, D. Buchhauser, C. Gärditz, R. Paetzold and P. Wellmann, Organic Electronics, 8, 293-299 (2007)

[7] T. Nakamura, H. Fujii, N. Juni, S. Nakanishi, M. Miyatake and N. Tsutsumi, Optical Review, Vol. 11, No. 6, 370–377 (2004)

[8] K. Neyts and A. Ullan Nieto, Journal Opt. Soc. Am. A, Vol. 23, No 5, 1201-1206 (2006)

[9] Bo-Ru Yang , Kang-Hung Liu, Shih-Nan Lee, Jen-Chieh Hsieh,,Han-Ping D. Shieh, and Chin H. Chen Japanese Journal of Applied Physics, Vol. 47, No. 2, pp. 1016–1018 (2008)

[10] Y. Izumi, S. Okamoto, K. Takozawa and K. Tanaka, Japanese Journal of Applied Physics, Vol. 41 1284-1287 (2002)

[11] J. J. Shiang and Anil R. Duggal J. Appl. Phys., 95, 2880-2888 (2004)

[12] C.C.M. Ma, Y.J. Chen, H.C. Kuan, J. Appl. Polym. Sci., 98, 2266 (2005)

[13] D.W. Chae, B.C. Kim, Polym. Adv. Technol., 16, 846. 238 (2006)

[14] M. Bass, Handbook of optics Vol. I "Fundamentals, Techniques, and Design" McGraw-Hill (1995)

[15] G. Mie, Annalen der Physik, Vol. 25,No. 3, 377-445 (1908)

[16] L.G.Henyey and J.L. Greenstein. Astrophys. J., Vol. 93, 70-83 (1941)

[17] Delta Tech.: http://www.delta-technologies.com/Products.asp?C=13

[18] C. Gumu , O. M. Ozkendir, H. Kavak, Y. Ufuktepe, Journal of Optoelectronics and Advanced Materials, Vol. 8, No. 1, pp. 299-303 (2006)

[19] X. W. Sun and H. S. Kwok, Journal Applied Physics, Vol. 86, No. 1, 408-411 (1999)

[20] J.C. Manifacier, J. Gasiot, and J.P. Fillard, Journal of Physics E, Vol. 9, 1002-1004 (1976)

[21] R. Swanepoel Journal of Physics E: Sci. Instrum., Vol.16, 1214-1222 (1983)

[22] R. Swanepoel Journal of Physics E: Sci. Instrum., Vol.17, 896-903 (1984)

[23] M. I. Mischchenko, Scattering, Absorption, And Emission Of Light By Small Particles Cambridge University press, NASA, pp. 299-318 (2002)

[24] N. K. Patel, S. Cinà, and J. H. Burroughes, IEEE Journal on Selected Topics in Quantum Electronics, Vol. 8, No. 2, 346-361 (2002)

[25] I. Schnitzer and E. Yablonovitch Applied Physics Letters, Vol. 63, No. 16 (1993)

[26] R.Windisch, P. Heremans, A. Knoloch, P. Kiesel, G. H. Döhler, B. Dutta, and G. Borghs, Applied Physics Letters, vol. 74, p. 2256 (1999)

In this thesis, we investigated several problems related to the limits of organic light emitting diodes. Our results about high field and temperature measurements demonstrated that the electrical damage can be observed in the I-V plot at voltages, greater than the optical failure voltage. We investigated the change in the electrical characteristics versus the temperature. It can be assumed that the optical failure is mainly due to the glass transition temperature of one constituent layer.

In particular, Impedance measurements versus temperature have been performed to investigate the optical and electrical failure mechanisms during the glass transition phenomena. The resultant dispersive behaviour, with its significant frequency dependence was analyzed into the framework of the UDR model. By these data, for the archetypal OLED structure ITO/TPD/Alq$_3$/Al discussed in this thesis, temperatures around 328-329 K appear as a separation point between two different working regimes. Anyway, in both the two regimes, RC data display linear temperature dependences with two different slopes. These experimental findings relate definitively the OLED electro-optical response in the temperature range between 328K and 340K to the TPD behaviour and to the occurrence of the glass transition. In more detail, we infer that the slope changes in the OLED electroluminescence and current occurring at 328-329 K can be related to glass transition effects mainly involving the interface regions between HTL and ETL, and HTL and the anode.

The AC electrical response of thin TPD films approaching the glass transition region has been investigated and an interface glass transition effects are localized at lower temperatures. The results analysis shows that the glass transition occurrence has a strong impact on the electro-optical behaviour of an OLED based on TPD Hole Transport Layer, defining different working regimes. In particular, glass transition kinetics seems to involve a temperature range of about 10 K below the nominal glass transition temperature. AC impedance spectroscopy coupled with thermal stress has confirmed to be a useful technique to study the processes governing the dynamics of glass transition and a tool to evidence the device operational limitations.

Another essential point for OLED devices is the aging mechanism and in particular the intrinsic aging that is strictly connected with the operation working-point of devices.

Indeed, we realized several experiments and simulations to improve the external efficiency of OLED devices, in a way that a better efficiency can be achieved improving the amount of light generated into the external environment.

A first approach was to analyze the geometry of the microlenses in order to have the right constraints to achieve our purpose for this particular type of structure, without making too many and expensive tests.

We have carried out three types of analysis, the first devoted to the geometry of the microlens, the second regarding the material to be used and a third related to the pattern density of microlenses on the substrate.

The first analysis was performed by varying the height of the microlenses to realize the best compromise. The evolution of the simulated data about the device efficiency in function of the ratio between the height and the base radius of the microlenses has shown that the best compromise is reached with a hemispherical shape.

The second analysis was performed for the choice of materials used in the microlenses manufacture. From these simulations the data shown that the most appropriate refractive index is the one that approaches close as possible to the substrate one.

The last analysis was realized to show the evolution of output power versus the change of microlenses density and to declare how it is important to cover the substrate surface to eliminate most of the light trapped paths To evaluate the simulation analysis we presented some experimental results about the realization of a microlenses array by gravure printing technique using a metal moulder that confirmed the simulations data.

A different approach to improve the external efficiency is the fabrication of texture structure to guide the light in transversal way using the same effect that guide the light along the substrate. To achieve this result we proposed two kind of texture, one on the substrate and another on the TCO. The analysis of the devices external efficiencies showed many differences between the proposed textured structures. If we report the photodiode current versus the device current, we realize that the best performances are achieved with the device realized on the textured substrate. In particular, we can note that the devices made on the untreated substrate report a reduction in the light emission of about 30% while the devices made on texturized TCO report a difference in the light extraction off about the 13%. These measures reveal a noticeable improvement in the

performance in both types of textured devices, so it can be a good approach to the external efficiency issues in OLED devices.

The last approach used in this thesis to improve the out-coupling performance of OLED devices was realized by a more unsophisticated structure, simply performing polymer-matrix by spin-coating or casting processes introducing scattering centers consisting of nanoparticles that locally change the refractive index

In summary, several kind of polystyrene-ZnO nanocomposites have been characterized to study the optical parameters of this mixture to be used as scattering film in lighting application. The optical parameters have been investigated and an anisotropy factor around 0.91 was found. We have found that increasing the thickness or the percentage in weight of ZnO nanoparticles there is an improvement of device efficiency. In particular, with a thickness of around 12μm is possible to reach a ~30% of improvement in the external efficiency parameter.

In conclusion, we have utilized a radiative-transport analysis to develop a simple light extraction system that can be suitable in OLED lightning applications, while it must be carefully used for displays application because the device active area seems to increase.

Publications and proceeding conferences
realized during the doctorate period

1. P. Vacca, M. Petrosino, R. Miscioscia, **G. Nenna**, C. Minarini, D. della Sala, A. Rubino, *"Poly(3,4-ethylenedioxythiophene):poly(4-styrenesulfonate) ratio: Structural, physical and hole injection properties in organic light emitting diodes"*, Thin Solid Films, ISSN: 0040-6090, Vol: 516, Issue: 12, Pages: 4232-423 (2008).

2. F. Villani, P. Vacca, **G. Nenna**, O. Valentino, G. Burrasca, T. Fasolino, C. Minarini and D. della Sala, *"Inkjet Printed Polymer Layer on Flexible Substrate for OLED Applications", J. Phys. Chem. C*, 113 (30), pp 13398–13402 (2009)

3. P. Vacca, **G. Nenna**, R. Miscioscia, D: Palumbo, C: MInarini, D. della Sala, *"Patterned organic and inorganic composites for electronic applications"*, J. Phys. Chem.C 113(14), Pages 5777-5783 (2009)

4. **G. Nenna**, M. Barra, A. Cassinese, R. Miscioscia, T. Fasolino, P. Tassini, C. Minarini, and D. della Sala J, *"Insights into thermal degradation of organic light emitting diodes induced by glass transition through impedance spectroscopy"*, Journal of Appl. Phys. 105, 123511 (2009).

5. Miscioscia, R.; Vacca, P.; **Nenna, G**.; Fasolino, T.; La Ferrara, V.; Tassini, P.; Minarini, C.; della Sala, D., **"*Electrooptical Analysis of Effects Induced by Floating Metallic Interlayers in Organic LEDs"*,** Electron Devices, IEEE Transactions on Volume 56, Issue 9, Page(s):1912 – 1918 (sept 2009)

6. **G. Nenna**, T. Fasolino, R. Miscioscia, P. Tassini, A. Imparato, P. Di Lorenzo, A. Cassinese, C. Minarini, D. Della Sala, *"Organic Light Emitting Diodes: temperature-rate dependence of electro-optical properties"*, proc. conf. EL2008, 1-11-PO, Tivoli (RM), 9-12 sept. 2008

7. Miscioscia R., Fasolino T., **Nenna G**, Tassini P., Vacca P., Minarini C., della Sala D. *"A study on the effects of thin metallic inter-layers in Organic LEDs"* , proc. conf. EL2008, 1-12-OR, Tivoli (RM), 9-12 sept. 2008

8. P. Vacca, R. Miscioscia, **G. Nenna**, D. Palumbo, T. Marcianò, C. Minarini, D. Della Sala, *"Polymeric anode for OLED applications"*, proc. conf. EL2008, 1-14-

PO, Tivoli (RM), 9-12 sept. 2008

9. F. Villani, G. Burrasca, T. Fasolino, **G. Nenna**, P. Vacca, O. Valentino, C. Minarini, D. Della Sala. "*Ink-jet printing of organic semiconductors for OLED applications*". proc. conf. EL2008, 6-06-PO, Tivoli (RM), 9-12 sept. 2008

10. G. Burrasca, T. Fasolino, R. Miscioscia, **G. Nenna**, P. Vacca, F. Villani, C. Minarini, and D. della Sala, "*INK-JET printing of PF6 for OLED applications*", AIP Conf. Proc. 1042, 324 (2008)

11. T. di Luccio, D. Carbone, S. Masala, C. Minarini, **G.Nenna**, P.Vacca, O.Valentino "*Structural and optical properties of polymer/CdS nanoparticle films*", proc. conf. EL2008, 7-07-PO, Tivoli (RM), 9-12 sept. 2008

12. R. Miscioscia, **G. Nenna**, P. Tassini, A. De Girolamo Del Mauro, P. Vacca 1, T. Di Luccio, C. Minarini, D. della Sala, M. Petrosino, A. Rubino "*A simple study of OTFTs non-idealities changing the polymeric gate dielectric*" The Proceedings of the 5th International TFT Conference, P5, march 5-6, Ecole Polytechnique (Paris), France (2009)

13. **G. Nenna**, A. De Girolamo Del Mauro, R. Miscioscia, E. Calò, F. Villani, C. Minarini, D. della Sala, "*Improved light extraction in organic LED by using polystyrene-ZnO nanocomposite scattering layer*" Proc. Conf. LOPE-C June 23-25, Frankfurt, Germany P3.1. ISBN 978-3-00-028063-4 OE-A (2009)